

Ultrasonic guided waves in composite plates:

*A study of interface bond condition and material properties
determination with broadband focused air-coupled ultrasounds*

by

Sorin Vasile Teles

A dissertation submitted to the graduate faculty
in partial fulfillment of the requirements for the degree of

DOCTOR OF PHILOSOPHY

Major: Engineering Mechanics

Program of Study Committee:
Dale E. Chimenti, Major Professor
Bruce R. Thompson
Julie Dickerson
David K. Hsu
John Basart

Iowa State University

Ames, Iowa

2004

UMI Number: 3145446

INFORMATION TO USERS

The quality of this reproduction is dependent upon the quality of the copy submitted. Broken or indistinct print, colored or poor quality illustrations and photographs, print bleed-through, substandard margins, and improper alignment can adversely affect reproduction.

In the unlikely event that the author did not send a complete manuscript and there are missing pages, these will be noted. Also, if unauthorized copyright material had to be removed, a note will indicate the deletion.

UMI[®]

UMI Microform 3145446

Copyright 2004 by ProQuest Information and Learning Company.

All rights reserved. This microform edition is protected against unauthorized copying under Title 17, United States Code.

ProQuest Information and Learning Company
300 North Zeeb Road
P.O. Box 1346
Ann Arbor, MI 48106-1346

Graduate College
Iowa State University

This is to certify that the doctoral dissertation of
Sorin Vasile Teles
has met the dissertation requirements of Iowa State University

Signature was redacted for privacy.

Major Professor

Signature was redacted for privacy.

For the Major Program

TABLE OF CONTENTS

LIST OF TABLES	vi
LIST OF FIGURES	vii
GENERAL INTRODUCTION	1
Study of the bondlines in marine composites	2
Characterization of the non-contact electrostatic transducers	3
Reconstruction of infinite plate dispersion spectra by use of focused air-coupled ultrasound	5
Dissertation organization	6
CHAPTER 1 STUDY OF BONDLINES IN MARINE COMPOSITE	8
Introduction and basic concepts	8
Model development	11
Elastic waves in a halfspace	12
Elastic waves in plates	14
Elastic waves in a plate/solid substrate system	15
Numerical evaluation of the received voltage for a pitch-catch reflection setup - Received Voltage Transducer model	17
Experimental technique	29
Measurement procedure	29
Data analysis	31
Sample preparation	34

Results and discussion	44
Conclusion	51
Acknowledgments	52

CHAPTER 2 CHARACTERIZATION OF THE NON-CONTACT

ELECTROSTATIC TRANSDUCERS	53
Introduction	53
Experiment	57
Capacitive foil transducers	60
Focusing mirror	64
Data acquisition and signal processing	67
Transducer model	68
Piston model - planar and focused transducer	69
Complex transducer point	79
Results and discussion	95
Experimental results for the directivity profile measurement	98
Conclusion	104
Acknowledgments	105

CHAPTER 3 RECONSTRUCTION OF INFINITE PLATE DISPERSION SPECTRA BY USE OF FOCUSED AIR-COUPLED UL-

TRASOUND	108
Introduction and basic concepts	108
Theory of the method	112
Received Voltage Transducer Model	113
Transmission coefficient reconstruction	120
Focused probe parameters	125
Experimental procedure	125

Results and discussion	139
Isotropic samples	139
Composite material plates	143
Moderately anisotropic samples - wood plates	144
Estimation of the viscoelastic stiffness	148
Conclusion	150
Acknowledgments	150
GENERAL CONCLUSIONS	151
Summary	151
Recommendations for future research	153
APPENDIX A REFLECTION COEFFICIENT FOR A LAYERED	
 COMPOSITE	154
APPENDIX B ADDITIONAL INFORMATION ON THE COMPUTER	
 PROGRAMS USED IN THE NUMERICAL EVALUATIONS OF	
 THE ANALYTICAL MODELS	173
BIBLIOGRAPHY	179
ACKNOWLEDGEMENTS	190

LIST OF TABLES

Table 1.1	Values of the elastic stiffness of glass-epoxy composite and balsa wood	24
Table 1.2	Values of the parameters used in the numerical evaluation of the received voltage transducer model	24
Table 3.1	Values of the elastic stiffness of some common materials	124
Table 3.2	Output of the Ljung-Box randomness test performed on the random-phase signal with <i>Dataplot</i> statistical software	136

LIST OF FIGURES

Figure 1.1	Scattering from a fluid-solid half space interface. The incident, reflected, and transmitted plane waves are contained in the plane (x_1, x_3) with the x_1 direction pointing along the interface and the x_3 axis perpendicular to the half space.	14
Figure 1.2	Scattering from a fluid loaded plate in total immersion. The x_1 axis is parallel to the interfaces and located in the mid-plane of the plate. The thickness of the plate is d and the same fluid is considered for both top and bottom interfaces.	16
Figure 1.3	Scattering from a fluid loaded plate/solid substrate system. The x_1 axis is parallel to the interfaces and located in the mid-plane of the plate. The thickness of the plate is d	16
Figure 1.4	The cylindrical coordinate system for the evaluation of the received voltage of a 10 mm radius planar transducer at 1 MHz. The absolute value of the voltage is color coded (dark blue represents the lowest value). The signal is evaluated along the acoustical axis z and in the radial direction ρ . The projection in the real space of the acoustic field produced by a point source, displaced from the real space into the complex space by the length ib shown as a contour plot, accurately models a finite, quasi-Gaussian beam.	19

Figure 1.5	The received voltage geometry. The positions of the two identical transducers, shown in a pitch-catch reflection setup, are displaced in the complex plane to ease the numerical evaluation of the voltage.	20
Figure 1.6	The predicted received voltage for a water-loaded glass-epoxy/balsa sample evaluated for 500x500 frequency-wavenumber values equally spaced in the range $f=0$ - 2 MHz and $k=0$ - 0.8 mm ⁻¹ .	26
Figure 1.7	The predicted received voltage for a water-loaded glass-epoxy/balsa sample in the space-frequency domain. The result is computed through an inverse spatial Fourier transform of the (k, f) voltage.	26
Figure 1.8	The predicted received voltage for a water-loaded glass-epoxy/balsa core sample. The separation distance between the acoustical axes of the transducers is equal to their radius a . The thickness of the facesheet is 2 mm, and the balsa is considered to be a half space from $z = d/2$ to $z \rightarrow \infty$.	27
Figure 1.9	The predicted received voltage for a water-loaded glass-epoxy/balsa core sample subject to the band limitation of the transducer	27
Figure 1.10	The predicted received voltage for a water-loaded glass-epoxy/balsa core sample measured with a pair of identical planar transducers. The signal for the case of a good bond between the facesheet and core is represented by the dotted line; the continuous line represents the KDB case.	28
Figure 1.11	The predicted (dotted curve) and measured voltage (solid curve) for a water-loaded glass-epoxy/balsa sample.	28
Figure 1.12	Experimental setup - Leaky Lamb waves C-scan.	30

Figure 1.13	LLW C-Scan process. For discrete position on the scanning grid, the value of the voltage minimum is recorded and plotted as a function of the (x, y) position. The C-scan image represents the variation of this minimum over the scanning area.	35
Figure 1.14	Typical excitation signal. The RF received signal in the presence of a KDB is shown in the bottom graph while its spectrum is shown in the top graph. The chirp excitation is generated as sinusoidal oscillations with linearly decreasing period, the presence of a zero or minimum in the RF waveform, which reveals a KDB, corresponds to an amplitude decrease of a specific frequency in the spectrum.	36
Figure 1.15	Photograph of the Government Furnished Property (GFP) balsa-core composites with artificially created KDB - Teflon insert . .	39
Figure 1.16	Photograph of the GFP balsa-core composites with artificially created KDB - mechanically separated layers	39
Figure 1.17	“True” KDB fabrication process setup for GFP balsa-core composites	41
Figure 1.18	Photograph of the GFP balsa-core composites with “true” KDB induced by static pressure	41
Figure 1.19	Conventional normal incidence C-scan performed on a bi-layered Eglass-epoxy/balsa composite for detection of a open disbond . .	42
Figure 1.20	RF signal from a normal incidence measurement on a bi-layered Eglass-epoxy/balsa composite with a “true” KDB. Red and blue dash curves corresponds to signals recorded over distinct KDB areas whereas the black solid curve is measured for an known good bond.	42

Figure 1.21	Tap testing performed on a bi-layered Eglass-epoxy/balsa composite with an impact induced open disbond	43
Figure 1.22	Tap test performed on a bi-layered Eglass-epoxy/balsa composite with a “true” KDB	43
Figure 1.23	Measured signal: good bond vs. KDB. The dotted line is the measured signal for a good bond and the continuous line represents the measured voltage over a KDB.	47
Figure 1.24	LLW C-Scan: marine composite with Teflon insert - sample 1. . .	47
Figure 1.25	LLW C-Scan: marine composite with Teflon insert - sample 2. . .	48
Figure 1.26	LLW C-Scan: marine composite with Teflon insert -sample 3. . .	48
Figure 1.27	LLW C-Scan: marine composite with foam core.	50
Figure 1.28	LLW C-Scan: marine composite with balsa core and static pressure induced KDB.	50
Figure 2.1	Experimental arrangement for transducer’s directivity function measurement.	58
Figure 2.2	Schematic section of an air-coupled capacitive foil transducer. The disks of the capacitor are the micro machined backplate (controlled roughness) and the metallic layer on the dielectric film.	61
Figure 2.3	Photo of an actual capacitive foil transducer. The active surface of the probe is approximatively 10 mm. The dotted curve identifies the area where the metalized dielectric membrane is altered.	64
Figure 2.4	SolidWorks 3D computer model of the acoustic mirror. The planar electrostatic transducer is shown in dark gray, while the planar capacitive probe is dark blue and the reflected and focused rays are red.	66

Figure 2.5	The measured spectrum of the focused probe. The pressure field is sampled at equally spaced position in the focal plane. A 2D FFT transforms the (time-space) data into (wavenumber k - frequency f) spectrum. The spectrum has its amplitude color-coded, with white representing the highest value while black corresponds to the lowest amplitude. The acute angle approximates the angular beam spread of the focused probe.	66
Figure 2.6	The grid scan for acoustic pressure measurement. The color-coded 3D plot represents a typical profile of a planar transducer. The red color corresponds to high amplitude and the dark blue to low amplitude acoustic pressure. The z -axis is the acoustical axis of the transducer.	68
Figure 2.7	Planar piston transducer model. Geometry for calculating the output voltage for two transducers in reflection setup.	70
Figure 2.8	Schematic representation of the spatial beam spread of a planar piston transducer	74
Figure 2.9	Focused piston transducer model. System of two focused transducers in confocal geometry.	76
Figure 2.10	Complex transducer point model. Geometry for calculating the output voltage in a reflection setup.	80
Figure 2.11	Comparison of the numerical evaluation of the pressure field of a 10 mm diameter planar transducer at 500kHz with the CTP (solid) and piston (dotted) model. The pressure field is evaluated on the x -axis at three different position ($z/\lambda_{air} = 0, 10$ and 20) along the z -axis that corresponds to the transducer's acoustical axis.	85

Figure 2.12	Pressure field of a 10 mm diameter focused transducer at 500kHz evaluated along acoustical axis with CTP (solid) and piston (dotted) model	85
Figure 2.13	Variation of Fresnel length b and beam waist location d with focal length F_0 for 10-mm diameter focused Gaussian transducer with a 1/e waist width W_0 at 500 kHz.	86
Figure 2.14	Variation of 1/e pressure field cross-section with focal length F_0 for 10 mm diameter focused transducer at 500kHz. The 1/e pressure profile is evaluated for focal length F_0 equals to: 26.5 mm (black), 37.4 mm (red), 64.7 mm (blue), 106.0 mm (green), 212.0 mm (magenta).	86
Figure 2.15	Pressure field of a 10 mm diameter focused transducer at 500kHz evaluated along acoustical axis z and in radial direction ρ . The solid black line represents 1/e contour plot of pressure field, d is the beam waist location and b the Fresnel length or Rayleigh range defined as the distance over which the beam radius spreads by a factor of $\sqrt{2}$	87
Figure 2.16	CTP Model. Pressure field of a 10 mm diameter planar (top) and focused (bottom) transducer at 500kHz. A Gaussian transducer is replaced with a complex point source to model its acoustic profile. The dark red color represents the highest amplitudes of the pressure and dark blue the lowest value.	96

Figure 2.17	CTP Model. Pressure field of a 10 mm diameter planar (top) and focused (bottom) transducer at 700kHz. The focal length is $F_0=26.5$ mm. The numerical evaluation of the pressure field is performed over a grid of 500x500 equally spaced points in the range -20 mm to 20mm along the x -axis and 0 to 150 mm along the z -axis.	97
Figure 2.18	The measured directivity pressure profile (2D top image, 3D bottom graph) of the planar capacitive foil transducer with a radius of $a=5$ mm at 500 kHz	99
Figure 2.19	The measured directivity pressure profile (2D top image, 3D bottom graph) of the planar capacitive foil transducer with a radius of $a=5$ mm at 500 kHz	100
Figure 2.20	Comparison of the experimental acoustic profile with numerical prediction for a planar capacitive foil transducer with a radius of $a=5$ mm at 700 kHz. The “cross-sectional” pressure profile (top graph) is sampled at a distance $z = 20$ mm from the transducer. The measured acoustic pressure (black solid curve) is compared with CTP model (red dash line) and piston model (blue dash line). The bottom graph shows the experimental (black solid curve) and predicted (red dash line) pressure profile along the acoustical axis z	102
Figure 2.21	The experimental directivity pattern of the focused capacitive foil transducer measured in the frequency range 100-400 kHz close to the focal plane.	103
Figure 2.22	The experimental directivity pattern of the focused capacitive foil transducer measured in the frequency range 500-800 kHz close to the focal plane.	103

Figure 2.23	The measured (a) and predicted (b) spectrum of the received voltage of the focused capacitive foil transducer	106
Figure 2.24	The measured (a) and predicted (b) spectrum of the received voltage of the focused capacitive foil transducer in the focal plane	107
Figure 3.1	Received voltage transducer model geometry. The same setup has been used for both experimental measurements and theoretical calculations. The system of planar capacitive foil transducer and parabolic acoustic mirror has been replaced in the numerical evaluation with the equivalent focused probe.	115
Figure 3.2	Numerical evaluation of the received voltage in air for an aluminum 6061 plate of thickness 6.68 mm (0.263 inch)	121
Figure 3.3	Numerical evaluation of the received voltage in air for a Plexiglas plate of thickness 5.5 mm (0.215 inch)	121
Figure 3.4	Numerical evaluation of the received voltage for a 20-ply uniaxial glass-epoxy composite. The scan is performed along the fiber direction.	122
Figure 3.5	Numerical evaluation of the received voltage for a 20-ply uniaxial glass-epoxy composite. The scan is performed across the fiber direction.	122
Figure 3.6	Numerical evaluation of the received voltage for a basswood plate with the thickness of 6.350 mm (0.25 inch). The wood grain is in the plane of incidence.	123
Figure 3.7	Numerical evaluation of the received voltage for a balsa wood plate with the thickness of 9.525 mm (0.375 inch). The wood grain is in the plane of incidence.	123
Figure 3.8	Experimental setup for air-coupled ultrasonic measurements . . .	126

- Figure 3.9 Random phase noise excitation: first two graphs represent the absolute value and phase of the signal spectrum (bandwidth 50 kHz–1 MHz), third is the actual time domain signal with a length of 200 μ s. 130
- Figure 3.10 Typical results for impulse response $h(t)$ measurements with the pulse-compression technique. From the top: random phase noise excitation, received signal, impulse response of the medium. . . . 132
- Figure 3.11 Statistical analysis of the random-phase signal: Autocorrelation plot. The x -axis represents the numbers of lags performed and the y -axis the values of the autocorrelation. The dotted curves is the 99% confidence interval while the dashed curve is the 95% confidence interval. 137
- Figure 3.12 Air-coupled experimental geometry. The parabolic acoustic mirrors are built with a stereolithographic process (rapid prototyping) directly from a SolidWorks CAD model. 138
- Figure 3.13 Typical impulse-response sampled at discrete locations along the plate. Each waveform is obtained as the result of the cross-correlation of the excitation with the received signal. 138
- Figure 3.14 Measured voltage spectra for a Plexiglas plate. The curves represent the simulated antisymmetric (solid) and respectively symmetric (dashed) guided wave modes for the same plate in vacuum. 142
- Figure 3.15 Measured voltage spectra for an aluminum 6061 plate. The curves represent the simulated antisymmetric (solid) and respectively symmetric (dashed) guided wave modes for the same plate in vacuum. 142

Figure 3.16	Measured voltage spectrum for a uniaxial glass-epoxy composite plate. The scan is performed along (top), and across (bottom), the fibers direction. The curves represent the simulated antisymmetric (solid) and symmetric (dashed) dispersive guided wave modes.	145
Figure 3.17	Measured voltage spectrum for layered composite plates: AR-ALL1 (top) and ARALL3 (bottom). The curves represent the simulated guided wave modes for the same plate in vacuum. . . .	146
Figure 3.18	Measured voltage spectra for basswood (top) and balsa (bottom) wood plates. The curves represent the predicted antisymmetric (solid) and respectively symmetric (dashed) guided wave modes.	147
Figure A.1	Numerical evaluation of the reflection coefficient for a water loaded glass-epoxy/balsa system. The bonding between top layer and the balsa substrate is considered ideal.	166
Figure A.2	Numerical evaluation of the reflection coefficient for a water loaded glass-epoxy/balsa system for the KDB case. All parameters are kept constant from the previous case except for the boundary conditions.	166
Figure A.3	The difference in the numerical evaluation of the reflection coefficient between the good bond and KDB cases. The top horizontal and right vertical axes show the phase-match angle in water. The largest difference is concentrated at $15^\circ \pm 3^\circ$. For a frequency of 1MHz the maximum is located at 17° which it is in good agreement with the experiment.	167

- Figure A.4 Scattering from a fluid loaded two layers plate. The x_1 axis is parallel to the interfaces and located at the boundary between plates. The thicknesses of the plates are d_A for plate A and respectively d_B for plate B. Two different fluids can be considered for both top and bottom interfaces. 169

DEDICATION

*To my wife Adriana,
without whose unconditional love and support
I would not have been able to complete this work,
to my family and in the memory of my father.*

GENERAL INTRODUCTION

Non-Destructive Evaluation (NDE) techniques are used for detecting flaws and service-induced damage, for obtaining object dimensions, and for characterizing materials. In response to the ever increasing importance of composite materials in industry, NDE methods have been employed as critical tools for characterizing and evaluating these advanced materials. Composite materials are those materials that meet the following three criteria: they contain two or more distinct constituents that can be physically or visibly distinguished; they are synthesized in such a way that the form, distribution and amounts of constituents are controlled in a predetermined way; and they have unique, useful and superior performance characteristics that can be predicted from the properties, and from the amounts and arrangements of constituents on the basis of principles of mechanics. Compared to conventional engineering materials, composites can be designed to produce exceptional strength and stiffness with minimum weight, making them attractive for traditional and advanced applications.

Although many NDE methods are available for the inspection of composite materials, no single method can produce sufficiently reliable results to satisfy the requirements of safety and quality control, owing to the complexity of the material. This thesis is focused on two important aspects of the study of the composite materials: the characterization of the interface bonding in layered composites and the evaluation of the elastic material properties in air-coupled experiments.

The characterization of the condition of the interface bonding in a layered composite is critical to understanding the behavior of the material under various stress situations.

A closed disbond, alternatively known as zero-volume disbond or “kissing-disbond”, resulting from compressive stresses at the interface, poses a problem of detection by conventional normal-incidence ultrasonic NDE methods. Such an undetected defect may be dangerous because it can produce a significant decrease in structural integrity or even lead to a catastrophic failure under certain loading conditions. The first chapter of this dissertation presents an experimental and theoretical study of the bonding condition in a bi-layered composite of woven glass-epoxy/balsa employed by the marine industry.

Accurate and effective evaluation of a material’s elastic stiffness is important in the structural integrity, aging, and distributed flaw detection in composites. The requirement for partial or complete evaluation of the elastic material properties of composites was the motivation for the second part of this thesis, leading to the improvement of an air-coupled inspection system. The characterization of the experimental system and the description of the theoretical transducer model are presented in detail in this thesis. A rapid, non-contact method of reconstructing the elastic properties of a composite plate has been designed and studied theoretically and experimentally.

Study of the bondlines in marine composites

The influence of the elastic stiffness and the boundary conditions upon the propagating guided waves in plates is well known, and it has been exploited as a valuable tool in many ultrasonic NDE applications [19]. Even though the study of the dispersion curves and attenuation of the Rayleigh-Lamb waves is well established, only few attempts have been made to exploit these characteristics in producing scans of the internal defects, discontinuities, and interfacial disbonding [21], [74], [10], [84], [72], [86]. Important results in the detection of various internal defects in multilayered composite plates were obtained [9], [56] by scanning the specimen for one or more known propagating Lamb modes. By use of frequency-modulated excitation, small near-surface defects were detected, with good sensitivity in honeycomb composite facesheets [20].

The focus of our study has been the development of an NDE tool for the reliable detection of the “kissing-disbond” in marine composites. The method takes advantage of the results previously mentioned and consists of a C-scan using a carefully chosen Rayleigh-Lamb wave mode sensitive to the condition of the interface between the two layers of the specimen. A good bond produces continuity of both the compressive and shear stresses, whereas a closed disbond transmits only partially the shear stress across the glass-epoxy/balsa interface. After experimental identification of the guided wave mode most sensitive to the changes within the interface conditions in the bandwidth of the system, a pitch-catch reflection setup is exploited to produce a C-scan of the bondline. The separation distance between the acoustical axes of the transducers is set to a value approximatively the size of the radius of the probes. In this situation the minima in the received voltage and in the plane-wave reflection coefficient are nearly identical over a wide range of frequencies [62]. For comparison between the experiment and prediction, a model calculation has been extended to simulate the received voltage for various bond conditions in the same geometrical setup as the measurement. Several artificially created “kissing-disbonds” have been investigated with this technique.

Characterization of the non-contact electrostatic transducers

The dependence of the propagating guided wave modes on the viscoelastic stiffness of a medium has been used extensively for material characterization. Although this approach is well established in the water immersion measurements, it is only in recent years, owing to advances in technology, that non-contact experiments have become a realistic possibility.

The transducers currently available for air-coupled measurements can be divided into two main categories: piezoelectric and electrostatic. Perhaps the single most often used type of ultrasonic probes in NDE applications are the piezoelectric transducers. Their robustness, wide availability, and variety in characteristics and performance make them

attractive in conventional measurements. In spite of this, the use of piezoelectric transducers in non-contact experiments is somewhat limited by their low efficiency in producing or detecting acoustic waves in air and by their narrow-band spectra. To increase the generation/detection efficiency and to improve the acoustic impedance mismatch between the piezo-ceramic and air, impedance matching layers have been employed with good results by Gudra *et al.* [40]. The air-coupled experiments have been improved significantly by the development of the electrostatic transducers by Kuhl *et al.* [55] and their subsequently application by Luukkala *et al.* [68] in the reconstruction of the transmission coefficient. Efficient broadband generation and detection of acoustic waves in air have been made possible by Schindel *et al.* [90] and by Hutchins *et al.* [50] who introduced an air-coupled micromachined capacitive film transducer.

The transducers employed in the present study are planar micromachined capacitive foil probes. For the metalized dielectric film, Mylar with an aluminum layer has been selected because of its high dielectric strength and low mass. To achieve a tight focus in air, an acoustic mirror has been designed. The pressure field of the planar transducer and focused probe has been measured experimentally and compared with the predicted value. An important development was realized by Lobkis and Chimenti [62], [65], [26], who demonstrated the equivalence of Gaussian and piston ultrasonic transducer voltages. Even though the field of a piston transducer does not have a Gaussian shape, Gaussian beams can replace the combined piston directivity functions without loss of accuracy in the calculation of the received voltage. Another critical step was taken by Deschamps [30], who introduced the complex source point as a mathematical artifice to model a Gaussian beam. When a point source is translated from the real plane into the complex plane, its field in the real plane has a nearly Gaussian shape. Zeroug *et al.* [99] applied the Deschamps artifice to model acoustic beams. This idea is significant to the development of our model, allowing the replacement of the Gaussian transmitter with a complex transducer point (CTP) and using the reciprocity theorem of Auld [8] and

Kino [53] to replace the finite Gaussian receiver with a complex point receiver.

The directivity profile of the planar capacitive foil transducers, with and without reflective focusing devices, has been measured experimentally. For comparison, a theoretical model has been used for prediction of the received voltage.

Reconstruction of infinite plate dispersion spectra by use of focused air-coupled ultrasound

Materials characterization experiments, once performed exclusively in water immersion, because of the good energy coupling and the wide availability of broadband, highly focused transducers, are now also possible in an air-coupled setting as the result of development of more efficient capacitive foil transducers. An important development was the introduction by Safaeinilli *et al.* [88], [89] of a synthetic aperture scanning technique in air as a method to suppress interference by extrinsic factors and to estimate the viscoelastic stiffness in plates. Lobkis *et al.* [62] studied theoretically and experimentally the influence of the transducer's beam and geometry on the received voltage. A method for rapid reconstruction of the transmission and reflection coefficients with a broadband, wide angular range, synthetic-aperture line scans performed in water immersion has been demonstrated by Fei and Chimenti [31] and Fei *et al.* [32], [34]. The separation of the extrinsic contributions of different geometric elements such as transducer size, location, and focal length from intrinsic material properties in the received voltage expression has been shown by Lobkis *et al.* [63], [64]. Another critical contribution was made by Rohklin and Chimenti [84], who demonstrated that specific areas of the guided wave modes of a plate have their predominant influence on different elastic stiffnesses.

We show that by exploiting the broadband large angular range of our custom probes in an air-coupled transmission experiment, many guided wave modes can be successfully reconstructed by performing only one line scan with a fixed incident angle [44], [45]. A pulse compression technique and a fast data acquisition and processing system have

been exploited in order to increase the signal-to-noise ratio and to produce an excellent discrimination between the extrinsic and intrinsic contributions in the signal. The focused probe has been manufactured from a planar capacitive foil transducer and a reflective stereolithographic parabolic mirror. The design of the acoustic mirror has made possible an angular range in air of approximately 16° for the ultrasonic beam. The focusing and the impedance mismatch between the air and the samples have been exploited to produce the required wide angular range of the phase-match angles necessary for rapid reconstruction of the guided wave modes. Several types of materials have been investigated and the results compared with the numerical prediction obtained with the received transducer model.

Dissertation organization

This dissertation consists of three main chapters, preceded by this general introduction and followed by a general conclusion and two appendices. The three topics already discussed form the three main chapters of the thesis, related by the common theme of ultrasonic guided wave propagation in elastic media and application in the NDE of composite materials.

The first chapter presents an application of the ultrasonic guided wave propagating in a bi-layered composite woven glass-epoxy/balsa plate for the experimental and theoretical study of the bonding condition that exists between the two layers. Original experiment results of detecting “kissing-disbonds” are reported and compared to the analysis.

The second chapter shows analysis and measurements of the directivity profile of planar and focused air-coupled probes. An acoustic mirror has been designed and employed, along with the planar capacitive foil transducer, for broadband wide angular range ultrasonic measurements in air. A received voltage transducer model has been used for analysis and explained in detail.

The third chapter deals with evaluation of the elastic material properties in air-coupled ultrasonic experiments. The rapid non-contact reconstructions of the guided wave dispersion spectra are shown for various types of materials. The received voltage transducer model is applied to the air-coupled transmission geometry for comparison with the experiment.

Additional results are included in the appendices. Appendix A presents the formal solution of the reflection coefficient in several experimental configurations. Numerical calculations of the reflection spectra for different bonding conditions are also included and analyzed. Appendix B provides additional information needed to use the computer programs employed to produce the theoretical calculations.

CHAPTER 1 STUDY OF BONDLINES IN MARINE COMPOSITE

Introduction and basic concepts

Technological advances often are accompanied by increased materials demands, reaching for ever-higher standards of strength, durability, and performance, together with lower cost. The complex structure of advanced materials and the higher quality requirements make the task of determining structural integrity or evaluating mechanical properties more difficult than with traditional materials. An example of such an advanced material is a composite structure commonly known as marine composite, manufactured by Baltek Corporation. This composite consists of one or more glass-epoxy woven facesheets cured on top of pressure-bonded balsa wood plate of various thicknesses. Owing partially to compressive stresses at the interface between glass-epoxy facesheet and balsa/foam core, it is difficult to detect a closed disbond ("*kissing-disbond*", KDB) by conventional normal-incidence ultrasonic NDE techniques. The shape and the location of the KDB defect, alternatively called a zero-volume disbond, makes it potentially dangerous because it can drastically reduce mechanical properties of the structure under some kinds of loading. This is especially true for a composite with an undetected KDB incorporated into a structure in which the stresses will eventually increase the size of the discontinuity, producing a possibly catastrophic failure or at least a significant decrease in structural integrity. The study presented here is motivated by the failure of conventional techniques either to detect KDB or to monitor their dynamics, even for

large, artificially induced discontinuities with a known size and location.

The method for detecting KDB in marine composites consists of incorporating carefully chosen propagating plate waves to reveal the presence of a disbond beneath the glass-epoxy layer. The sensitivity of a propagating Lamb wave to the boundary conditions is exploited to detect differences in mechanical shear coupling at the interface. A good bond will produce continuity of compressive and shear stresses, but a closed disbond will only partially transmit the shear stress across the glass-epoxy/core interface. In pitch-catch ultrasonic measurements, the difference in the received voltage between the two cases, good bond and disbond, is unequivocal and can be used to identify those areas with the KDB when a C-scan is performed in an immersion test. This method will be fully explained later in this section.

Although many other investigators have tried to exploit the Lamb wave propagation characteristics such as dispersion curves and attenuation, as Chimenti extensively listed in a recent review [19], only a few, which are cited here, have attempted to capitalize on these characteristics and produce scans of internal discontinuities or interfaces using the leaky Lamb wave reflected or transmitted spectra. Notable efforts were made by Chimenti and Martin [20] to detect with good sensitivity small near-surface defects in honeycomb composite facesheets, using frequency modulated excitation, and by Bar-Cohen *et al.* [9] and Kundu *et al.* [56], [69] to inspect multilayered composite and produce a C-scan of the different internal defects by scanning the specimen for one or more Lamb modes (also known as L-scan). Dayal and Kinra [27] showed that information about matrix cracking can be obtained from reduction of in plane stiffness using the leaky Lamb wave method. Also, it is important to note that the work of Chimenti [21], Nayfeh [74], Bar-Cohen [10], Rokhlin [84], Nagy [72], Rose [86] and others prove that the Lamb wave propagation characteristics (dispersion curves, phase and group velocities and attenuation) are influenced by material discontinuities and boundary conditions.

The method developed here takes advantage of the previously mentioned results to

produce a reliable tool for investigating KDB in marine composites. Because of the known properties of the facesheet, we can choose a specific Lamb mode that is sensitive to changes at the interface between the facesheet and the core. A propagating Lamb mode defined by its frequency f and wavenumber k can be identified within the specific bandwidth of the transducers by choosing the incident angle of the incoming plane wave according to $\theta = \sin^{-1}(k/k_f)$, with k_f being the wavenumber in the surrounding fluid. To excite a Lamb wave in the composite, a pitch-catch geometry is used with both transmitter and receiver on the same side of the sample. The separation distance between the acoustical axis of transmitter and receiver is set to be approximatively the radius of the probes. The value for this distance is drawn from [62], in which it was shown that for this distance the closest correspondence of the voltage minimum with reflection coefficient zeroes occurs over a wide range of frequencies. Of course, the transducers produce a finite beam and not an infinite plane wave, but their pressure field can be expressed as an infinite series of plane waves. The transducer's ultrasonic pressure field is considered to arise from a superposition of elementary point sources producing spherical waves and located on the face of the transducer. If either Brekhovskikh's [16] or Weyl's expansion of a spherical wave into plane waves is used and the integrations over the aperture of both transmitter and receiver are performed, then the probes' ultrasonic field can be written in terms of a spectrum of plane waves. The influence of the sample over the received voltage is given by the plane-wave reflection coefficient for each individual incident plane wave from the expansion. Because numerical evaluation of this model is complicated, a computationally more efficient method is used instead to model the received voltage for the geometrical setup used here. This model, known as the complex transducer point [99], replaces the transmitter and receiver with a point source and point receiver with their real space location displaced into the complex plane. The complex transducer point is extensively explained in chapter 2. The leaky Lamb mode, which is sensitive to the KDB, can be found either theoretically, by modeling

the reflected spectra corresponding to different interface conditions, or experimentally. The latter can be achieved by comparing the signal for a known good bond to that of a disbanded facesheet, both in the pitch-catch arrangement described above. The goal is to find the angle that produces a Lamb wave only for the disbanded glass-epoxy facesheet. After this angle is identified and selected, the geometry setup is kept constant throughout the experiment to provide high sensitivity to changes of bond conditions and to produce the C-scan of the composite.

Model development

In this section the influence of the glass-epoxy/balsa wood interface on the received voltage is studied for different interface conditions: good bond, partial bond, open disbond, and KDB. In the case of a good bond, the facesheet is considered to be fluid loaded and to have a welded contact to the balsa core. For an open disbond, the glass-epoxy plate has the upper interface water-loaded and the lower boundary traction-free. The cases for which the lower interface has a smooth contact with the balsa or partial transmission of shear stress, corresponding to a rough surface, are used to model the KDB. The bond condition between the glass-epoxy layer and balsa wood is accounted for with the help of a simple stress-jump model, according to the expression developed in Appendix A. The numerical evaluation of the received voltage transducer model, for these various bond conditions, is presented. In the numerical evaluation of the received voltage, the balsa wood is considered a half space, because of its large thickness and acoustical damping compared to the glass-epoxy facesheet. A comparison of the predicted and measured received voltages is shown later in this chapter.

Elastic waves in a halfspace

Following the method of Nayfeh [73], which is explained in more detail in Appendix A, the expression of the amplitude of the displacements and stresses for a wave propagating in an elastic medium is given by

$$(u_1, u_2, u_3) = \sum_{q=1}^6 (1, V_q, W_q) U_{1q} e^{ik_x \alpha_q x_3} \quad (1.1)$$

$$(\sigma_{33}, \sigma_{13}, \sigma_{23}) = \sum_{q=1}^6 ik_x (D_{1q}, D_{2q}, D_{3q}) U_{1q} e^{ik_x \alpha_q x_3}, \quad (1.2)$$

for a solid medium and for a fluid

$$(\bar{u}_1, \bar{u}_3, \bar{\sigma}_{33})_f = \sum_{q=1}^2 (1, (-1)^{q+1} \alpha_f, ik_x \rho_f c^2) \bar{U}_q e^{ik_x (-1)^{q+1} \alpha_f x_3}, \quad (1.3)$$

where k_x is the x_1 -component of the wavenumber, c is the phase velocity $c = \omega/k_x$ along x_1 , ω is the circular frequency, α is the unknown ratio of the wavenumber components along the x_3 - and x_1 -axis and U_{1q} is the displacement amplitude on x_1 -axis. The amplitudes V_q , W_q of the displacements and D_{iq} of the stresses with $i = 1, 2, 3$ can be found in Appendix A.

Applying these equations for the case of incidence and reflection in the fluid for a solid half space would provide the complete description of the reflected and transmitted waves, as shown in fig. 1.1. Even though the composite is a layered plate, because of the large thickness of the balsa wood compared with the thickness of the facesheet and the orientation of the wood grains perpendicular to the interface, practically, the composite behaves as layered half-space. The reflection of the acoustic waves from the bottom surface of the balsa layer can be neglected because the contribution is insignificant experimentally. We will show later in this section that the expression of the reflection coefficient for the marine composite has a form similar to that of a half-space, but with mixed contributions from terms particular to the waves propagating into the balsa half-space and glass-epoxy facesheet.

Formal solutions for the displacement and stresses appropriate for this case are those given above with the convention that the overbar will be used to designate the fluid and that the superscripts (T) and (R) will be used for transmitted and reflected waves, respectively. By choosing the incident wave amplitude \bar{U}_1^R as unity, we can identify the reflected amplitude \bar{U}_2^R with the reflection coefficient R and amplitudes in the solid medium U_{11}^T , U_{13}^T and U_{15}^T with the transmission coefficients T_1 , T_2 and T_3 , respectively. Boundary conditions require the continuity of the normal displacements and stresses ($\bar{u}_3 = u_3^T$ and $\bar{\sigma}_{33} = \sigma_{33}^T$) at $x_3 = 0$. Furthermore, for an inviscid fluid, σ_{13}^T and σ_{23}^T at the interface are equal to zero. Applying these boundary conditions to the displacements and stresses we can solve for the reflection coefficient. Upon solving that equation, we obtain the following expression [36], [54], [75], [22]

$$R = \frac{\Delta_v - Y}{\Delta_v + Y}, \quad (1.4)$$

where

$$\begin{aligned} \Delta_v &= D_{11}G_1 - D_{13}G_3 + D_{15}G_5 \\ Y &= \frac{\rho_f c^2}{\alpha_f} (W_1G_1 - W_3G_3 + W_5G_5) \\ G_1 &= D_{23}D_{35} - D_{33}D_{25} \\ G_3 &= D_{21}D_{35} - D_{31}D_{25} \\ G_5 &= D_{21}D_{33} - D_{31}D_{23}. \end{aligned} \quad (1.5)$$

The vanishing of the denominator of the reflection coefficient defines the characteristic equation for the propagation of the fluid-modified surface waves on the substrate $\Delta_v + Y = 0$. In the absence of the fluid ($\rho_f = 0$ or $Y = 0$) this reduces to $\Delta_v = 0$. This latter equation is known as the Rayleigh wave equation and defines the propagation of the surface wave along the interface of an elastic semi-infinite medium [1].

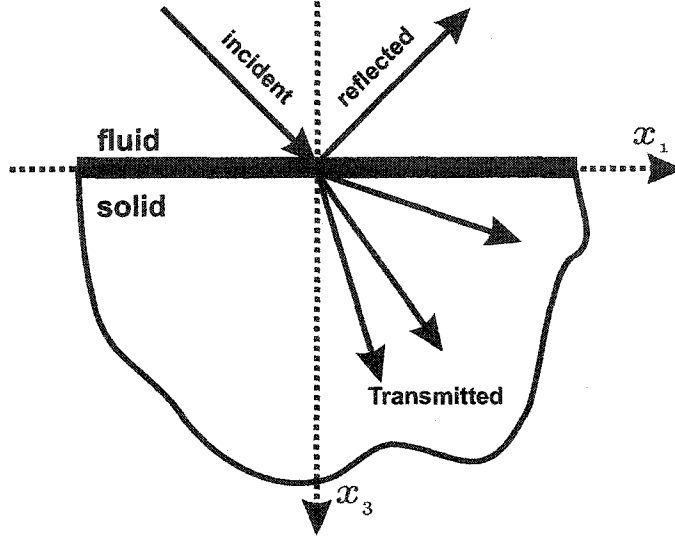


Figure 1.1 Scattering from a fluid-solid half space interface. The incident, reflected, and transmitted plane waves are contained in the plane (x_1, x_3) with the x_1 direction pointing along the interface and the x_3 axis perpendicular to the half space.

Elastic waves in plates

The formal solutions (1.1) - (1.3) are now applied for the case of a plate completely immersed in an inviscid fluid, as illustrated in fig. 1.2. Boundary conditions for this case require continuity of the normal displacement and stress for both upper and lower interface ($x_3 = \pm d/2$) between plate and fluids. In addition, for inviscid fluids the σ_{13} and σ_{23} of the solid plate will vanish. The equations obtained for this case can be solved by use of Cramer's rule for the reflected and transmitted coefficients and also for the amplitudes of the displacement U_{1q} with $q = 1..6$. By this means, the expression for the reflection coefficient for the case of a completely immersed plate in a fluid is found to be, as shown by others [10], [22], [24], [27],

$$R = \frac{AS - Y^2}{(S - iY)(A + iY)}, \quad (1.6)$$

where

$$\begin{aligned} S &= D_{11}G_1 \cot(\gamma\alpha_1) - D_{13}G_3 \cot(\gamma\alpha_3) + D_{15}G_5 \cot(\gamma\alpha_5) \\ A &= D_{11}G_1 \tan(\gamma\alpha_1) - D_{13}G_3 \tan(\gamma\alpha_3) + D_{15}G_5 \tan(\gamma\alpha_5), \end{aligned} \quad (1.7)$$

with γ given by [76]

$$\gamma = k_x d/2 = \omega d/2c.$$

A detailed derivation of the terms involved in the expression of the reflection coefficient can be found in Appendix A.

Elastic waves in a plate/solid substrate system

For the case in which the plate is fluid loaded at the top boundary and in contact with a bottom substrate, the boundary conditions allow us, as in the previous cases, to obtain the expression of the reflection coefficient. The reflection coefficient from a plate/substrate system shown in equation (1.8) is derived in a form similar to the one given in equation (1.4). The difference in the expression of the reflection coefficient comes from the fact that the contributions of both the plate and the substrate are found in every term present in its formula [2],

$$R = \frac{\Delta_{ps} - Y_{ps}}{\Delta_{ps} + Y_{ps}}. \quad (1.8)$$

The dependence of Δ_{ps} and Y_{ps} on the amplitudes of the displacements and stresses in plate and substrate is presented in Appendix A (equations A.32 and A.33). The influence of the fluid is manifested in the term Y_{ps} only. The characteristic equation for the propagation of fluid-modified surface waves in the system of layer and half-space is obtained when the denominator of equation (1.8) vanishes ($\Delta_{ps} + Y_{ps} = 0$). If the fluid is absent ($Y_{ps} = 0$, i.e., vacuum), the characteristic equation is reduced to $\Delta_{ps} = 0$, which describes the propagation of a Rayleigh-Lamb wave in the plate/substrate system.

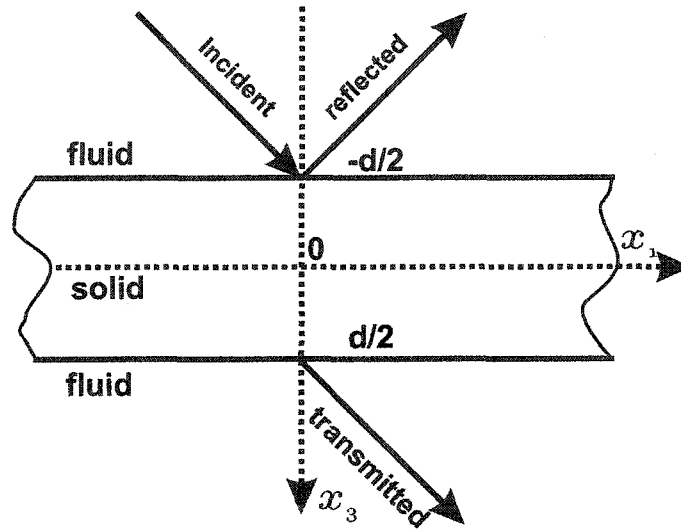


Figure 1.2 Scattering from a fluid loaded plate in total immersion. The x_1 axis is parallel to the interfaces and located in the mid-plane of the plate. The thickness of the plate is d and the same fluid is considered for both top and bottom interfaces.

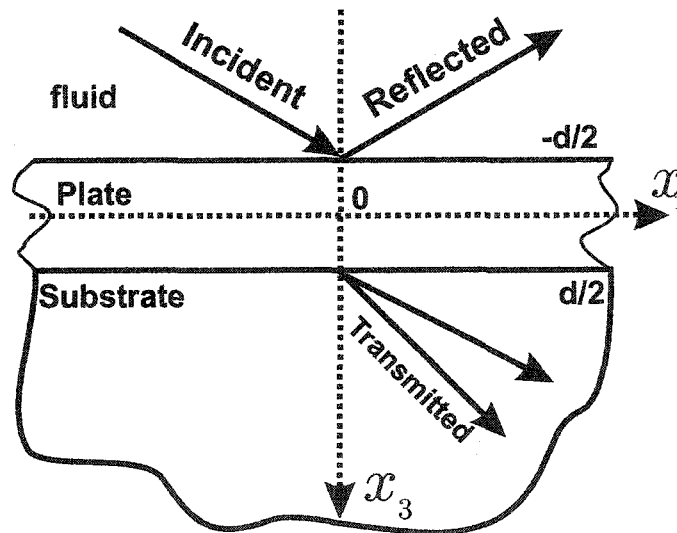


Figure 1.3 Scattering from a fluid loaded plate/solid substrate system. The x_1 axis is parallel to the interfaces and located in the mid-plane of the plate. The thickness of the plate is d .

Different interface conditions, such as welded contact or a smooth interface, are shown, in the next section, to influence the reflection coefficient and the received voltage. The difference in the received voltage is found to be more significant for specific guided wave modes. A careful selection of one of these modes will assure experimentally an unequivocal indication for the presence of a KDB.

Numerical evaluation of the received voltage for a pitch-catch reflection setup - Received Voltage Transducer model

As mentioned in the introduction, for numerical evaluation of the generated voltage, the complex transducer point (CTP) model is employed. In this section a brief description of the model's parameters is presented, and theoretical results are shown for different interface conditions. The model is exploited here without going into further details; its complete explanation can be found in the next chapter.

The CTP model replaces a pair of Gaussian beams with point sources located in the complex plane [99]. The operation of replacing the finite Gaussian transmitter with a point source simplifies the expression of the voltage sampled at any arbitrary location. The acoustic field produced by the complex source point projected in the real space accurately models a finite, quasi-Gaussian source. Furthermore, in the case of a finite Gaussian receiver, integration over the surface of the receiver is also needed to calculate the voltage. By use of the reciprocity theorem of Auld [8] and Kino [53] that implies source-detector exchange, the finite receiver can be replaced with a complex point receiver as well. When both the transmitter and receiver are complex point transducers, Zeroug et al. [99] showed that the received voltage is given directly by the spherical waves expression $V_{\text{recv}} = \mathcal{C}(e^{ik_f \mathcal{R}}/4\pi\mathcal{R})$ (equation (3.2)). The coefficient \mathcal{C} depends on the frequency, the surrounding fluid properties and the associated electronics, while \mathcal{R} is the distance between the point source and the point receiver. When the acoustic field is reflected or transmitted through various media it is convenient to use the plane-wave de-

composition of the spherical waves. Zeroug et al. [99] (equation (3.15)) and Lobkis et al. [62] (equation (6)), derived a spectral integral representation of the received frequency-domain voltage whose integrand contains the directivity functions of the transmitter and the receiver, and a spectral reflection coefficient that accounts for the acoustic wave interaction with the fluid- or air-loaded structure.

$$V_{\text{recv}}(x) = C \int R(\xi) \hat{D}(\xi) d\xi. \quad (1.9)$$

with C a parameter that was mentioned before to depend on associated electronics, frequency and fluid properties. In the latter expression, ξ can be either the phase match angle or the projection of the wavenumber on the fluid-solid interface. The term $R(\xi)$ represents the reflection coefficient that describes the acoustic wave interaction with the fluid-loaded elastic structure. The combined directivity functions, $\hat{D}(\xi)$, are Bessel functions for the piston model, Gaussian beams for Gaussian transducers, or spherical waves for CTP model. The reason for using spectral decomposition is that the reflection coefficient is conveniently calculated for plane waves. The other terms in the expression of the received voltage being easily obtained as functions of plane waves by the use of the spherical wave decomposition into a infinite sum of plane waves.

The voltage will have then a complex amplitude \mathcal{A} , which decreases along the acoustical axis with the distance from the source, and a Gaussian shape in the axial-symmetry direction. The term \mathcal{P} is the phase of the voltage, which is unity when the absolute value is calculated. The voltage, as shown later, is

$$V_{\text{recv}} \approx \mathcal{A} \mathcal{P} \exp \left\{ -k_f \left[\frac{\pm \text{sign}(z) \rho^2}{2b(1 + z^2/b^2)} \right] \right\}. \quad (1.10)$$

Here, k_f is the wavenumber in fluid, z the distance along the axis of the transducer, and ρ the off-axis distance as shown in fig. 1.4. Because of the axial symmetry of the transducer, cylindrical coordinates are used in the expression of the voltage rather than Cartesian coordinates ($x = \rho \cos \theta$, $y = \rho \sin \theta$). The parameter b , presented in fig. 1.4

as the imaginary coordinate of the complex point source, controls the Fresnel length of the transducer. The voltage of a planar 1 MHz transducer with a radius of 10 mm is evaluated with the received voltage transducer model in radial direction ρ and for distances along the acoustical axis up to 15 cm from the probe's aperture. In fig. 1.4, the dotted lines are the absolute values of the “cross-sectional” voltage evaluated at four different separation distances along the acoustical axis ($z = 0, 5, 10$, and 15 cm). With increased distance from the complex point source, the amplitude of the Gaussian profile decreases while its waist size increases.

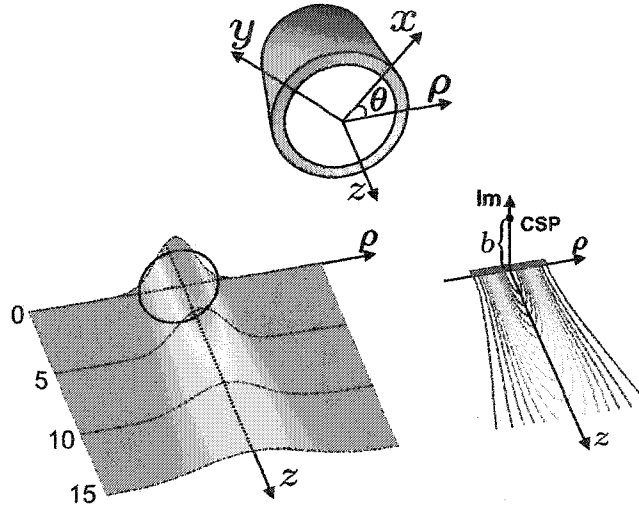


Figure 1.4 The cylindrical coordinate system for the evaluation of the received voltage of a 10 mm radius planar transducer at 1 MHz. The absolute value of the voltage is color coded (dark blue represents the lowest value). The signal is evaluated along the acoustical axis z and in the radial direction ρ . The projection in the real space of the acoustic field produced by a point source, displaced from the real space into the complex space by the length ib shown as a contour plot, accurately models a finite, quasi-Gaussian beam.

For the numerical evaluation of the received voltage we will consider the case of a pair of identical planar transducers having the same incident angle α between their

acoustical axis and the normal to the sample. The transducer pair is positioned over the sample at the same height z_0 and in the same plane (x, z) , (see fig. 1.5). For simplicity we neglect any y -dependence for both the reflection coefficient and the acoustic beam, and the problem is reduced to a two-dimensional one. Because the transducers' beams are symmetric with respect of their acoustical axis, and the measurement is performed along one of the symmetry axes of the material, in the sagittal plane, the two-dimensional problem is a good approximation for the voltage model.

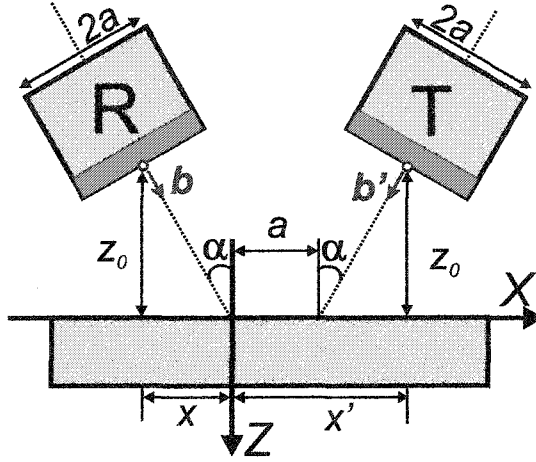


Figure 1.5 The received voltage geometry. The positions of the two identical transducers, shown in a pitch-catch reflection setup, are displaced in the complex plane to ease the numerical evaluation of the voltage.

The notation k_x is adopted for the invariant x -axis projection of the wavenumber, and then the z -axis projection is given by $k_z = \sqrt{k_f^2 - k_x^2}$. The received voltage is then obtained, according to Fei *et al.* [32], [34], and Fei and Chimenti [33], from the received voltage transducer model as

$$V(x, f) = -\frac{1}{2}\rho_f\gamma f A_T A_R \int_{-\infty}^{\infty} R(k_x, f) \frac{e^{ik_x(\tilde{x}-\tilde{x}')-i\sqrt{k_f^2-k_x^2}(\tilde{z}+\tilde{z}')}}{\sqrt{k_f^2-k_x^2}} dk_x, \quad (1.11)$$

where f is the frequency, ρ_f the fluid density, and γ a frequency-dependent factor characteristic to the associated transducer's electronics. The terms A_T and A_R are the

dimensionless strength of the transmitter and the receiver, respectively. The plane wave reflection coefficient $R(k_x, f)$ represents the sample's influence on the received voltage. The transducers have their location in the complex plane at $(\tilde{x}', 0, \tilde{z}')$ for the transmitter and $(\tilde{x}, 0, \tilde{z})$ for the receiver, respectively. The (x, y, z) coordinate system, shown in fig. 1.5, has the z -axis perpendicular to the plate with $z = 0$ on the upper surface of the plate, and the x -axis along the sample. The complex position of the transducers is then given by

$$\tilde{x}' = z_0 \tan \alpha + a - ib \sin \alpha \quad \tilde{z}' = -z_0 + ib \cos \alpha,$$

$$\tilde{x} = -z_0 \tan \alpha + ib \sin \alpha \quad \tilde{z} = -z_0 + ib \cos \alpha.$$

The parameter b defines the Fresnel length of the transducers and the direction of the axisymmetric Gaussian beam. The Fresnel length b can be expressed as $b = W_0^2 k_f / 2$, where W_0 is $1/e$ width at the waist, and k_f the wavenumber in water $k_f = 2\pi f / c_f$ ($c_f \simeq 1480$ m/s the speed of sound in distilled water at room temperature [93]). The separation between the acoustical axes measured on the sample's surface, along the x -direction, is equal to the transducers' radius a . An approximate estimation of the beam waist W_0 was found by Thompson and Lopes [94] and Lobkis *et al.* [62] to be $W_0 = 0.752a$, with a the transducer's radius.

The numerical evaluation of the received voltage is found to be performed more easily in the wavenumber-frequency domain rather than in the space-frequency domain. In the (x, f) space, the integral from equation (1.11) is not well defined for $k_x = k_f$ and high frequencies. If a spatial Fourier transformation is applied to equation (1.11), the voltage, now presented in wavenumber-frequency (k, f) space, has the expression

$$|V(k_x, f)| = \frac{1}{2} \omega \rho_f \gamma A_T A_R |R(k_x, f)| \frac{e^{k_f [b \cos(\theta - \alpha) + b' \cos(\theta - \alpha')]} }{k_f \cos \theta}. \quad (1.12)$$

The numerical evaluation of the voltage formula in the (k, f) domain is less computationally demanding. The voltage is shown to be the product of the reflection coefficient

and an exponential, which depends on the frequency, position, and orientation of the transducers. A critical normalization needs to be applied to equation (1.12) for it to be valid for arbitrary values of the Fresnel lengths b and b' . The amplitudes of both complex transducer points are normalized by the $\exp(-k_f b)$ and $\exp(-k_f b')$ respectively. The normalization makes the transducer's field at the aperture unity for all frequencies, but leaves the field profile unmodified,

$$|V(k_x, f)| = \frac{1}{2} \omega \rho_f \gamma A_T A_R |R(k_x, f)| \frac{e^{k_f \{b[\cos(\theta-\alpha)-1] + b'[\cos(\theta-\alpha')-1]\}}}{k_f \cos \theta}. \quad (1.13)$$

By use of the latter expression, the voltage is evaluated for the desired frequency bandwidth (0-2 MHz) and wavenumber range (0 - 0.5 mm⁻¹). For identical transducers with the same incident angle the Fresnel lengths b and b' are equal, and α equals α' . In fig. 1.6 is shown the result of the numerical evaluation of the received voltage in the (k, f) domain for a water-loaded glass-epoxy plate with a balsa substrate. The spectrum of the received voltage is presented as a color-coded image, with zero amplitude corresponding to the dark blue and higher amplitudes corresponding to lighter colors. The only non-zero amplitudes of the voltage are located on the line that corresponds to the acoustical axis of the transducers, as expected. It can be seen from fig. 1.6 that the slope that matches the maximum amplitude can be evaluated as $\theta = \sin^{-1}(k/k_f) = \sin^{-1}(kv_f/f) = \sin^{-1}(0.4 \cdot 1.48/2) = 17.21^\circ$, where $k = k_x$ is the non-angular wavenumber ($k = f/v$). Because the transducers are planar, their angular range is weakly frequency dependent and decreases with the increase of frequency,

$$\begin{aligned} |V(k, f)| &= \frac{1}{2} \omega \rho_f \gamma A_T A_R \frac{|R(k, f)|}{k_f \cos \theta} e^{\left\{-2k_f \left[b \sin^2\left(\frac{\theta-\alpha}{2}\right) + b' \sin^2\left(\frac{\theta-\alpha'}{2}\right)\right]\right\}} \\ &\approx \frac{1}{2} \omega \rho_f \gamma A_T A_R \frac{|R(k, f)|}{k_f \cos \theta} e^{\{-k_f [b(\theta-\alpha)^2 + b'(\theta-\alpha')^2]\}}. \end{aligned} \quad (1.14)$$

For identical transducers, the latter equation simplifies to

$$|V(k, f)| \approx \frac{1}{2} \omega \rho_f \gamma A_T A_R \frac{|R(k, f)|}{k_f \cos \theta} e^{\{-2k_f b(\theta-\alpha)^2\}}, \quad (1.15)$$

as shown by Fei *et al.* [32]. The beam width $\Delta\theta$ is determined from equation (1.15) as $\Delta\theta = 1/\sqrt{2k_f b} = 1/k_f W \approx v_f/1.504\pi a f$. In the bandwidth 0.5 MHz to 1.5 MHz, the angular range of the voltage has an average value of 2° . Therefore, the voltage will have a significant value only in the vicinity of the incident angle. This feature can be observed in fig. 1.6 to correspond to the oblique light-colored band. The dark blue curves, which are seen crossing the light colored band, are the reflection coefficient minima. These minima indicate that there exists a propagating guided plate wave for the specific frequency-wavenumber combination. Only those reflection minima that are visible in the (k, f) plot are accessible for the given bandwidth and geometry conditions.

The thickness of the glass-epoxy facesheet is 2 mm. The values for stiffness matrix $[C]$ that have been used in the numerical evaluations of the reflection coefficient and voltage for glass-epoxy facesheet and balsa wood are taken from the United States Department of defense composite materials handbook [28] and Forest Service wood handbook [37], and are presented in table (1.1). In table (1.2) are shown the model parameters employed in the evaluation of the received voltage. The interface between the facesheet and the substrate is assumed to possess the continuity only of the normal displacement u_{33} and normal stress σ_{33} in order to simulate the KDB.

The voltage is evaluated for a frequency bandwidth 0 - 2 MHz with a step of 4 kHz, and a wavenumber range 0 - 0.8 mm^{-1} with a step size of $1.6 \cdot 10^{-3} \text{ mm}^{-1}$. The incident angle for both transducers is set to the value 17° to correspond to the experimental setup. To obtain the frequency dependence of the voltage for a specific separation distance between the transducers, an inverse spatial Fourier transform is performed over the $V(k, f)$ voltage. The result of the transformation is the spatial-frequency dependent voltage, as shown in fig. 1.7. The absolute value of the spectrum of the received voltage is presented in fig. 1.7 as a color-coded image as a function of the separation distance between the acoustical axes of the transducers; red represents maxima while dark blue corresponds to zero amplitude. The voltage is sampled for all frequencies with a step size

Table 1.1 Values of the elastic stiffness of glass-epoxy composite and balsa wood

Material	Stiffness (GPa)								
	C_{11}	C_{12}	C_{13}	C_{22}	C_{23}	C_{33}	C_{44}	C_{55}	C_{66}
EGlass-epoxy $\rho=2.10 \text{ g/cm}^3$	50.64	15.62	5.14	50.64	5.14	13.21	5.52	5.52	17.52
Balsa wood $\rho=0.16 \text{ g/cm}^3$	3.596	0.187	0.313	0.186	0.276	0.566	0.002	0.183	0.126

Table 1.2 Values of the parameters used in the numerical evaluation of the received voltage transducer model

Transducer	Received voltage transducer model parameters						
	x (mm)	y (mm)	z (mm)	$radius$ (mm)	$angle$ (deg.)	$freq.$ (MHz)	$Band.$ (-6dB) (kHz)
Transmitter	430	0	-120	10	17	1	400
Receiver	-420	0	-120	10	17	1	400

of 0.1953 mm in both the positive and the negative directions. From this data set the frequency dependence for a separation distance equal to the radius of the transducers is extracted (fig. 1.8).

Fig. 1.8 shows several minima in the received voltage, which correspond to propagating Lamb waves in the facesheet. When the frequency bandwidth of the transducers is superimposed, the received voltage, presented in fig. 1.9, is shown to detect only one propagating Lamb mode. The transducers are considered to have a central frequency of 1 MHz with a bandwidth of 400 kHz at the -6 dB points.

In fig. 1.10 is shown the result of numerical evaluation of the received voltage for two interface conditions: good bond and KDB. The good bond interface allows continuity of all displacements and stresses at the interface. The minimum in the received voltage, present only in the case of a KDB, is an unequivocal indication of a propagating Lamb wave in the disbanded glass-epoxy facesheet.

When the simulated signal is compared with the measured voltage for the KDB case, good agreement between the voltage minima is obtained. Figure 1.11 shows a comparison between the theoretical model and the experiment. The experimental signal, shown as a continuous line, is measured for a known KDB. The most important parameter in imaging KDB defects is the frequency minimum position. In the two spectra, model and experiment, the positions of the minima coincide. The transducers' parameters used in the received voltage model are those of the actual transducers used in the experiments, to be described.

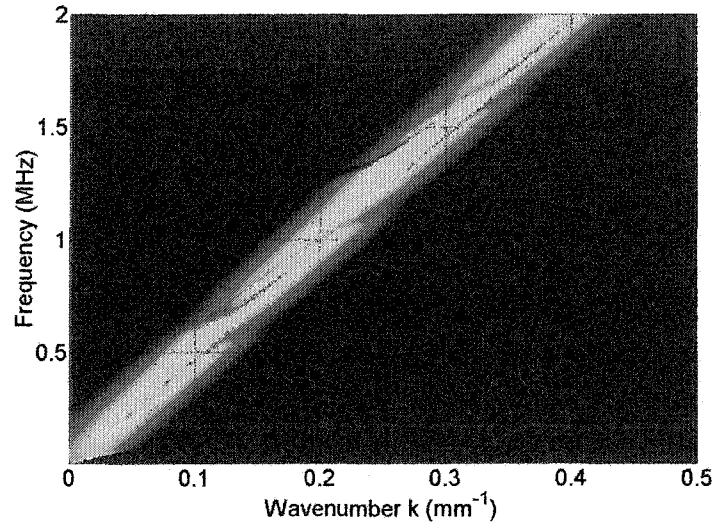


Figure 1.6 The predicted received voltage for a water-loaded glass-epoxy/balsa sample evaluated for 500x500 frequency-wavenumber values equally spaced in the range $f=0 - 2$ MHz and $k=0 - 0.8$ mm^{-1} .

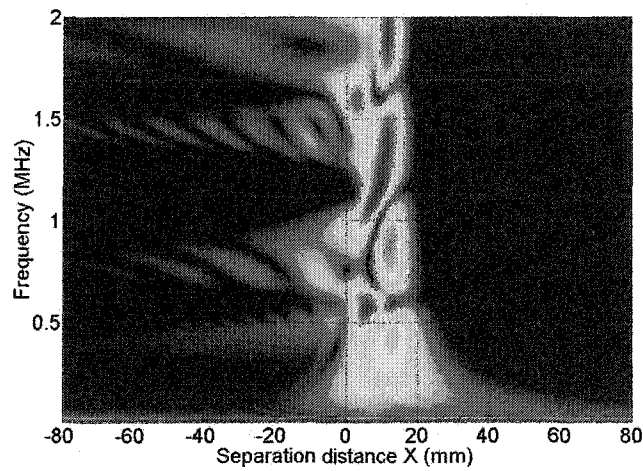


Figure 1.7 The predicted received voltage for a water-loaded glass-epoxy/balsa sample in the space-frequency domain. The result is computed through an inverse spatial Fourier transform of the (k, f) voltage.

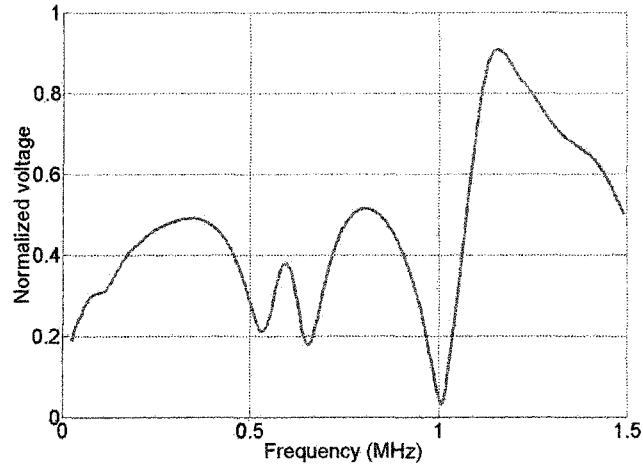


Figure 1.8 The predicted received voltage for a water-loaded glass-epoxy/balsa core sample. The separation distance between the acoustical axes of the transducers is equal to their radius a . The thickness of the facesheet is 2 mm, and the balsa is considered to be a half space from $z = d/2$ to $z \rightarrow \infty$.

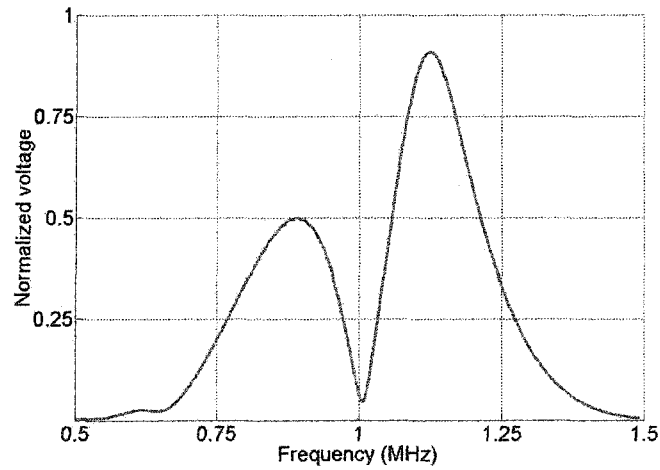


Figure 1.9 The predicted received voltage for a water-loaded glass-epoxy/balsa core sample subject to the band limitation of the transducer

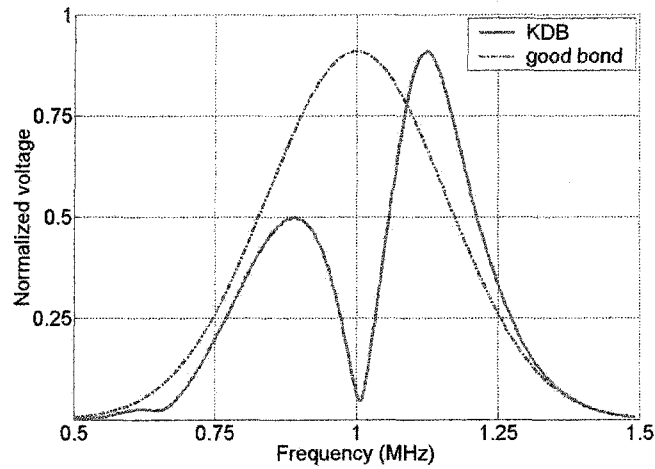


Figure 1.10 The predicted received voltage for a water-loaded glass-epoxy/balsa core sample measured with a pair of identical planar transducers. The signal for the case of a good bond between the facesheet and core is represented by the dotted line; the continuous line represents the KDB case.

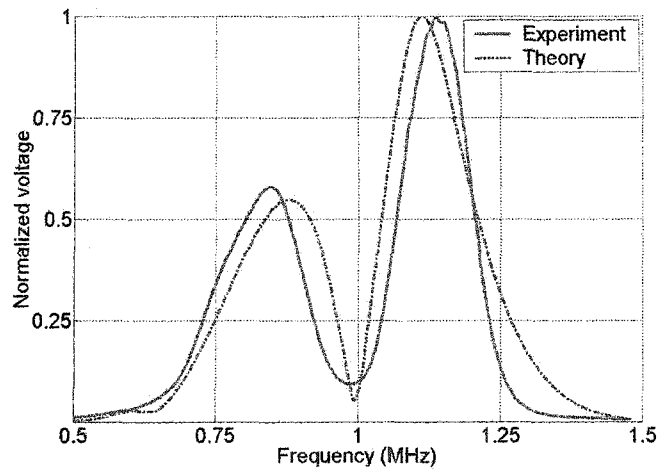


Figure 1.11 The predicted (dotted curve) and measured voltage (solid curve) for a water-loaded glass-epoxy/balsa sample.

Experimental technique

Measurement procedure

The experimental setup diagram is shown in fig. 1.12. The system is completely controlled by an IBM compatible PC running *LabView*® as the data acquisition software, thereby assuring real-time data acquisition and processing as well as easing the customization of the measurement procedure. The excitation waveform is computer generated for optimal results and uploaded into the memory of a DS345 Stanford Research Systems arbitrary function generator. For a computer generated waveform, the maximum sampling rate is 40 MHz. The maximum number of sample points that can be stored in the DS345's memory is fixed at 16,300 points. The sampling frequency can be changed to any of the values given by: $F_s = 40 \text{ MHz}/N$, with $N = 1, 2, 3 \dots 2^{34} - 1$. The vertical resolution is 12 bits, representing 0.025% of the full scale. The harmonic distortion produced by the arbitrary function generator is quoted to be less than -35 dBc.

The RF amplifier model 50A220 AR Research, which is used to increase the amplitude of the excitation to a level appropriate for inspection of a lossy medium, has a maximum power output of 75 W and a flatness of $\pm 1 \text{ dB}$ for the $f \leq 2 \text{ MHz}$ operating frequency. The harmonic distortion is less than -20 dBc for a typical 50 W output. To prevent unwanted saturation of the amplifier, the input signal is limited to a value of 1 mW (220 mV for a 50Ω impedance).

The broadband receiver model BR-640 RITEC has a bandwidth from 100 kHz to 50 MHz and a maximum gain of 64 dB when it is operating with a 50Ω load. The gain control is adjusted into steps of 4 dB in the range -12 dB to 64 dB. The output level is $2 V_{\text{peak-to-peak}}$ into a 50Ω load.

The oscilloscope model LT224 LeCroy, which has four channels and a vertical resolution of 16 bits, is used to display and acquire the raw data. Limited data processing

can be performed with the scope's math module for quick evaluation and interpretation.

The scanning system, a Parker-Daedel scan frame, has the capability to perform automatic scans along two axes; in the third axis, manual changes of the position can be made. The minimum step size is 0.01 mm for the computer-controlled axis. Two rotation stages allow accurate positioning for the transducers' incident angle, with a precision of 0.01° .

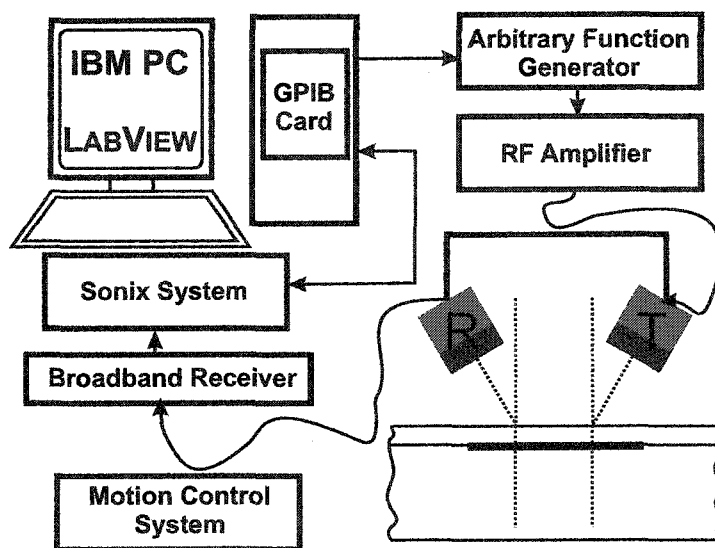


Figure 1.12 Experimental setup - Leaky Lamb waves C-scan.

Both the transmitter and receiver are 1-MHz ULTRAN broadband planar transducers WS75-1 with an active diameter of 19 mm. The loop sensitivity or the loop gain $S \text{ (dB)} = -20 \log(V_{\text{recv}}/V_{\text{ex}})$ is -36 dB, and the typical S/N ratio is about 40 dB.

Through the GPIB data bus, the PC controls the arbitrary function generator, the scanning system and the data acquisition from the oscilloscope. The excitation signal is custom designed with LabView Signal Processing Toolbox and uploaded into the arbitrary function generator memory before starting the actual measurements. The excitation signal is a frequency sweep (chirp) signal in the range 0.5-2.5 MHz (4,000

points, 10 Msamples). The signal is further amplified by the RF amplifier and applied to the transmitter. A 20-dB passive attenuator connected at the output of DS345 replaces the internal attenuator of the function generator in order to improve SNR and prevent saturation of the amplifier. The two transducers are placed in a pitch-catch arrangement over the specimen, which is immersed in the coupling fluid (water). The same experimental geometry could be used for an air-coupled arrangement.

The separation distance between the acoustical axis of the transmitter and the receiver is set to be approximatively equal to the radius of the probes. The value for this distance is drawn from [62], in which it was shown that for this distance the closest correspondence between the voltage minima on reflection coefficient zeroes and propagating Lamb waves occurs over a wide range of frequencies. Transmitter and receiver are both fixed to a frame that keeps the distance between them constant during the scanning process. In the region where a specular reflection is present, the amplitude of the received signal is high enough to produce saturation in the receiver amplifier. For this reason, the received signal from the transducer is fed to the input of a RITEC broadband receiver through another passive attenuator. The amplified RF signal and its video envelope are displayed on the oscilloscope, then digitized and sent to the computer for further data processing. A data acquisition LabView “.vi” file controls not only the customization of the excitation signal, the upload into the arbitrary function generator memory, and acquisition of the received waveform from the oscilloscope, but also the position of the probes over the sample. The program also produces the desired C-scan.

Data analysis

Because the transducers are reciprocal devices and the spectrum of the excitation signal used in this measurements is broader than the bandwidth of the probes, the effect of the transducers is similar to a window function in the frequency domain. This means the bandwidth of the measurement is limited to that of the probes. For the direct or

specular reflection, the spectrum of the received waveform should remain unchanged. When a leaky Lamb wave is present, its re-radiated field adds coherently to that of the specular reflection, and a distortion in the received waveform results because of interference. The distortion consists of a lateral shift along the interface in the direction of the propagating Lamb wave of the weight center of the reflected beam and the appearance of a so-called “null zone”, together with a trailing field that decays exponentially as it extends along the interface in the direction of the propagating Lamb wave [14].

As already cited, for a separation between acoustical axes of the transducers approximately equal to their radius, the minima in the received voltage will correspond to zeroes of the plane-wave reflection coefficient. When the conditions for efficient mode conversion from a compressional wave in the fluid to a Rayleigh-Lamb wave in the plate are met, zeroes or minima will occur in the plane-wave reflection coefficient. The excitation signal is a swept-frequency burst, or chirp with a cosine ramp up and down. The envelope of the time-domain waveform and the amplitude of the absolute value of the waveform spectrum have basically the same rectangular shape that it is windowed down with the cosine ramp. Because of the way the chirp excitation is generated as sinusoidal oscillations with linearly decreasing period, the presence of a zero or minimum in the received waveform corresponds to an amplitude decrease of a specific frequency in the spectrum. The broadband receiver amplifies and captures the video envelope of the RF signal. To facilitate data processing and decrease the processing time, the acquisition of the video envelope is used instead of the time-domain RF waveform. Because we monitor the amplitude of a carefully chosen Lamb mode that is characteristic of the glass-epoxy facesheet composite and that does not appear in the case of a good bond to the balsa core, we can enhance defect discrimination by limiting the measurement bandwidth to the region of interest. By recording either the average value or minimum in the frequency window for every position over the sample, an accurate C-scan for the KDB condition is achieved.

Two approaches can be used to identify the Lamb mode most sensitive to the interface between the glass-epoxy facesheet and the balsa/foam core. The first is based on theoretical calculations of the reflection coefficient and received voltage for the case of a good bond (i.e., continuity of stresses and displacements at the interface) and an open disbond (i.e., continuity of normal stresses and displacements only) between the facesheet and core. For a given probe bandwidth, one combination of wavenumber-frequency corresponding to a Lamb mode present only in the KDB case is chosen. From this numerical prediction, the frequency and the incident angle can be calculated from $\theta = \sin^{-1}(k/k_f) = \sin^{-1}(kv_f/2\pi f)$, where f is the frequency, k the wavenumber, θ the incident angle and v_f the wavespeed in the fluid. The position of the recording time window of the measurement system must be consistent with the frequency of the chosen guided wave mode.

The second approach, which is purely experimental, consists of identifying the incident angle θ that excites a Lamb mode in the marine composite when the composite has a KDB but not otherwise. To detect this angle, an artificially induced defect is necessary as a reference. This is a phenomenological process, but shown to provide useful results. After following through by use of either one of the approaches the position of both the transmitter and receiver, the frequency, the incident angle, and the time window location are known.

In fig. 1.13 is presented the process that transforms the measured raw data into a C-scan image of the interface. For each individual (x, y) position in the C-scan the video envelope of the received signal is recorded. As noted above, the chirp excitation that generated as sinusoidal oscillations with linearly decreasing period is received with a zero or minimum in the RF waveform when a KDB is present. This decrease in amplitude produces an amplitude decrease of a specific frequency in its spectrum, as shown in fig. 1.14. Therefore, the video envelope of the time domain signal and the amplitude of the spectrum have similar shape, thus permitting mutual substitution in our analysis.

We prefer the usage of the video envelope of the RF signal, which is provided by the broadband receiver, over the spectrum to increase data acquisition speed and processing. In fig. 1.13 five actual signals recorded from different positions on the scan grid are shown. The frequency of the selected Lamb wave mode that is specific to the KDB case is positioned close to the center frequency of the probes, as it can be seen for the signals corresponding to the positions 2,3, and 4. The received signals at positions 1 and 2 are characteristic to a good bond, because of the non-presence of minima in the signals. The rectangular box shown in fig. 1.13, for all five signals, represents the gate in which the signal was measured. The value measured by use of the gate (i.e., minimum or average value; either of them yields similar result) is recorded according to the individual (x, y) position in the C-scan. The arrows in fig. 1.13 point to the actual location on the C-scan they produced. Red color represents high amplitudes while dark blue low value signals. The presence of a circular KDB can then be easily distinguished in the center of the C-scan image.

Sample preparation

Several types of defective samples were investigated using the technique described above. The lack of interfacial bonding, characteristic of the KDB, was simulated in balsa core samples by embedding a very thin, $12.5\ \mu\text{m}$, Teflon foil at the interface between the composite facesheet and core before the sample was cured. The Teflon foil prevents bonding between the facesheet and core. This type of close contact between the foil and both facesheet and core will allow transmission of the compressional stresses, but not of shear waves. An example of such a sample is shown in fig. 1.15, with the defect visually detectable.

In the case of a foam core sample (AIREX R82 manufactured by BALTEK Corporation), shown in fig. 1.16, the KDB is produced by drilling a hole from the bottom to the facesheet/foam interface and polishing the glass-epoxy composite to obtain a smooth

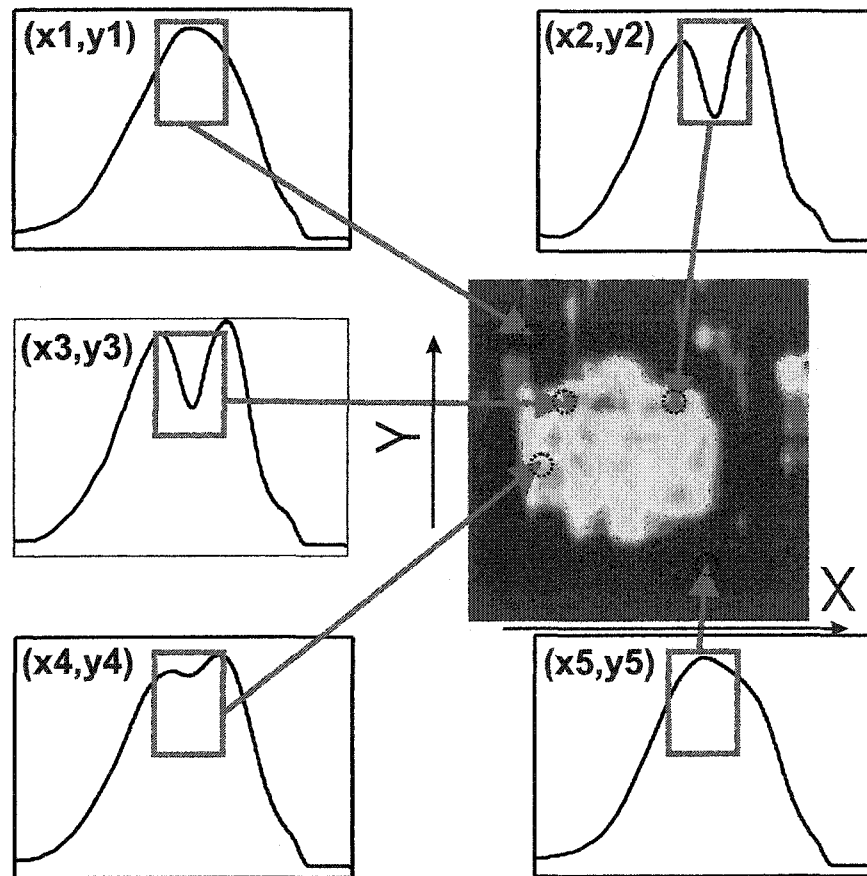


Figure 1.13 LLW C-Scan process. For discrete position on the scanning grid, the value of the voltage minimum is recorded and plotted as a function of the (x, y) position. The C-scan image represents the variation of this minimum over the scanning area.

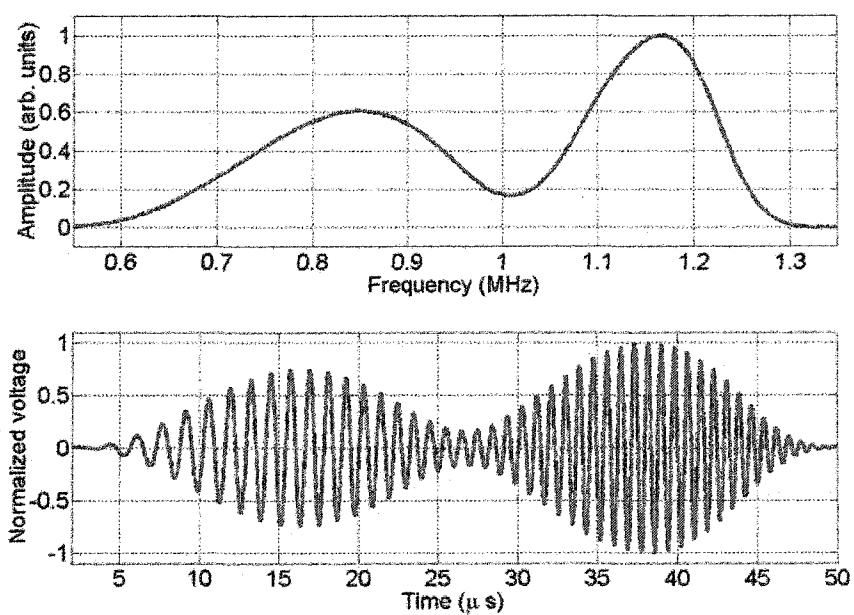


Figure 1.14 Typical excitation signal. The RF received signal in the presence of a KDB is shown in the bottom graph while its spectrum is shown in the top graph. The chirp excitation is generated as sinusoidal oscillations with linearly decreasing period, the presence of a zero or minimum in the RF waveform, which reveals a KDB, corresponds to an amplitude decrease of a specific frequency in the spectrum.

interface. Another cylindrical foam shape is then added, such that the facesheet is in contact with the added foam, but without bonding between them. The thickness of the foam core is 4 inches, four times larger than the balsa. The dimensions of the foam core specimen are 5 feet in length and 2 feet in width. Damage from shipping and handling as well as packing residues were visible on the glass-epoxy facesheet.

Even though these defects are close to real disbonds, they all fail to emulate all the characteristics of a “true” KDB because of the way they are fabricated. Therefore, a process that produces a “true” KDB has been sought. We have devised a new scheme to produce authentic KDB samples from the GFP balsa-core composites. If we load a balsa-core sample quasistatically, a “true” KDB can be produced. The method consists of applying increasing pressure, from 0 to 400 psi, with a hydraulic ram over one side of the marine composite, slowly, over a period of two to three minutes. In a relatively short period of time, the adhesive bond between the glass-epoxy facesheet and balsa core will begin to fracture on the surface opposite to the one where the stress is applied, leaving a KDB. The ram depicted in fig. 1.17 is a two-stage hydraulic hand pump manufactured by OTC (manufacturer part no. 4016). The first stage provides high oil volume, 2.6 in³ per stroke, for rapid ram approach. At 300 psi, the ram automatically switches to the high-pressure, low-volume stage, 0.16 in³ per stroke, for high-stress applications. The pressure at which disbonding begins is established; then, dwelling at that stress level for 30 seconds or so, allows the cracking to proceed to a delamination with contact (i.e., KDB). The growth of the crack is accompanied by a distinct acoustic emission signal, the level of which is used phenomenologically to decide the appropriate stress settings. The optimum level of the pressure for which the KDB develops was found experimentally to be 400 psi for the balsa core samples. The arrangement for the fabrication of the “true” KDB is shown in fig. 1.17. The region of disbonding is controlled by time under stress, rather than the stress level itself. The result is a near picture-perfect KDB that is visually detectable because of the semitransparent nature of the glass-epoxy layer.

A photograph of a sample with a discontinuity fabricated in the fashion just described is shown in fig. 1.18. The KDB area is of a lighter shade and is located in the center of the sample. The circle shows the position of the piston on the opposite side of the sample. The grid, present on the sample, is 0.5 in. For comparison, a United States quarter is placed on top of the sample (24.3 mm diameter). The shape of the KDB is irregular, but close to a circular shape. The approximate diameter of the KDB is 3 inches (76.2 mm). The result of our sample fabrication process is a “true” KDB that is virtually undetectable in any conventional normal incidence stress-wave testing, in which only low-amplitude normal forces are applied, or by tap testing [25].

Conventional ultrasonic scanning or normal incidence measurements show virtually no difference between the bonded and disbonded locations. In fig. 1.19 is presented the results of a conventional normal incidence C-scan performed on a bi-layered Eglass-epoxy/balsa composite for detection of an open disbond. The disbond is created by impact with minimal damage caused to the Eglass-epoxy but with the balsa layer crushed that produces the open disbond. The fig. 1.19 shows that an open disbond is detectable in a normal incidence measurement whereas for a KDB, virtually there is no difference between the bonded and disbonded locations in the RF signal, as shown in fig. 1.20. Both dash curves, red and blue, in fig. 1.20 correspond to the RF signal measured over a KDB area in a normal incidence measurement while the black solid curve is the RF signal for a good bonding. A direct comparison among these three signals shows no discernable difference that can be exploited for unambiguous detection of KDB.

Tap testing is widely used as a tool for a quick evaluation of any accessible surface to detect the presence of delamination or debonding. The tap testing procedure consists of lightly tapping the surface of the part with a coin, light special hammer, or any other suitable object. The acoustic response is compared with that of a known good area; a “flat” or “dead” response is indication of a flaw. The acoustic response of a good part can vary dramatically with changes in geometry, in which case a standard of some sort

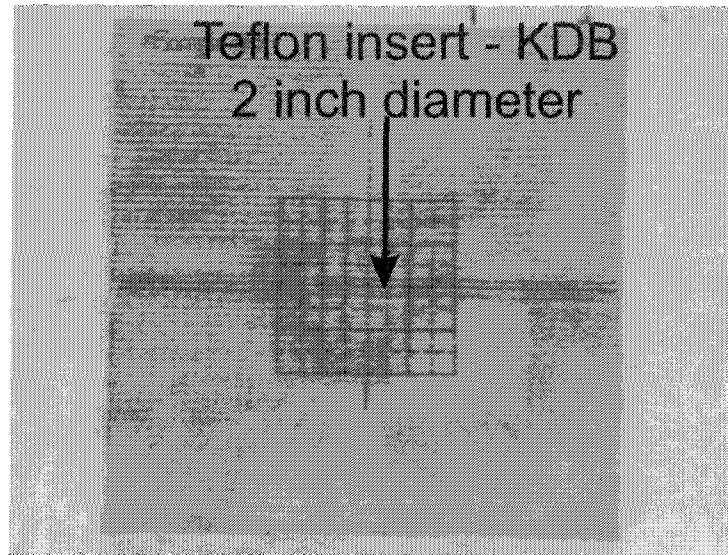


Figure 1.15 Photograph of the Government Furnished Property (GFP) balsa-core composites with artificially created KDB - Teflon insert

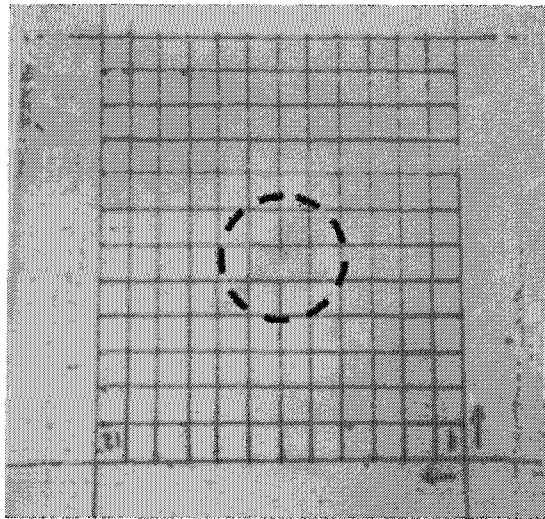


Figure 1.16 Photograph of the GFP balsa-core composites with artificially created KDB - mechanically separated layers

is required. An instrumented tap test system that uses an accelerometer with a brass tip as a tapper, has been developed at Iowa State University by a group of researchers led by Dr. David K. Hsu [49], [80], [11]. The tap test system can be used for producing images of the local stiffness that revealed the presence of defects as well as internal substructures. An example of tap testing performed on a bi-layered Eglass-epoxy/balsa composite with an impact induced open disbond is shown in fig. 1.21. The result is a color-coded map of the local stiffnesses of the composite, presented in a similar fashion as a C-scan. The red color represents a decrease in stiffness and reveals the presence of an open disbond. A totally different case is when exactly the same method is applied to detect the presence of a KDB. Fig. 1.22 shows the result of a tap test performed on a bi-layered Eglass-epoxy/balsa composite with a “true” KDB. It is clear that the result fails to reveal the presence of the defect. In conclusion, although both conventional normal incidence stress-wave testing and tap testing produce positive detection of open disbonds in bi-layered composites, both methods fail to detect KDB in exactly the same samples leaving any “true” KDB virtually undetectable.

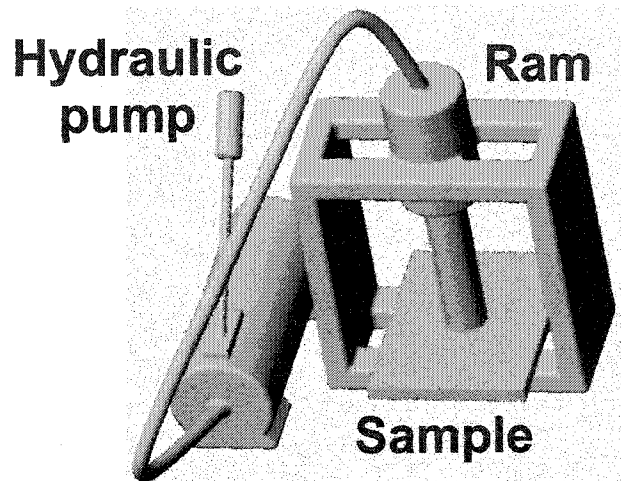


Figure 1.17 “True” KDB fabrication process setup for GFP balsa-core composites

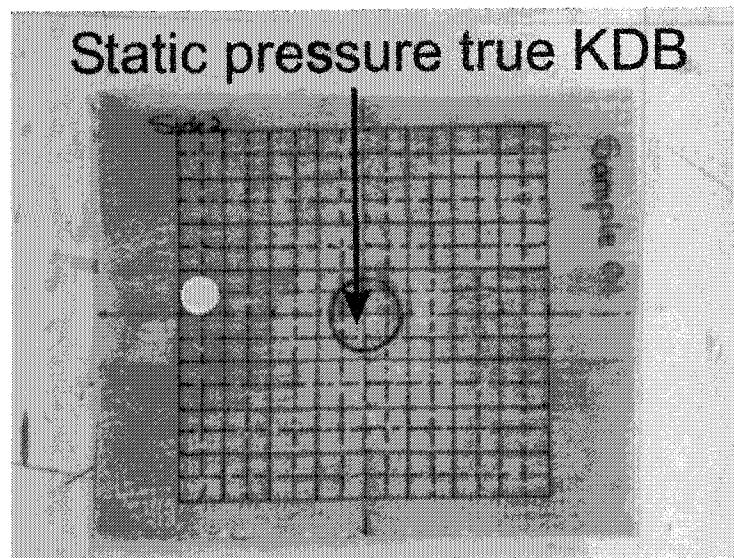


Figure 1.18 Photograph of the GFP balsa-core composites with “true” KDB induced by static pressure

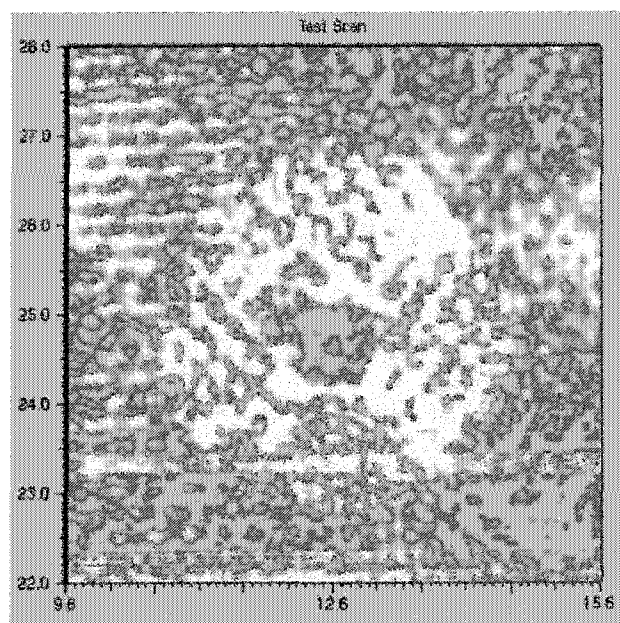


Figure 1.19 Conventional normal incidence C-scan performed on a bi-layered Eglass-epoxy/balsa composite for detection of a open disbond

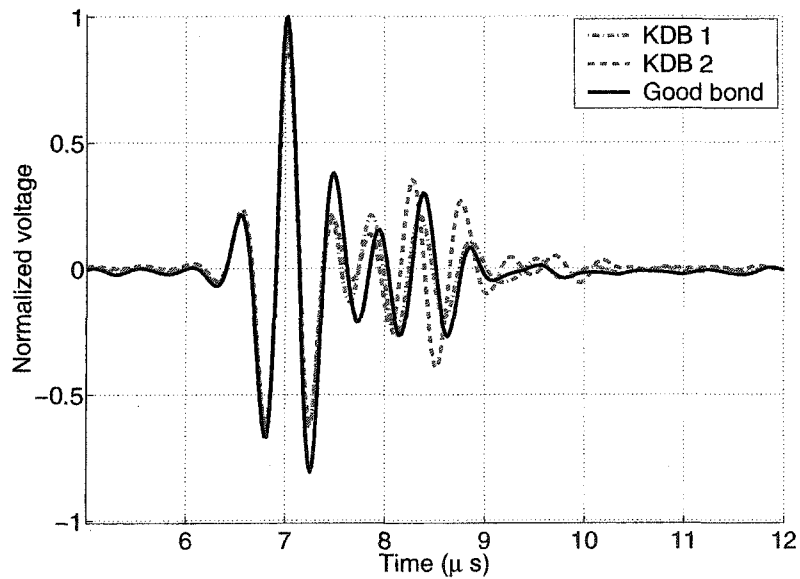


Figure 1.20 RF signal from a normal incidence measurement on a bi-layered Eglass-epoxy/balsa composite with a “true” KDB. Red and blue dash curves corresponds to signals recorded over distinct KDB areas whereas the black solid curve is measured for an known good bond.

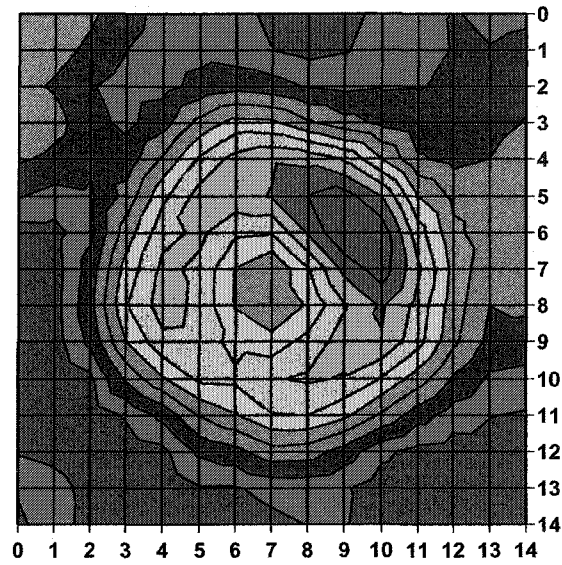


Figure 1.21 Tap testing performed on a bi-layered Eglass-epoxy/balsa composite with an impact induced open disbond

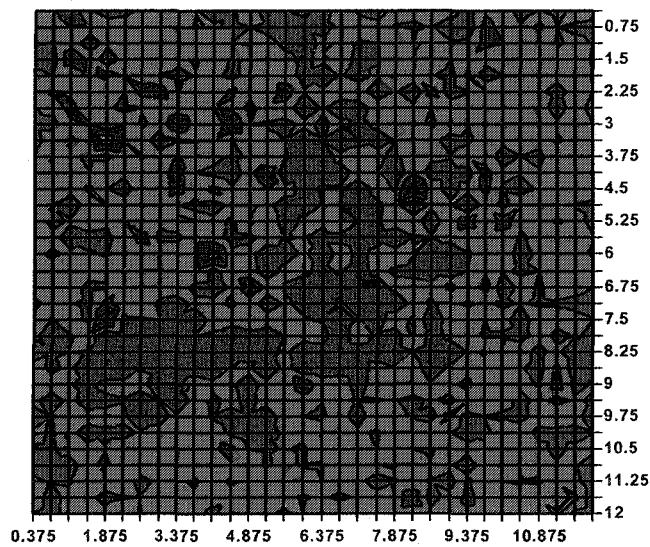


Figure 1.22 Tap test performed on a bi-layered Eglass-epoxy/balsa composite with a "true" KDB

Results and discussion

In this section is described the data processing of leaky Lamb wave C-scans; also presented and discussed are results of this method for foam-core marine composites with artificially induced KDB and balsa-core composites with two different types of KDB (Teflon inserts, and *true* “kissing disbonds”).

As mentioned in the previous section, the excitation of Rayleigh-Lamb waves is achieved by using water as a coupling medium and positioning a transducer at an angle to the sample, according to the coincidence principle. The principle states that an incident wave in a coupling medium may be used to excite a plate wave if the component of its wavenumber in the direction along the plate (x-axis) matches the wavenumber of the plate wave. By the same analysis, a transducer positioned to receive a leaking signal from the plate would be set at the same angle from the normal. By the use of an infinitely wide plane wave transducer and a single frequency signal the coincidence principle could be used ideally to excite a specific guided wave. In practice of course this is impossible because of the angular spread and frequency bandwidth of the transducers. However, by controlling the angle of the transducer and the frequency content of the signal, it is possible to direct the acoustic energy to a region of the dispersion curves where a particular Lamb (plate) wave can be excited into the facesheet composite. When the test conditions are chosen correctly, a low-damping Lamb wave will be excited in the glass-epoxy facesheet only in the case of a KDB. If there is a good mechanical shear contact between the glass-epoxy and balsa core, the carefully chosen frequency bandwidth and incident angular range will not excite a propagating Lamb wave into the glass-epoxy/balsa plate but an evanescent wave that is quickly damped. The lack of bonding at the facesheet-core interface permits the Lamb wave to propagate along the layer; in this case the wave propagation is damped by material losses and the energy leakage into the water only. Our results use this hypothesis to enhance detection of the

otherwise elusive KDB. With a disbond, most of the energy in the generated Lamb wave appears as a leaky wave in the fluid.

This method produces a very reliable difference between the spectrum of a good bond and one of a KDB (the KDB causes a minimum, revealing the propagating Lamb mode). Figure 1.23 presents both spectra for easy comparison. Away from the delamination, the reflected spectrum is dictated by the specular reflection - low in the outer portions, and high in the center of the transducer frequency range. Over the delamination, a minimum develops in the center of the spectrum. This minimum is an unequivocal indication of the presence of a propagating Lamb wave. The indication exists here because of the presence of the delamination and the lack of bond to the underlying balsa/foam core. The absence of the bond means that the facesheet can sustain a Lamb wave mode, whose subsequent energy leakage into the fluid is observed as a decrease in reflected amplitude. The correlation of the spectrum change with the delamination region was demonstrated on different samples.

At each (x, y) position on the scanning grid, a waveform is measured. To produce the C-scan pixel corresponding to that specific position, a frequency window is imposed over the waveform spectrum at a location corresponding to the frequency of the chosen propagating Lamb mode. The minimum or the average value of the amplitude inside the window is recorded and stored. The process is repeated for the rest of the desired scanning grid positions. The result of this process is presented in fig. 1.13.

Before starting the measurements to detect KDB, a measurement is necessary to determine the propagating Lamb modes of the facesheet. Several combinations of incident angle θ and frequency are recorded. In the case of a good bond, no leaky Lamb wave is observed within the bandwidth and incident angular range tested. After carefully performed tests, one Lamb mode has been identified as more sensitive than the nearby modes to the presence of KDB. The geometry required to excite this preferred Lamb mode has been maintained for tests performed on other glass/epoxy-balsa samples. In

fig. 1.24 is presented the result of the C-scan over a scanning grid of 110 mm X 120 mm, which includes the KDB area for a Teflon insert sample.

The difference between the good bond area and the KDB is clearly shown by the contrast difference. No image enhancement (contrast stretching or histogram equalization) was performed over the measured data. The detected size of KDB is about 50 mm, very close to the actual defect size (2 inches = 50.8 mm). Two more results are presented in fig. 1.25 and 1.26 to demonstrate that, with the same settings and test procedure for similar samples, the results are consistent. In all three samples, the artificially created KDB has been obtained using Teflon inserts of similar size. The dotted circle visible on the top of the each C-scan shows the actual detected size of the KDB, which is close to the one of the inserts. Because no surface finish has been performed for any of the samples, some of the extra features present on the C-scans could be results of local thickness changes owing to the woven glass-epoxy facesheet.

Even though samples 1, 2, and 3 are different and contain independently prepared KDBs, our method for detection of the simulated defect with a Teflon insert produces consistent results. For all three samples the unequivocal difference in contrast corresponding to the actual KDB area (as easily identified in fig. 1.15) shows that, with a carefully chosen experimental geometry, a facesheet-propagating Lamb mode can be excited only when the KDB is present. The existence of this mode is shown as a minimum in the reflected spectrum and mapped over the scanned area to produce the image of the glass/epoxy-balsa interface.

An entirely different case is represented by the foam-core marine composite. For the foam-core composite the difference between a good bond and a KDB or even an open disbond is small, because the acoustic impedances of air and foam are close ($Z_{air}=0.0004$ MRayl, $Z_{AIREXR82}=0.0264$ MRayl). This similarity is expected to produce a far smaller contrast difference between a KDB and a good bond. A result of inspecting a foam core marine composite is presented in fig. 1.27. Keeping the same geometry as in the

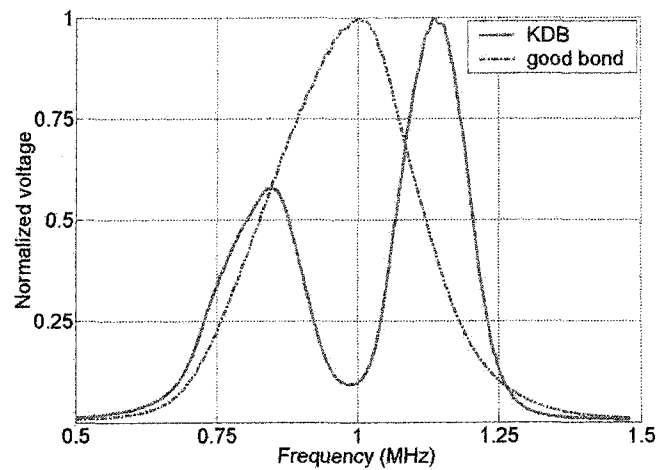


Figure 1.23 Measured signal: good bond vs. KDB. The dotted line is the measured signal for a good bond and the continuous line represents the measured voltage over a KDB.

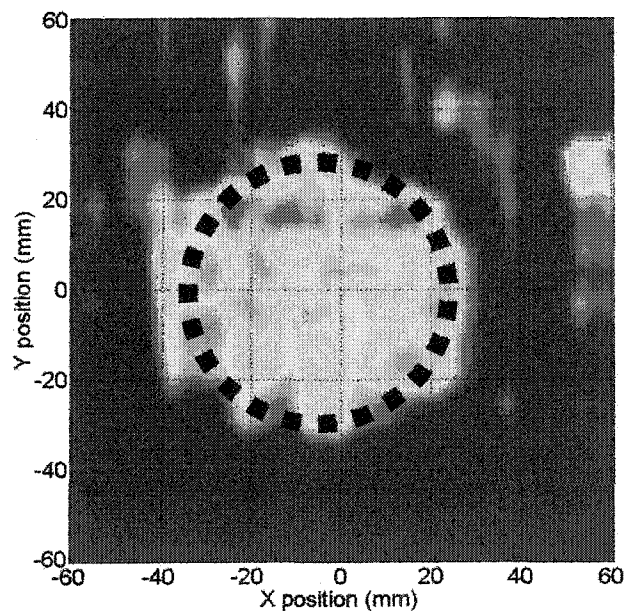


Figure 1.24 LLW C-Scan: marine composite with Teflon insert - sample 1.

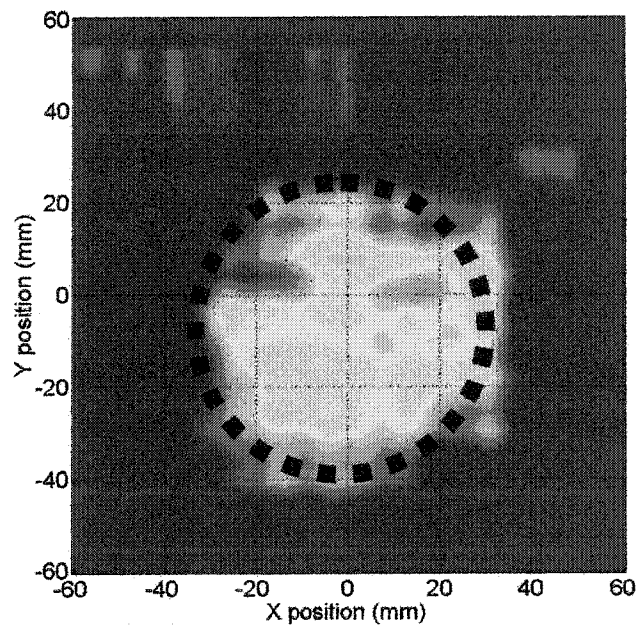


Figure 1.25 LLW C-Scan: marine composite with Teflon insert - sample 2.

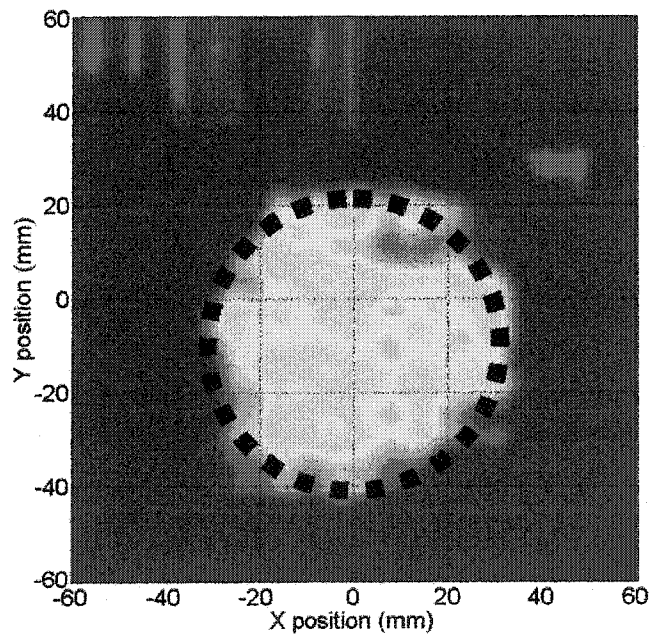


Figure 1.26 LLW C-Scan: marine composite with Teflon insert -sample 3.

previous experiments, the measurements seem to show the presence of the KDB, but this conclusion is definitely equivocal because the scan also detects other hidden features not intentionally simulated.

One explanation of these extra features might be found in the sample handling. Damage of the foam core or facesheet could easily have occurred during the fabrication process or during shipping from the Naval Surface Warfare Center Carderock Division (NSWCCD) to our lab. Another possible explanation can be found in the different failure mechanisms that operate in the glass/epoxy-balsa and glass/epoxy-foam composites. In the balsa-core material, the failures are almost exclusively at the wood-composite interface, essentially all adhesive failures. By contrast, in the foam-core composites, most failures occur in the vicinity of the interface but separated from it by a few millimeters at least. We reason that the penetration of the epoxy into the open-cell foam stiffens and strengthens the foam in the interfacial region, causing the weak zone to occur somewhat deeper into the foam and away from the interface with the glass/epoxy. The effect of these different failure mechanics is that the failed glass/epoxy facesheet has a substantial remnant of foam core attached to it. This remnant foam at the failure site, as observed experimentally, can still attenuate the leaky wave quite effectively. Another way to view the situation is that the method discussed here has strong applicability only in the case of glass/epoxy-balsa composites and much less utility for the foam-core materials.

So far, the results shown have been observed in samples with simulated KDBs. These defects are close to those of a real KDB but, because they are fabricated, none have all the characteristics of a real disbond. In the previous section we presented the process by which “true” KDB samples are produced from the GFP balsa-core composites. Because we do not simulate the KDB, but rather create the conditions for the disbond to occur naturally, our scheme produces “true” KDB. Following the same inspection procedure as presented before for the Teflon insert samples, the resulting C-scan of the “true” KDB sample is shown in fig. 1.28.

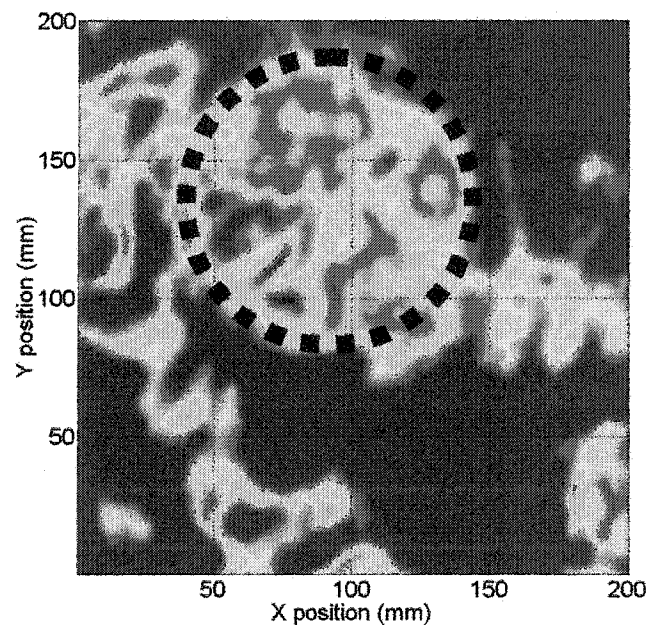


Figure 1.27 LLW C-Scan: marine composite with foam core.

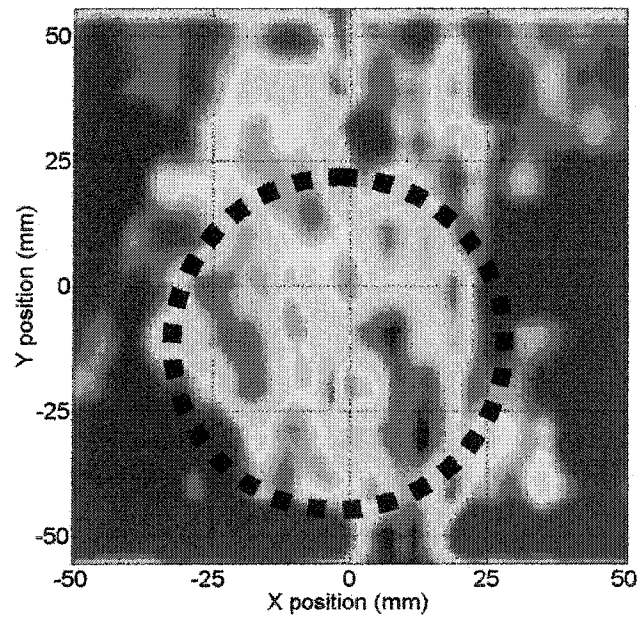


Figure 1.28 LLW C-Scan: marine composite with balsa core and static pressure induced KDB.

The high contrast between the good bond area (red) and the KDB (blue) demonstrates that the detection of a real KDB with selective Lamb modes monitoring is feasible. An additional feature, which is not related to the interface condition but which influences the overall amplitude of the reflected signal when scanned, was later identified to be a surface artifact. This artifact is clearly seen in fig. 1.28 as a vertical strip of lower contrast that crosses through the center of the scan. If this spurious feature is ignored, the result shows good detection of an otherwise invisible real KDB.

Conclusion

For many advanced bonded materials, KDBs, virtually undetectable by traditional inspection techniques, constitute a real challenge. The requirement for safety always exceeds the need for performance. The nature of these discontinuities and their location constitutes a serious obstacle to their detection. In this work we focus our study on the detection of these defect in bi-layered composites suchlike the Eglass-epoxy/end grain balsa and Eglass-epoxy/Airex R82 structural foam currently employed by United States Navy for hulls and decks in high speed offshore power boats and for the large double truncated pyramid mast for housing sensitive radar equipment.

In this chapter is shown a way to exploit the unique capabilities of guided acoustic waves to our advantage. We present an approach that leads to positive identification of KDB in a complex marine composite.

This methodology exploits the fact that a propagating Lamb wave in the glass-epoxy facesheet composite will exist only when a KDB is present at the location of the incident beam. The leaky wave into the upper fluid is then detected and monitored over the scanning grid, producing a C-scan of the interface with clear discrimination between well bonded areas and KDBs. A theoretical evaluation of the received voltage is developed, using the complex transducer point model. Numerical evaluations of the

voltage corresponding to different interface conditions are compared with the experimental measurements. The theoretical predictions are shown to be in good agreement with the experiment for a variety of samples and disbonds. The inspection technique was tested for different samples with artificially induced KDBs. A process that produces “true” KDB was developed and tested. We found that all of the KDBs were positively detected and identified, indicating the reliability of our method.

Acknowledgments

This research was supported by NSWC Contract award N00167-00-M-0694 and the Center for Nondestructive Evaluation at Iowa State University. The author thanks Dr. Dong Fei for helpful discussions on experiments and signal processing, and Dr. David K. Hsu and John Peters for lending some of the experimental apparatus.

CHAPTER 2 CHARACTERIZATION OF THE NON-CONTACT ELECTROSTATIC TRANSDUCERS

Introduction

Most NDE ultrasonic experiments require that acoustic waves travel through a fluid medium that couples the radiating energy of the transducer to the tested sample and/or vice versa. Water or other liquids are used for immersion tests, coupling liquids or gels for wet contact coupling, and air/gas for non-contact tests. Therefore, it is important to be able to characterize the behavior of the pressure field of ultrasonic probes in fluid media. The focus of this chapter is the study of the field pattern of an electrostatic air-coupled transducer. Experimental results are presented for both planar and focused transducers and compared with theoretical predictions. The transducer's pressure field is obtained using the complex transducer point model and compared with the conventional piston model.

The characterization of ultrasonic transducer fields is not new; it has been employed for many transducer types and applications. Recent advances in the design and implementation of air-coupled transducers, especially with focusing devices or natively focused probes, make feasible the non-contact evaluation of materials properties. The detailed study of such an ultrasonic tool can play a significant role in the development of air-coupled NDE techniques for quantitative materials characterization.

In the most common model of a planar transducer, as the model developed by Schmerr [92], the probe particle velocity is assumed to be constant over the transducer's

surface. With this model, known as the piston transducer model, the pressure field can be easily calculated at any arbitrary location in a fluid. For more complicated geometries, where a source, receiver, and eventually a sample are present, this piston transducer model still provides good results, although it requires for the numerical evaluation of the received voltage higher computational power. Numerical evaluation of the pressure field of focused probes is an even harder task. To derive a solution for mono-frequency focused beams using the Rayleigh integral approximation, Williams [98] and O'Neil [78] assumed the curvature of the source to be weak and the frequency high enough so that no significant diffraction phenomenon is present. Lucas *et al.* [67] used the Fresnel approximation of both the field integral and the boundary conditions to investigate the radiation of a mono-frequency focused source. Levin *et al.* [60] projected the field onto a plane at $z = 0$ perpendicular to the acoustical axis and redefined the velocity profile for this plane in order to apply the Rayleigh integral. The transducer's focal length is assumed to be sufficiently large compared with the wavelength to allow one to ignore the diffraction from the finite size of the probe. Hamilton [41] compared these three approaches and showed good numerical results for small aperture angles in the focal region and beyond for all three, although differences exist in the near field. Another approach was taken by Zeroug *et al.* [99], who developed the complex transducer point (CTP) model. In 1971 Deschamps [30] introduced the complex source point as a mathematical artifice to model a Gaussian beam. When a point source is translated from the real plane into the complex plane its field in the real plane is very nearly Gaussian. Lobkis *et al.* [62] demonstrated that even though the field of a transducer does not have a Gaussian shape, in the calculation of the received voltage that depends on both receiver's and source's field pattern, the Gaussian beams can replace the combined piston directivity functions without loss of accuracy. Therefore, the CTP is a good approximation for a piston beam in a two-transducer voltage model. Zhang and Chimenti [101] investigated the difference of beam reflection from anisotropic plates between a 2D and 3D CTP

model, Zhang *et al.* [102] studied the influence of the experimental geometry on the received voltage and on the CTP model parameters and applied this model in materials characterization [103]. Fei *et al.* [31], [32] modeled with CTP and multiple CTP the pressure field of both planar and focused transducers to obtain accurate predictions of the transducer voltage in both water-coupled reflection and transmission experiments, and they exploited the model to infer elastic stiffness from a subset of the measured data.

The task of characterizing experimentally the pressure field of the air-coupled transducers is important because of the large variation in types of capacitive probes. For most NDE applications, piezoelectric probes are used. In the case of air-coupled measurements, the use of piezoelectric probes dramatically lowers efficiency owing to the large acoustic impedance mismatch between the piezo ceramic and air, and the efficiency can be improved only marginally with impedance matching layers. An electrostatic transducer is a much better choice, providing a large sound amplitude with a relatively wide ultrasonic bandwidth. The drawback to these probes is that they are quite susceptible to damage and to electrical breakdown. A characterization of several types of air-coupled transducers was reported by Gachagan *et al.* [38] and by Pizarro *et al.* [81] for electrostatic grooved backplate transducers. The measurement and numerical modeling of the diffraction field of a piezoelectric ceramic with matching layers was presented by Gudra *et al.* [40]. Because the behavior and performance of the air coupled electrostatic probes rely heavily on the backplate mechanical finish, the goal of reducing the variability of air-coupled probe efficiency reduces to controlling the roughness of the backplate. The rest of the parameters are more easily controlled through the bias voltage or metalized dielectric film [90]. Bashford *et al.* [12] investigated quite extensively the pressure field of a micro machined capacitive foil transducer in various configurations, including beam focusing with a Fresnel plate [91]; comparison of the results with values predicted by theoretical calculation based on a planar piston model showed good agreement. Other

investigators have used laser tomography [13], [4], [70] to measure the beam profile for air-coupled transducers or have used equivalent circuits to predict their directivity patterns and resonance frequencies.

In this chapter, experimental measurements of the directivity pattern for planar capacitive foil transducers with and without reflective focusing devices are reported. The high amplitude generation in air and large bandwidth of such probes make them desirable for most non-contact NDE inspection techniques, especially for material evaluation. This type of transducer can be described from the electrical standpoint as a capacitor, with one of its electrodes very light and mobile (a metallic layer deposited on the dielectric film) and the other a fixed backplate with induced roughness. A bias voltage applied on the capacitor keeps the dielectric film in contact with the backplate by electrostatic force. When a transient voltage is applied over the capacitor, the dielectric film with its metal layer vibrates because of variations in the amplitude of the electrostatic force. These vibrations are transmitted into the air as sound waves. When a sound wave propagating in air arrives on the transducer surface, it produces mechanical vibrations of the foil and time-varying charge on the capacitor. The time-varying charge is then further amplified by a charge amplifier and converted into a transient voltage. From a mechanical standpoint, the probe acts as a vibrating membrane in which sensitivity is controlled by the mass per unit area. Many factors influence the transduction mechanism in the membrane [18], such as: membrane response to the characteristic wavelengths of the backplate periodicities (induced roughness), drum-like vibration over the backplate pits, and quarter wavelength resonances of trapped air in the plate's roughness. A focused acoustic beam is obtained by allowing the planar probe's field to be totally reflected by a parabolic mirror. Experimental measurements are compared with the numerical analysis of the analytical CTP and piston models. The measured directivity patterns are in good agreement with the theoretical field calculations.

Experiment

If a circular transducer with its active surface in the plane (x, y) is considered, then its acoustical axis is pointing along the z -direction away from the transducer's surface for $z > 0$. Because of the transducer symmetry in the plane (x, y) , polar coordinates can be used ($x = \rho \cos \theta$, $y = \rho \sin \theta$) with ρ the radial or "cross-sectional" direction and θ the polar angle. The experimental measurement of a transducer's acoustic profile can be performed ideally by sampling its ultrasonic field in the half-space $z > 0$ with a point receiver. For convenience, the sampling is performed with the point receiver scanning in a plane (x_R, y_R) , parallel with (x, y) and perpendicular to the acoustical axis, at discrete separation distances between the transducer and the point receiver. This action will produce a spatial representation of the "cross-sectional" pressure. Because of the cylindrical symmetry of a circular transducer, a line scan would be sufficient to measure the off-axis pressure. In the case of a quasi-line focused beam, the line scan will be performed along a direction perpendicular to the focal line owing to the symmetry of the beam. The point receiver in the air-coupled directivity measurement is constructed from a capacitive foil probe with its aperture masked by a high attenuation material (open cell foam) with a central pinhole. The diameter of the pinhole is 0.1 mm, which is less than half of the smallest measured wavelength. The wavelength of an ultrasound wave in air at 1 MHz is 0.343 mm. The experimental setup is presented in fig. 2.1.

The y -axis was chosen along the quasi-line focus and z -axis to correspond to the acoustical axis of the beam. To obtain the "cross-sectional" pressure field, the measurements are performed along x -axis in a line scan. In the case of a planar transducer, the x - and y -axis are both pointing in the radial direction of the beam.

Measurement of the directivity patterns of planar and of focused transducers is similar in theory but performed with different experimental setups in the two cases. The apparatus involved in the case of planar probe, and presented in the following para-

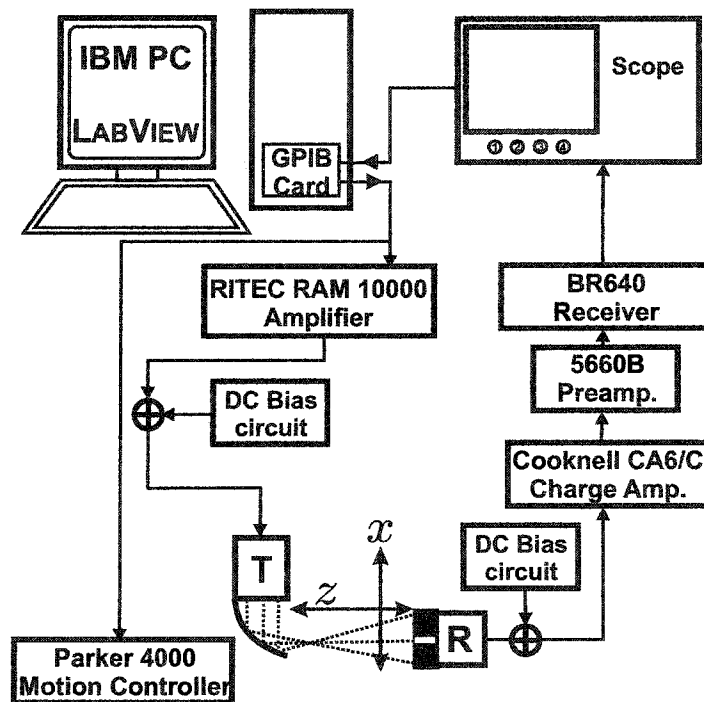


Figure 2.1 Experimental arrangement for transducer's directivity function measurement.

graph, was found to produce satisfying results initially. Later, for evaluation of material properties with focused probes, an improved setup was designed: a faster data acquisition system in conjunction with a novel digital signal processing procedure, and the capability of custom excitation waveforms. This approach helped to boost significantly the signal-to-noise ratio (S/N), filtering out interferences and speeding up data acquisition and processing. Although results from the directivity pattern of focused probes are presented here, the second arrangement will be described in detail in the next chapter in connection with extensive use in material evaluation.

The experimental arrangement has three main components: an automated scan system, an excitation/reception apparatus, and a data acquisition and processing component. The Parker Daedel MC4000 scan system has a spatial resolution of 0.01 mm for the two axes, which are computer controlled. The transducers' orientation can be independently changed with two rotation stages with a precision of 0.01° . The excitation/reception apparatus is computer controlled through a GPIB interface. Both the measurement parameters and the data acquisition and processing flow are managed with a LabView software interface on an IBM compatible PC. The excitation is a rectangular window tone burst produced by a RITEC RAM 10000 system. The central frequency of the burst is changed in discrete steps to cover the entire useful bandwidth of the probes. Because we use in our analysis only the central frequency of the burst any contribution from the side lobes is neglected. This transient voltage is applied over a bias circuit to the terminals of the transmitter. The bias is required by the capacitive foil transducer to function; therefore, the transmitter and the receiver each has its own bias circuit. The received signal is amplified with a Panametrics 5660B low noise preamplifier in the first stage. Second, a RITEC BR640 broadband receiver is used to further amplify the signal to a level adequate for the oscilloscope input. The oscilloscope LeCroy 9304A acquires and digitizes the raw data. A limited data processing is performed with the oscilloscope math module for quick evaluation and interpretation. For each z position, the data is

saved as a separate file on the computer's hard drive for further analysis.

The maximum power output of the signal generator is 5 kW rms into a 50 Ω load. The harmonic distortion at the 5 kW rms level ($\sim 1000 V_{\text{peak-to-peak}}$) is less than -40 dB for the second harmonic but about -20 dB for the third harmonic relative to the fundamental. The capacitive transducers have a nominal capacitance of 600 pF. The Cooknell CA6/C charge amplifier, which provides its own well regulated variable bias supply of 100 V, has a flat frequency response from 100 kHz to 20 MHz, a low noise input, and a sensitivity of 250 mV/pC. The Panametrics 5660B preamplifier has a bandwidth at (-3 dB) of 20 kHz - 2 MHz with an equivalent input noise of 5 $\mu V_{\text{peak-to-peak}}$. The maximum output voltage is 2 $V_{\text{peak-to-peak}}$ into a 50 Ω load. Its gain can be set to 40 dB or 60 dB. The RITEC BR640 receiver's bandwidth is 100 kHz - 50 MHz with a maximum gain of 64 dB when it is operating with a 50 Ω load. The gain can be changed with steps of 4 dB in the range -12 dB to 64 dB.

Capacitive foil transducers

The capacitive foil air-coupled transducers are schematically presented in fig. 2.2. The micro-machined backplate has a well defined pit geometry. The detailed manufacturing process is explained in detail by Schindel [90]. The pits, which have an average diameter of 40 μm and depth of 35 μm are periodically distributed over a grid with unit size 80 μm . A DC bias is applied to hold the metalized film and to squeeze out the air between the membrane and the backplate. The pressure sensitivity of this device reported by the manufacturer [90] is 0.7 mV/Pa. The characteristics and performance of this type of probe are influenced by the roughness of the backplate, the metalized dielectric film, the bias voltage and the transient excitation.

As previously mentioned, Carr and Wykes [18] found several possible transduction mechanisms for air-coupled probes: membrane resonances, drumhead modes, and quarter-wavelength resonances of waves in air in the pits. The resonant frequency and

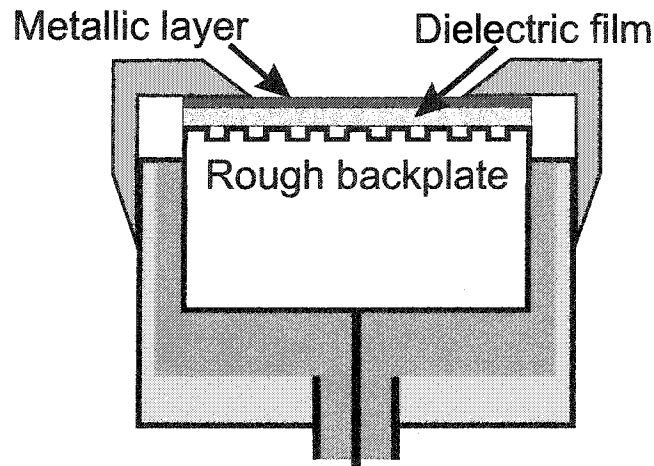


Figure 2.2 Schematic section of an air-coupled capacitive foil transducer. The disks of the capacitor are the micro machined backplate (controlled roughness) and the metallic layer on the dielectric film.

the bandwidth of the transducer are determined by the superposition of these mechanisms. Also, the membrane's mass and stiffness affect the amplitude and frequency dependence of the vibrations. To detect small amplitude oscillations in air, the detector's membrane needs to be light. Therefore, the sensitivity of the detector is increased with a decrease of the film thickness for the same metallic layer. The thinnest dielectric film (Mylar/Kapton) commercially available has a thickness of $2.5\text{ }\mu\text{m}$ and is offered with gold or aluminum metal layer. Taking into account that the average thickness of a metallic layer is about $1000\text{ }\text{\AA}$, the mass is estimated to be for the gold layer, 1.9 g/m^2 and for the aluminum layer 0.3 g/m^2 . The mass of a $2.4\text{ }\mu\text{m}$ Mylar film is 3.3 g/m^2 ; the mass of a Mylar membrane is then 5.2 g/m^2 with gold layer (37% gold, 67% Mylar), but is only 3.6 g/m^2 with aluminum layer (7% aluminum, 93% Mylar). The aluminum layer is preferred over gold because its weight is lower so that it produces higher sensitivity and larger bandwidth for the detector. The stiffness of the membrane is controlled through

the bias voltage; a higher bias increases the stiffness and produces a larger bandwidth.

The attenuation of ultrasonic waves in air above 500 kHz increases with the square of the frequency, with the square root of the temperature, and with the atmospheric pressure, while below 500 kHz, humidity is an additional factor [17]. For example a propagating wave in air at 1 MHz is attenuated with 160 dB/m. Therefore, the transmitter needs to generate enough energy for the ultrasonic wave to travel through the air and eventually to couple guided waves into the sample. The transient voltage excitation necessary to produce the desired air-coupled wave has a peak-to-peak amplitude of 400-500 V, and is applied with the negative DC bias over the capacitive transducer's plates. In order to prevent generation of nonlinear effects in the membrane vibration, the amplitude of the bias has to exceed the maximum amplitude of the excitation. Thus, the transmitter's dielectric film must be able to sustain transient voltages with peak-to-peak amplitudes twice the value of the bias voltage. Because of the tenuous nature of air and the extremely poor energy coupling to most materials, any air-coupled ultrasonic experiment demands a high-energy generation of the acoustic waves into the air for the transmitter and a high sensitivity for the detector. Thus, the transmitter must be able to accommodate higher transient and bias voltages than the receiver; for this reason, the transmitter must accommodate a thicker dielectric film ($10 - 15 \mu\text{m}$) than the receiver ($2 - 5 \mu\text{m}$).

The voltage across a dielectric material, thus the field within, cannot be infinitely increased; eventually a threshold is reached for which a substantial current flow appears between electrodes. This limit is called dielectric breakdown. In liquid or gaseous dielectrics the breakdown does not generally causes a permanent damage of the media, however, in solid dielectrics the breakdown invariably produces a permanent damage. The dielectric strength is the maximum voltage that can be applied to a dielectric without causing dielectric breakdown. The dielectric strength depends on a variety of factors such as the amplitude of the voltage, duration and frequency of the applied transients,

molecular structure of dielectric, nature of electrodes, temperature, and humidity [52]. There are also aging effects that produce reduction of the dielectric strength. In the case of a solid dielectric there are various type of breakdown that can occur separate or simultaneously. The most common type is the one known as the intrinsic, electronic, or electron avalanche breakdown, where free electrons in the conduction band are accelerated by the electric field, which exists between electrodes, and ionize a host of atoms producing an avalanche of other free electrons and eventually a substantial current flow inside the dielectric. Another mechanisms are the thermal breakdown, internal discharges, external discharges, material aging and last but not least, the electromechanical breakdown. The latter type is significant when the elastic deformation of the dielectric cannot balance the compressional forces produced by electrostatic attraction between electrodes [52]. Even though the maximum dielectric breakdown voltage for Kapton and Mylar is high (approximately 300 kV/mm for Kapton and 400 kV/mm for Mylar), the voltage applied on the transducers was kept at a safe 10% of this value in all experiments to prevent the occurrence of any of type of dielectric breakdown.

Fig. 2.3 is a photograph of the active surface of a capacitive foil transducer. This particular probe is of interest because it shows degradation of the metallic layer. This transducer was still functional in the condition seen in fig. 2.3, but its performance was reduced to 20%-30% of its performance in its original state. Replacement of the dielectric film solved the problem and restored the probe's performance. We found film replacement to be simple and easy to perform. So far, there are no reports in the literature of factors producing failure of the metalized film. Identification of the mechanisms that produce such failure needs further research, but this is not our purpose in the present study.

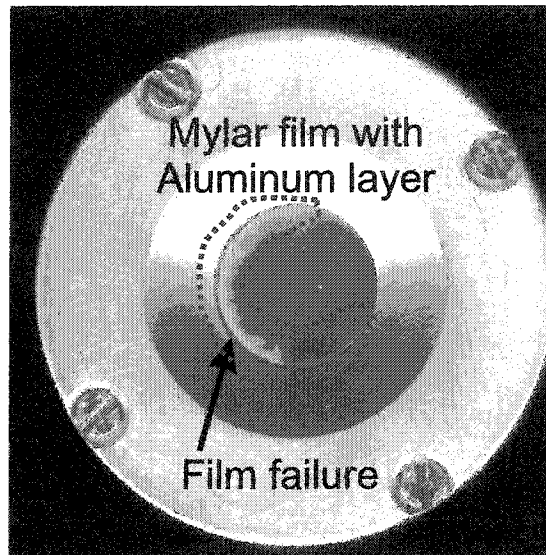


Figure 2.3 Photo of an actual capacitive foil transducer. The active surface of the probe is approximately 10 mm. The dotted curve identifies the area where the metalized dielectric membrane is altered.

Focusing mirror

One important advantage of using air-coupled ultrasonics is that we can exploit even weakly focused beams to produce a relatively large angular range inside most engineering materials. This is possible because of the difference in the acoustic impedances of air and various samples (e.g., $Z_{air}=400$ Rayl, $Z_{aluminum}=17.66$ MRayl, $Z_{lucite}=3.2$ MRayl, $Z_{water}=1.48$ MRayl). According to the coincidence principle or the phase matching condition, an incident acoustic beam of about 20° angular spread will excite the majority of phase-match angles simultaneously in most materials (i.e., metals, plastics, carbon and glass fiber composites). In the case of the metals, 10° is sufficient to couple the energy into the sample, for example an incident angular beam spread of 7.8° (second critical angle) will excite all phase-match angles in an aluminum plate, an incident angle that is any higher will produce total reflection back into the surrounding air.

The actual capacitive foil transducers that we use have planar active elements. To

increase their angular range, we designed a focusing device, an acoustic mirror, for both transmitter and receiver. In fig. 2.4 one of the acoustic mirrors is shown in light gray, while the planar capacitive probe is dark blue and the rays generated by the active element in the plane (x, z) are red color. The focusing mirrors have a cylindrical parabolic shape that provides a quasi-line focus along y -axis. The transducer's acoustical axis is parallel to the x -axis before being reflected by the mirror and parallel to the z -axis after reflection. The focusing mirrors were designed with a 3D CAD software SolidWorks to produce an angular beam spread of $\Delta\theta = 16^\circ$.

Fig. 2.5 presents the measured angular beam spread of the transducer/mirror system; the white portion represents the high value and the black portion the low value of the amplitude of the acoustic pressure. The acoustic field of the focused transducer/mirror system has been measured at equally spaced locations along x -axis in the focal plane ($z=0$) with a point receiver. A planar capacitive foil transducer with a 0.1-0.2mm mask (open cell foam) was employed to simulate the quasi-point receiver. A 2D FFT transforms the raw data (time-space) into the spectrum (wavenumber k - frequency f) shown in fig. 2.5. The acute angle (solid lines) approximates the angular beam spread of the focused probe ($\Delta\theta \sim 16^\circ$). A complete description of the experimental procedure can be found later in this chapter.

A rapid prototyping process, stereo lithography, was used in producing the physical objects from the 3D computer model. Stereo lithography, or SLA, creates a tangible three-dimensional physical object from a CAD drawing, by directing ultraviolet laser radiation onto a vat of photosensitive polymer resin. The resin, DuraFormTM Nylon glass-filled (GF), is cured, layer-by-layer, with a computer-controlled laser. The vertical resolution of the laser is 0.001 mm but the layers' resolution is 0.025 mm, dependant upon geometry, build parameters and material. After being cured in an ultraviolet oven, each piece is hand-polished and finished to specifications. The surface finish of the acoustic mirrors is obtained to be approximately $1.0 \mu\text{m}$.

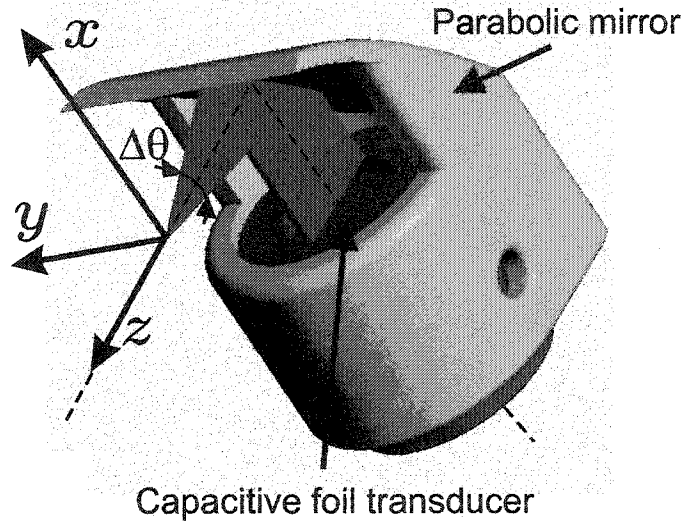


Figure 2.4 SolidWorks 3D computer model of the acoustic mirror. The planar electrostatic transducer is shown in dark gray, while the planar capacitive probe is dark blue and the reflected and focused rays are red.

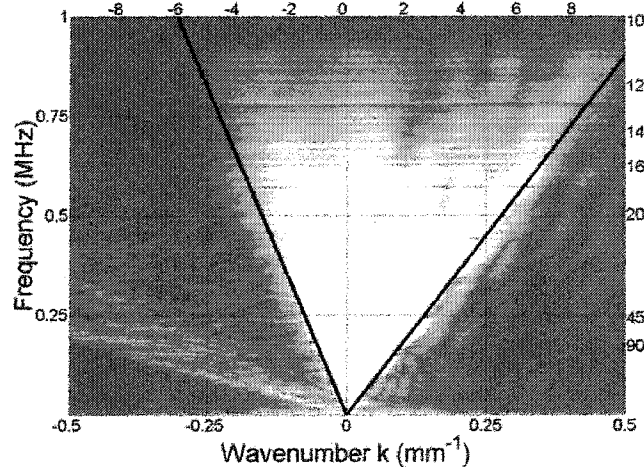


Figure 2.5 The measured spectrum of the focused probe. The pressure field is sampled at equally spaced position in the focal plane. A 2D FFT transforms the (time-space) data into (wavenumber k - frequency f) spectrum. The spectrum has its amplitude color-coded, with white representing the highest value while black corresponds to the lowest amplitude. The acute angle approximates the angular beam spread of the focused probe.

To obtain a similar shape of the acoustic beam, the system planar foil transducer - parabolic mirror can be replaced by a focused probe with the following characteristics: beam waist at aperture $W_0 \approx 10$ mm and focal length $F_0 \approx 26.5$ mm. These are the parameters used in the complex transducer point model for the numerical evaluation of the received voltage.

Data acquisition and signal processing

The transmitter's pressure field is sampled with a quasi-point receiver at discrete locations in the plane, which contains the transmitter's acoustic axis. As presented in fig. 2.6, the acoustic axis points in the z -direction while the active surface of the probe rests in the (x, y) plane. For discrete z_n positions, a line scan is performed along the x -axis and the signal is recorded for equally spaced x_m positions. The m and n are the number of equally spaced steps along the x - and z -axis respectively. The directivity pattern measurement consists then in implementing a (m, n) grid scan and recording individual waveforms $\mathcal{W}(t, x_m, z_n)$ for every node of the grid (m, n) . After the desired number of waveforms $\mathcal{W}(t)$ have been recorded, a Fourier transform of the time domain signal is computed for each location. Next the amplitudes of a specific frequency are extracted from the spectra for every (x_m, z_n) of the scan. This three-dimensional data set $(x_m, z_n, A_F(x_m, z_n))$ represents the mapping of the directivity pattern of the transmitter.

For each step of the scan, the measurement parameters (i.e., position, excitation, reception) are controlled through the GPIB interface by LabView virtual instrument software. The excitation signal is produced by a RAM 10000 system, and is a tone-burst with a user-controlled frequency, number of cycles, and amplitude. The frequency can be dynamically changed to cover the entire useful bandwidth of the probe in discrete steps. For covering the bandwidth 0.5-1.5 MHz, 20 tone bursts were used.

The acquisition is done through the A/D converter of the oscilloscope and the raw data is then downloaded onto the PC hard disk. The LabView interface produces real

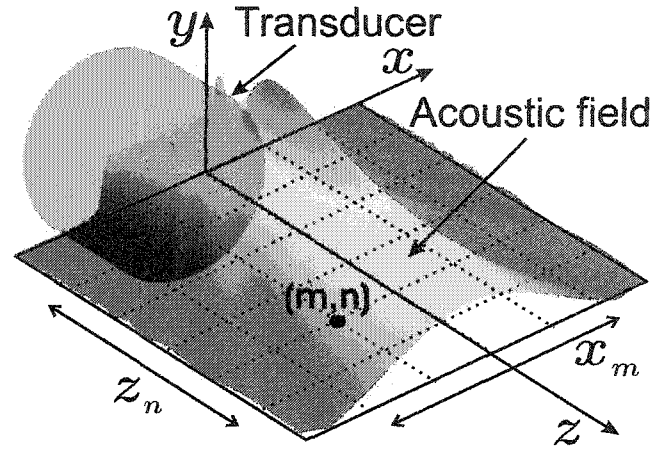


Figure 2.6 The grid scan for acoustic pressure measurement. The color-coded 3D plot represents a typical profile of a planar transducer. The red color corresponds to high amplitude and the dark blue to low amplitude acoustic pressure. The z -axis is the acoustical axis of the transducer.

time data processing and analysis. Because of the very weak signals involved in an air-coupled experiment, the signal is amplified to the maximum possible value allowed by the amplifiers' saturation thresholds. In spite of this, the typical S/N ratio is so small that signal averaging is required. The averaging reduces the white noise and improves the S/N ratio, but all the other noise sources remain present in the signal. For the directivity pattern measurement, in which the sound travels relatively short distances in air, the system and the procedure are satisfactory. This experimental system is, however, impractical for the mechanical property evaluation, being slow in data acquisition and processing.

Transducer model

Direct calculation of a piston-like transducer's field is performed by summing the contributions of infinitesimal area elements on the surface of the transducer at an ar-

bitrary location in the coupling fluid. The received voltage is obtained according to reciprocity expressions of Auld [8] and Kino [53] as a sum of the transmitter's field over the receiver's surface, weighted by the receiver's directivity function. The numerical evaluation of the voltage integral can be complicated and time-consuming. However, it has been shown by Lobkis and Chimenti [65], [26], and Lobkis *et al.* [63] that the received voltage is not altered but the numerical evaluations are substantially simplified if the transducers' pressure field are approximated with Gaussian beams. Furthermore, Zeroug *et al.* [99] and Fei and Chimenti [33] showed that the expression of the received voltage is simplified even more if the locations of transducers are translated into the complex plane and the finite transducers are replaced with point source and point receiver, respectively. The field profile of such complex source on the real axis is nearly identical to a Gaussian beam allowing the replacement of the transmitter with a complex point source and similarly, because of reciprocity considerations, the replacement of the receiver with a complex point receiver.

Piston model - planar and focused transducer

In a conventional ultrasonic experiment, using either pitch-catch or pulse-echo arrangements, the quantity accessible to our investigation is not the pressure, although it is related to it, but the voltage. For this reason, it is important to be able to model the output voltage for a two-transducers setup, one transmitting and the other receiving. All possible experimental arrangements are particular cases for the relative location of this two transducers configuration. Let us consider the geometry shown in fig. 2.7 with the transmitter T located at $(d_0, 0, h)$ and the receiver R at $(-d_0, 0, h)$ in a pitch-catch arrangement and a test sample along the x -axis. For a pulse-echo setup, both transducers, the transmitter and receiver, would have the same location in the model. For simplicity of calculations, we consider the centers of both transducer to lie on the x -axis of the coordinate system, and we further consider that the upper sample surface coincides with

the plane $z = 0$. The angle that both transducers' acoustical axes have with respect to the normal to the sample is equal to α . The distance $2d$ would be the separation between the intersection points of the acoustical axis with the sample $d = d_0 - h \tan \alpha$.

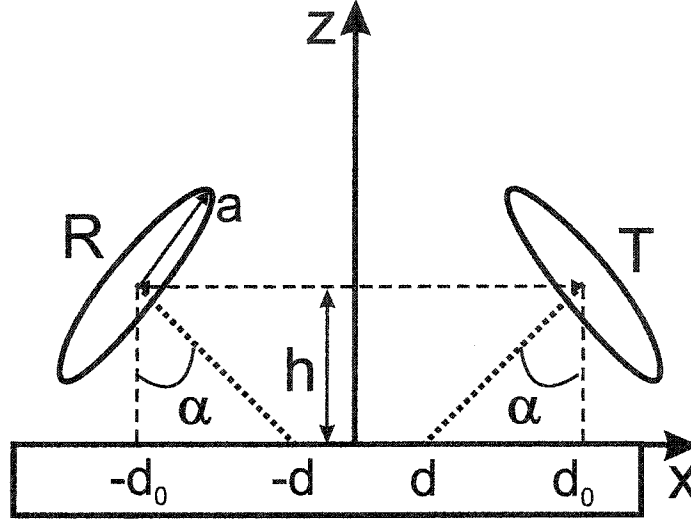


Figure 2.7 Planar piston transducer model. Geometry for calculating the output voltage for two transducers in reflection setup.

For convenience, let us use the notation S_T and S_R for the surface of the transmitter and the receiver, respectively. The distance between the point P and a point A on the surface of the transmitter will be given by $r = \sqrt{(x_T - x)^2 + (y_T - y)^2 + (z_T - z)^2}$. According to the Rayleigh formula, the pressure field of an incident ultrasonic wave produced by the transmitter T at an arbitrary point $P(x, y, 0)$ on the sample plate surface can be obtain according to Schmerr [92] (equations (8.8) and (8.9) on page 159) as

$$p^{inc} = \frac{-i\omega\rho_f}{2\pi} \iint_{S_T} v_z(A, \omega) \frac{e^{i\vec{k}\cdot\vec{r}-\omega t}}{r} dS_T(A) \quad (2.1)$$

where ω is the circular frequency, ρ_f is the fluid's density, k is the wavenumber and $v_z(A, \omega)$ is the velocity distribution. The expression for the pressure field presented in (2.1) is valid for any particle velocity distribution on the surface S_T . In the case

of a piston transducer, the velocity distribution is constant over the surface S_T of the transducer ($v_z(A, \omega) = v_0(\omega)$ on S_T and $v_z(A, \omega) = 0$ elsewhere), and following Schmerr's approach the expression of the pressure is simplified to

$$p^{inc} = \frac{-i\omega\rho_f v_0}{2\pi} \iint_{S_T} \frac{e^{i\vec{k}\cdot\vec{r}-\omega t}}{r} dS_T \quad (2.2)$$

for the piston planar transducer's pressure field at an arbitrary point B . For the rest of the calculation, the term $e^{-\omega t}$ will be ignored for simplicity. In order to find the reflected pressure field at the sample-fluid interface, Brekhovskikh's expansion of an incident spherical wave into plane waves [16] will be used in the following calculation. The spherical wave e^{ikr}/r is expressed in terms of plane waves by Brekhovskikh (equation (18.19) on page 240) as

$$\frac{e^{ikr}}{r} = \frac{ik}{2\pi} \int_0^{2\pi} d\varphi \int_0^{\pi/2-i\infty} e^{ikz_T \cos\theta + ik \sin\theta[(x_T-x)\cos\varphi + (y_T-y)\sin\varphi]} \sin\theta d\theta, \quad (2.3)$$

with θ the angle between the wave vector \vec{k} and the z -axis and φ the angle between the x -axis and the projection of \vec{k} on the (x, y) plane. The projections of the wave vector are expressed as $k_x = k \sin\theta \cos\varphi$, $k_y = k \sin\theta \sin\varphi$ and $k_z = k \cos\theta$ with $k_z = \sqrt{k^2 - k_x^2 - k_y^2}$. The integration with respect to φ is performed between the limits $(0, \pi)$. Because the z -axis projection of the wave number k_z can vary from $k_z = k$ for $k_x = k_y = 0$ to $k_z = i\infty$ for $k_x \rightarrow \pm\infty$ or $k_y \rightarrow \pm\infty$, the integration with respect to θ must be performed on a complex contour from $\theta = 0$ to $\theta = \pi/2 - i\infty$. Substituting (2.3) in (2.2), we obtain the incident pressure field of the transducer as

$$p^{inc} = \frac{\omega\rho_f k v_0}{(2\pi)^2} \iint_{S_T} dS_T \int_0^{2\pi} d\varphi \int_0^{\pi/2-i\infty} e^{ikz_T \cos\theta + ik \sin\theta[(x_T-x)\cos\varphi + (y_T-y)\sin\varphi]} \sin\theta d\theta. \quad (2.4)$$

When the variables that depend only on the geometrical location of the transducer are rearranged, the incident pressure field at an arbitrary point P on the sample surface will be given by

$$p^{inc} = \frac{\omega\rho_f k v_0}{(2\pi)^2} \int_0^{2\pi} d\varphi \int_0^{\pi/2-i\infty} D_T(\theta, \varphi) e^{-ikx \sin\theta \cos\varphi -iky \sin\theta \sin\varphi} \sin\theta d\theta, \quad (2.5)$$

where

$$D_T(\theta, \varphi) = \iint_{S_T} e^{ikz_T \cos \theta + ik \sin \theta (x_T \cos \varphi + y_T \sin \varphi)} dS_T \quad (2.6)$$

is the directivity function of the transmitter and depends on the transducer's size and location. Equation (2.5) is the plane wave representation (with θ the incident angle) of the planar transducer field in the plane $z = 0$. Upon reflection, the amplitude of each incident plane wave is modified by the reflection coefficient $R(\theta)$ and the phase changes as the waves are reflected, yielding the reflected pressure field expression at an arbitrary point (x, y, z) as

$$p^{ref} = \frac{\omega \rho_f k v_0}{(2\pi)^2} \int_0^{2\pi} d\varphi \int_0^{\pi/2-i\infty} R(\theta) D_T(\theta, \varphi) e^{ikz \cos \theta - ik \sin \theta (x \cos \varphi + ky \sin \varphi)} \sin \theta d\theta. \quad (2.7)$$

By allowing the arbitrary point (x, y, z) to be located on the receiver surface S_R at (x_R, y_R, z_R) , we obtain the expression of the pressure field on the receiver's active element as

$$p^{ref}(\vec{r}_R) = \frac{\omega \rho_f k v_0}{(2\pi)^2} \int_0^{2\pi} d\varphi \int_0^{\pi/2-i\infty} R(\theta) D_T(\theta, \varphi) e^{ikz_R \cos \theta - ik \sin \theta (x_R \cos \varphi + ky_R \sin \varphi)} \sin \theta d\theta. \quad (2.8)$$

The voltage V_{recv} that is generated on the receiver's surface S_R that samples the transmitter's acoustic field is obtained according to reciprocity expressions of Auld [8] and Kino [53] as

$$V_{recv} = F(\omega) \iint_{S_R} p^{ref}(\vec{r}_R) dS_R, \quad (2.9)$$

with $F(\omega)$ a coefficient that depends on the frequency and fluid medium. Substituting (2.8) in (2.9), we obtain the voltage on the receiver in a similar fashion as equation (6) of Lobkis *et al.* [62]

$$V_{recv} = F(\omega) \int_0^{2\pi} d\varphi \int_0^{\pi/2-i\infty} R(\theta) D_T(\theta, \varphi) D_R(\theta, \varphi) \sin \theta d\theta, \quad (2.10)$$

with

$$D_R(\theta, \varphi) = \iint_{S_R} e^{ikz_R \cos \theta - ik \sin \theta (x_R \cos \varphi + y_R \sin \varphi)} dS_R \quad (2.11)$$

the directivity function of the receiver that depends on the transducer's size and location. Thus the problem of finding an analytical expression for the received voltage depends on the calculation of the transducer's directivity functions D_T and D_R .

We shall consider, for simplicity, a polar coordinate system on the transmitter surface such that the Cartesian coordinates (\bar{x}, \bar{y}) that define the surface S_T are transformed into $\bar{x} = \rho \cos \varphi_T$ and $\bar{y} = \rho \sin \varphi_T$, respectively. The coordinates of a point (x_T, y_T, z_T) on the surface S_T will be given by $x_T = d_0 + \rho \cos \alpha \cos \varphi_T$, $y_T = \rho \sin \varphi_T$ and $z_T = h - \rho \sin \alpha \cos \varphi_T$ with the $(d_0, 0, h)$ the center of the transmitter. Then the directivity function D_T can be expressed as

$$D_T(\theta, \varphi) = C \int_0^a \rho d\rho \int_0^{2\pi} d\varphi_T e^{ik\rho[(\cos \alpha \sin \theta \cos \varphi - \sin \alpha \cos \theta) \cos \varphi_T + \sin \theta \sin \varphi \sin \varphi_T]}, \quad (2.12)$$

with $C = e^{ikh \cos \theta + ikd_0 \sin \theta \cos \varphi}$. If the notation $\cos \beta = \cos \alpha \sin \theta \cos \varphi - \sin \alpha \cos \theta$ and $\cos \gamma = \sin \theta \sin \varphi$ is introduced, the phase term from equation (2.12) $\psi(\varphi_T) = \cos \alpha \sin \theta \cos \varphi - \sin \alpha \cos \theta) \cos \varphi_T + \sin \theta \sin \varphi \sin \varphi_T$ can be rewritten as

$$\psi(\varphi_T) = \cos \beta \cos \varphi_T + \cos \gamma \sin \varphi_T = \sqrt{\cos^2 \beta + \cos^2 \gamma} \cos(\varphi_T - \tilde{\varphi}), \quad (2.13)$$

with $\sin \tilde{\varphi} = \cos \gamma / \sqrt{\cos^2 \beta + \cos^2 \gamma}$ and $\cos \tilde{\varphi} = \cos \beta / \sqrt{\cos^2 \beta + \cos^2 \gamma}$. The physical interpretation of the angles β and γ , just introduced, is shown in fig. 2.8. As already stated, it is implied in the above calculation that the acoustical axes of the transducers lie in the plane (x, z) . In the following calculation, we shall consider only the spatial beam spread of the transmitter to identify the angles β and γ . The vector \vec{r} has its direction along the acoustical axis of the transducer (versor $e_r = \vec{r}/r$) and α is the incident angle, or in other words $\alpha = \widehat{(\vec{r}, -\hat{k})}$ the angle between the normal to the sample's plane (x, y) and the acoustical axis \vec{r} of the transducer. The vector $\vec{\rho}$ has its direction (versor $e_\rho = \vec{\rho}/\rho$) along an arbitrary plane-wave direction of propagation (θ, φ) in three dimensions. The angle θ is the angle between the arbitrary plane wave direction e_ρ and the normal to the sample, $\theta = \widehat{(\vec{e}_\rho, -\hat{k})}$ and φ is the angle between the projection

with $J_0(k\rho\sqrt{\cos^2\beta + \cos^2\gamma})$ the Bessel function of the first kind [6]. The directivity function D_T can be simplified to an expression much the same as equation (7) of Lobkis *et al.* [62]

$$D_T(\theta, \varphi) = \pi a^2 e^{ikh \cos \theta + ikd_0 \sin \theta \cos \varphi} \left[\frac{2J_1(ka\sqrt{\cos^2\beta + \cos^2\gamma})}{ka\sqrt{\cos^2\beta + \cos^2\gamma}} \right], \quad (2.17)$$

with $\cos\beta = \cos\alpha \sin\theta \cos\varphi - \sin\alpha \cos\theta$ and $\cos\gamma = \sin\theta \sin\varphi$. Furthermore, if we consider the notation $\sin\delta = \sqrt{\cos^2\beta + \cos^2\gamma}$, which yields $\cos\delta = \sqrt{1 - \cos^2\beta - \cos^2\gamma} = \sin\theta \sin\alpha \cos\varphi + \cos\theta \cos\alpha$, we can make the observation that the angle δ is precisely the angle between the arbitrary plane-wave direction \hat{e}_ρ and the transmitter's acoustical axis \hat{e}_r .

$$\begin{aligned} \hat{e}_\rho \cdot \hat{e}_r &= (\sin\theta \cos\varphi \hat{i} + \sin\theta \sin\varphi \hat{j} - \cos\theta \hat{k}) \cdot (\sin\alpha \hat{i} + 0\hat{j} - \cos\alpha \hat{k}) \\ &= \sin\theta \sin\alpha \cos\varphi + \cos\theta \cos\alpha = \cos\delta \end{aligned} \quad (2.18)$$

Performing the calculation of the receiver's directivity a similar expression can be obtained; for identical transducers we expect the directivity to be the same, $D_R = D_T$. Hence, for identical transducers, the expression of the received signal V_{recv} can be simplified to

$$V_{\text{recv}} = F(\omega) \int_0^{2\pi} d\varphi \int_0^{\pi/2-i\infty} R(\theta) \left[\frac{2J_1(ka \sin\delta)}{ka \sin\delta} \right]^2 e^{2ikh \cos \theta} e^{2ikd_0 \sin \theta \cos \varphi} \sin \theta d\theta, \quad (2.19)$$

with $F(\omega)$ a coefficient that depends on the frequency and fluid medium. The equation (2.19) is the same as the voltage formula previously obtained by Lobkis *et al.* [62] (equation (8)). The numerical evaluation of the received voltage can be substantially simplified without losing accuracy if the piston beams are replaced by Gaussian beams in the received voltage expression, as was shown by Lobkis and Chimenti [65]. Later in the chapter the expression (2.19) modified with the Gaussian directivity is used for numerical predictions of the pressure field profile.

Now let us consider the geometry, presented in fig. 2.9, with two focused transducers in a confocal geometry. The expression (2.2) will be used to describe the pressure field

at point B on the left surface of the sample with velocity profile given by $v(\theta) = v_0 \mathcal{P}(\theta)$. Here, the function $\mathcal{P}(\theta)$ is the pupil function that describes the spatial-frequency or angular pass-band region and is given by the following relation

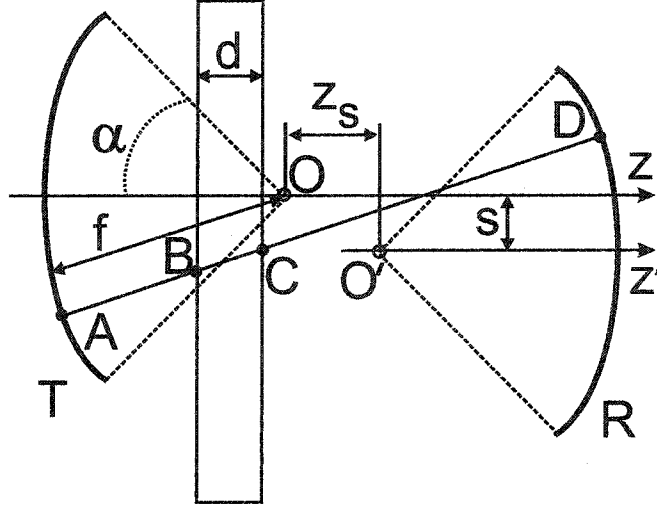


Figure 2.9 Focused piston transducer model. System of two focused transducers in confocal geometry.

$$\mathcal{P}(x, y) = \begin{cases} 1 & \text{if } \sqrt{\frac{x^2 + y^2}{f^2}} \leq \frac{1}{2} \sin 2\alpha \\ 0 & \text{otherwise} \end{cases} \quad \text{or} \quad \mathcal{P}(\theta) = \begin{cases} 1 & \text{if } (\pi - \alpha) \leq \theta \leq (\pi + \alpha) \\ 0 & \text{otherwise} \end{cases}$$

The element of area on the active surface of the transmitter is $dS_T = f d\theta_T dy$ for a cylindrical probe with its axis of symmetry along the y -axis and is $dS_T = f^2 \sin \theta_T d\theta_T d\varphi_T$ for a spherical focused probe. Thus, using the Rayleigh integral, as we have done before, the pressure field at point B will have the expression

$$p_B = \text{coeff.} \int_{S_T} \frac{e^{ik\rho}}{\rho} \mathcal{P}(\theta_T) dS_T,$$

where ρ is the distance between point A located on the transmitter surface, and B , on the sample. As previously mentioned, the plane wave decomposition of a spherical wave

is given according to Brekhovskikh by

$$\frac{e^{ik\rho}}{\rho} = \frac{ik}{2\pi} \int_0^{2\pi} d\varphi \int_0^{\pi/2-i\infty} e^{ik(z_B-z_T)\cos\theta+ik\sin\theta[(x_B-x_T)\cos\varphi+(y_B-y_T)\sin\varphi]} \sin\theta d\theta,$$

where (x_T, y_T, z_T) are the coordinates of point A and (x_B, y_B, z_B) the coordinates of point B , the pressure field at B has the expression

$$p_B = C \int_{S_T} dS_T \mathcal{P}(\theta_T) \int_0^{2\pi} d\varphi \int_0^{\pi/2-i\infty} e^{ik(z_B-z_T)\cos\theta+ik\sin\theta[(x_B-x_T)\cos\varphi+(y_B-y_T)\sin\varphi]} \sin\theta d\theta,$$

with C a frequency-dependent coefficient. The pressure field can be rewritten in terms of the directivity function as

$$p_B = C \int_0^{2\pi} d\varphi \int_0^{\pi/2-i\infty} D_T(\theta, \varphi) e^{ikz_B\cos\theta+ik\sin\theta(x_B\cos\varphi+y_B\sin\varphi)} \sin\theta d\theta \quad (2.20)$$

where the directivity function $D_T(\theta, \varphi)$ is given by

$$D_T(\theta, \varphi) = \int_{S_T} \mathcal{P}(\theta_T) e^{-ikz_T\cos\theta-ik\sin\theta(x_T\cos\varphi+y_T\sin\varphi)} dS_T \quad (2.21)$$

The equations (2.20) and (2.21) describe the plane wave representation of the incident pressure field of the transmitter at point B , arbitrarily located on the left surface of the sample. After the incident field is transmitted through the sample, the amplitude of the pressure field is modified by the transmission coefficient, and the phase is modified by the wave's path yielding the expression

$$p_C = C \int_0^{2\pi} d\varphi \int_0^{\pi/2-i\infty} D_T(\theta, \varphi) T(\theta) e^{ik(z_C-d)\cos\theta+ik\sin\theta(x_C\cos\varphi+y_C\sin\varphi)} \sin\theta d\theta \quad (2.22)$$

The term $T(\theta)$ is the transmission coefficient of plane waves traveling through the sample layer with thickness d . The coordinates of point C , which is located on the opposite side with respect to the transmitter, are (x_C, y_C, z_C) . Let us consider the pressure field that arrives on the receiver surface at point D with the coordinates (x_R, y_R, z_R) . Its expression can be calculated according to equation (2.22) as

$$p_D = C \int_0^{2\pi} d\varphi \int_0^{\pi/2-i\infty} D_T(\theta, \varphi) T(\theta) e^{ik(z_R-d)\cos\theta+ik\sin\theta(x_R\cos\varphi+y_R\sin\varphi)} \sin\theta d\theta. \quad (2.23)$$

So far, all the coordinates have been given in the system with the origin at the focus of the transmitter — point O (x_1, y_1, z_1) = (0, 0, 0). Let us consider that the focus of the receiver is located at point O' as presented in fig. 2.9, with coordinates (x_2, y_2, z_2). If we consider also a coordinate system that has its origin at O' , the coordinates of point D in this system will be (x'_R, y'_R, z'_R). Thus $x_R = x'_R + x_2$, $y_R = y'_R + y_2$ and $z_R = z'_R + z_2$, and the pressure field can be rewritten as

$$p_D = C \int_0^{2\pi} d\varphi \int_0^{\pi/2-i\infty} D_T(\theta, \varphi) T(\theta) e^{ik(z_2-d)\cos\theta + ik\sin\theta(x_2\cos\varphi + y_2\sin\varphi)} \times e^{ikz'_R\cos\theta + ik\sin\theta(x'_R\cos\varphi + y'_R\sin\varphi)} \sin\theta d\theta. \quad (2.24)$$

As previously mentioned, the received voltage can be obtained through a summation of the incident pressure field over the whole area of the receiver

$$V_{\text{recv}} = \text{coeff.} \int_{S_R} p_D \mathcal{P}(\theta_R) dS_R, \quad (2.25)$$

with $\mathcal{P}(\theta_R)$ as the pupil function of the receiver. Because of the symmetry of the transducer with respect to its acoustic axis, it would be easier to calculate the received voltage in the system of coordinates that has its origin in the focal point. The received voltage can be rewritten in the form

$$V_{\text{recv}} = \int_0^{2\pi} d\varphi \int_0^{\pi/2-i\infty} T(\theta) D_T(\theta, \varphi) D_R(\theta, \varphi) e^{ik(z_2-d)\cos\theta + ik\sin\theta(x_2\cos\varphi + y_2\sin\varphi)} \sin\theta d\theta, \quad (2.26)$$

where the frequency-dependent coefficient has been neglected and the transmitter directivity function is shown in equation (2.21). Similarly, the receiver's directivity function is given by

$$D_R(\theta, \varphi) = \int_{S_R} \mathcal{P}(\theta_R) e^{ikz'_R\cos\theta + ik\sin\theta(x'_R\cos\varphi + y'_R\sin\varphi)} dS_R. \quad (2.27)$$

For the case of a identical spherical focused probe, the two directivity functions are equal and can be expressed as

$$D_T(\theta, \varphi) = D_R(\theta, \varphi) = 2\pi f^2 \int_0^\alpha e^{ikf\cos\theta\cos\theta'} J_0(kf\sin\theta\sin\theta') \mathcal{P}(\theta') \sin\theta' d\theta'. \quad (2.28)$$

With the latter formula, the received voltage can be expressed then as

$$V_{\text{recv}} = F(\omega) \int_0^{\pi/2 - i\infty} T(\theta) D^2(\theta) J_0(ks \sin \theta) e^{ik(z_2 - d) \cos \theta} \sin \theta d\theta \quad (2.29)$$

where $s = \sqrt{x_2^2 + y_2^2}$ is the separation between the transducers' acoustical axis, z_2 is the distance between their focuses along the z -axis and $F(\omega)$ is a frequency-dependent coefficient. In the numerical evaluation of the received voltage, the replacement of the Bessel functions (piston radiators) with Gaussian beams has been justified by the work of Lobkis and Chimenti [65], [26]. The substitution of the piston radiator by a Gaussian beam in the expression of the pressure field is not desirable, however, when the representation of the side lobe structures of the radiated field is sought.

Complex transducer point

With the complex source point (CSP) model, an isotropic spherical wave is converted into a Gaussian beam in real space, when the coordinates of the source point are displaced into the complex plane. Therefore, the CSP models a finite, real Gaussian beam with a point source that has complex location. By reciprocity, measurement of an acoustic field with a finite, a Gaussian receiver can also be modeled by a point source receiver displaced at a complex location. If both the transmitter and receiver are replaced by CSPs, a method known as the complex transducer point (CTP), the combined Gaussian directivities are similar to the combination of two piston-like transducers. In fig. 2.10, two focused transducers are shown in a pitch-catch setup, arrangement that will be used for calculating the received voltage through the CTP method.

The field of a point source in an unbounded medium with location defined by the position vector \vec{r} is described by Green's function $G(\vec{r}) = \exp(i\vec{k}_f \cdot \vec{r})/4\pi\vec{r}$. The Green's function $G(\vec{r})$ is the solution of the inhomogeneous Helmholtz equation $(\nabla^2 + k_f^2)G(\vec{r}) = -\delta(\vec{r})$ with $k_f = \omega/c_f$ the wavenumber in the surrounding medium. Furthermore, in the case when the spherical wave is propagating through a sample plate, because

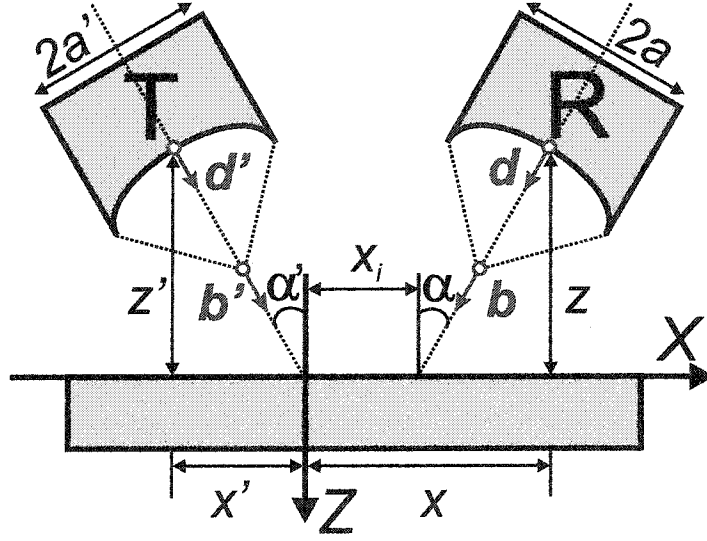


Figure 2.10 Complex transducer point model. Geometry for calculating the output voltage in a reflection setup.

the reflection/transmission coefficient that describes the pressure field after passing the sample is well-known for plane waves, it would be easier to use the plane-wave expansion of a spherical wave in the expression of the acoustic pressure of a point source. As we previously used Brekhovskikh's expansion of an incident spherical wave into plane waves for simplicity, for the same reason we now employ the Weyl expansion in the next steps,

$$\frac{e^{ik_f r}}{4\pi r} = \frac{1}{4\pi^2} \iint \left\{ \frac{i}{2k_z} e^{ik_z |z|} \right\} e^{i(k_x x + k_y y)} dk_x dk_y \quad (2.30)$$

with the source located in the coordinate system origin and $k_z = \sqrt{k_f^2 - k_x^2 - k_y^2}$ the z -axis projection of the wave vector \vec{k}_f and both real and imaginary parts positive $Re(k_z) \geq 0$ $Im(k_z) \geq 0$. If the source has a different location, for example point $\vec{r}_S = (x_S, y_S, z_S)$, the Weyl expansion is rewritten as

$$\frac{e^{ik_f |\vec{r} - \vec{r}_S|}}{4\pi |\vec{r} - \vec{r}_S|} = \frac{1}{4\pi^2} \iint \left\{ \frac{i}{2k_z} e^{-ik_x x_S - ik_y y_S + ik_z |z - z_S|} \right\} e^{i(k_x x + k_y y)} dk_x dk_y. \quad (2.31)$$

Let us consider the translation of both transducers from their real position to a complex location given by $\mathbf{r}' \rightarrow \tilde{\mathbf{r}}' = \mathbf{r}' + \mathbf{d}' + i\mathbf{b}'$ for the transmitter and $\mathbf{r} \rightarrow \tilde{\mathbf{r}} = \mathbf{r} + \mathbf{d} + i\mathbf{b}$

the receiver, respectively. The vectors $\mathbf{r}' = (x', y', z')$ and $\mathbf{r} = (x, y, z)$ define the position of the transducers' aperture centers; the vectors $\tilde{\mathbf{r}}'$ and $\tilde{\mathbf{r}}$ represent the CTP location; the vectors \mathbf{d}' and \mathbf{d} represent the Gaussian beam waist location relative to the aperture center for each probe and, finally, the vectors \mathbf{b}' and \mathbf{b} define the transducers' Fresnel length and beam direction.

Let us consider a point source that has been displaced from the real position \mathbf{r}_s to the complex position $\tilde{\mathbf{r}}_s$ according to the relation $\mathbf{r}_s \rightarrow \tilde{\mathbf{r}}_s = \mathbf{r}_s + \mathbf{d} + i\mathbf{b}$. The distance between the source and an arbitrary point (x, y, z) is

$$\mathcal{R}(\mathbf{r} - \mathbf{r}_s) = \sqrt{(x - x_s - d_x - ib_x)^2 + (y - y_s - d_y - ib_y)^2 + (z - z_s - d_z - ib_z)^2}.$$

For simplicity, let us consider that the real position of the source is at the origin $\mathbf{r}_s = (0, 0, 0)$ and both $\mathbf{d} = (0, 0, d)$ and $\mathbf{b} = (0, 0, b)$ have only z -axis projections. Thus $\mathcal{R}(\mathbf{r}) = \sqrt{x^2 + y^2 + (z - d - ib)^2} = \sqrt{x^2 + y^2 + (z_0 - ib)^2}$ with $z_0 = z - d$. If the point source field is estimated near the beam axis, we can assume that $\rho^2 = (x^2 + y^2) \ll (z_0^2 + b^2)$ and the distance $\mathcal{R}(\mathbf{r})$ can be approximated as

$$\begin{aligned} \mathcal{R}(\mathbf{r}) &= \pm \text{sign}(z_0)(z_0 - ib) \sqrt{1 + \frac{\rho^2}{(z_0 - ib)^2}} \\ \mathcal{R}(\mathbf{r}) &\approx \pm \text{sign}(z_0)(z_0 - ib) \left\{ 1 + \frac{\rho^2}{2z_0(1 + b^2/z_0^2)} + i \frac{\rho^2}{2b(1 + z_0^2/b^2)} \right\}. \end{aligned}$$

Substituting $\mathcal{R}(\mathbf{r})$ into the point source field equation we obtain

$$\frac{e^{ik_f \mathcal{R}(\mathbf{r})}}{4\pi \mathcal{R}(\mathbf{r})} \approx \frac{\pm \text{sign}(z_0) e^{k_f b}}{4\pi(z_0 - ib)} e^{\pm \text{sign}(z_0) i k_f \left(z_0 - \frac{\rho^2}{2z_0(1 + b^2/z_0^2)} \right)} e^{-k_f \left(\frac{\pm \text{sign}(z_0) \rho^2}{2b(1 + z_0^2/b^2)} \right)}. \quad (2.32)$$

In the case of the denominator of the fraction $1/\mathcal{R}(\mathbf{r})$, only the first term in the expansion was kept and the second, having $\rho^2/(z_0 - ib)$ in its expression, was ignored, but for the exponential, the first and second terms were kept and the rest in the expansion ignored because they contain $\rho^4/(z_0 - ib)^3$ and thus can be neglected as being insignificantly small. For this approximation to yield accurate results, it is not necessary that the higher order terms of the expansion be small, it is necessary only that they do not change the result significantly.

The exponential $\exp\{-k_f[\rho^2/2b(1 + z_0^2/b^2)]\}$ in equation (2.32) for $z > 0$ controls the amplitude of the point source like a Gaussian $\exp\{-\rho^2/W^2(z_0)\}$ in ρ near the axis $\rho = 0$. In fig. 2.11, the pressure field of a transducer modeled with the CTP method is evaluated at different positions along the z -axis and compared with the conventional piston radiator field. As we expected from equation (2.32), and shown in fig. 2.11, the field of a CTP projected on the real plane is nearly identical to a Gaussian, and the main lobe field distribution is similar for both models, however, the side lobes are not reproduced by the CTP model. In fig. 2.12 the pressure field is evaluated along the transducer's acoustical axis and compared with the conventional piston model. Although the near field pattern is not reproduced by the CTP model, the general shape of the pressure field is similar for both models.

The Gaussian beam's waist for a $1/e$ decrease in amplitude is given by $W(z_0) = W_0\sqrt{1 + z_0^2/b^2}$; thus, the term $b = k_f W^2/2$ is the critical Gaussian beam scaling parameter, which is called variously the Fresnel length or Rayleigh range, or for $2b$ the diffraction length, or the confocal parameter. From the expression of $W(z_0)$, we can find the Gaussian beam waist location relative to the aperture center to be $z = d$ when we impose the condition $W(z_0) = W_0$. When a transducer is replaced by a point source displaced into the complex plane, the geometrical parameters of the transducer's pressure field will need to be matched by those of the point source field. The beam width at the waist location W and the distance between the transducer aperture and waist location d are given by [94]

$$W = W_0 \frac{\beta}{\sqrt{1 + \beta^2}} \text{ and } d = \frac{F_0}{1 + \beta^2} \text{ with } \beta = \frac{2F_0}{k_f W_0^2}$$

F_0 is the focal length of the transducer, and W_0 is the beam width at the transducer aperture, estimated [94], [62] for measurements at a distance smaller or larger than Rayleigh distance a^2/λ to be $W_0 = 0.752a$ (a being the transducer radius).

From $b = k_f W^2/2$ and the above expressions the Fresnel length can be written in

term of the focal length F_0 as

$$b = \frac{k_f W_0^2}{2} \frac{\beta^2}{1 + \beta^2} = \frac{k_f W_0^2/2}{(k_f W_0^2/2F_0)^2 + 1} = \frac{b_0}{(b_0/F_0)^2 + 1}, \quad (2.33)$$

with $b_0 = k_f W_0^2/2$ the Fresnel length of a planar Gaussian transducer. By inspecting the equation (2.33) we observe that the parameter b varies with the focal length F_0 from 0 when $F_0 = 0$ (semi-spherical transducer) to b_0 when $F_0 \rightarrow \infty$ (planar transducer). The variation of the Fresnel length with the focal length F_0 is shown in fig. 2.13 as red solid line. Parameter b is strictly monotonically increasing with the focal length of the transducer having a point of inflexion at $F_0 = b_0/\sqrt{3}$ and an asymptotic limit of b_0 as F_0 approaches ∞ .

Similarly, the parameter d representing Gaussian beam waist location relative to the aperture center can be written in term of the focal length F_0 as

$$d = \frac{F_0}{1 + \beta^2} = \frac{F_0}{(F_0/b_0)^2 + 1}. \quad (2.34)$$

From the above equation (2.34), we find that parameter d increases with the focal length F_0 to its maximum for $F_0 = b_0$ after which asymptotically decreases to 0 as F_0 approaches ∞ , as shown in fig. 2.13 as blue solid line. A close examination of the equations (2.33) and (2.34) shows that parameters b and d interchange their behavior for constant value of the focal length F_0 and variable frequency ($b_0 = \pi f W_0^2/c_f$) from the case where the frequency, or b_0 , is constant while the focal length varies. In other words, for $F_0 = \text{const.}$ and $0 \leq f < \infty$, b increases with the frequency to its maximum for $f = c_f F_0/\pi W_0^2$ after which asymptotically decreases to 0 as frequency approaches ∞ ; d is strictly monotonically increasing with the frequency and has a point of inflexion at $f = c_f F_0/\pi W_0^2 \sqrt{3}$ and an asymptotic limit of $c_f F_0/\pi W_0^2$ as f approaches ∞ . The variations of b and d with the frequency has been previously studied by Zeroug *et al.* [99] who published an identical plot as fig. 2.13 but with the behavior of b and d interchanged as discussed above.

Variation of Fresnel length b and beam waist location d with focal length F_0 and their influence on 1/e contour plot of the acoustic pressure field for a 10-mm diameter focused transducer at 500kHz is shown in fig. 2.14. The 1/e pressure profile is evaluated for five focal lengths F_0 equal to: 26.5 mm (black), 37.4 mm (red), 64.7 mm (blue), 106.0 mm (green), 212.0 mm (magenta). The value $F_0 = 26.5$ mm corresponds to the focal length of the experimental transducer, $F_0 = 37.4$ mm is the point of inflection for b , and for $F_0 = 64.7$ mm d has a maximum $d = F_0/2 = b_0/2 = 32.4$ mm. As expected from equations (2.33) and (2.34), and fig. 2.13, the Fresnel length is increasing rapidly with the focal length to reach its asymptotic limit b_0 when $F_0 \rightarrow \infty$ for planar transducers. The parameter d increases rapidly to its maximum $b_0/2$ when $F_0 = b_0$ after which slowly decreases to zero; d equals zero for planar transducers. In fig. 2.15, the acoustic pressure field of a 10 mm diameter focused transducer operating in air at 500kHz is evaluated along acoustical axis z and in radial direction ρ . The 1/e decrease in amplitude is presented as a solid contour line along with the schematics for b and d to show their physical interpretation. For a Gaussian beam propagating in an elastic medium, the beam waist W has a minimum value W_0 at one place along the beam, known as the beam waist. The axial distance from the point of minimum beam waist W_0 to the point where the beam diameter has increased to $W_0\sqrt{2}$ is known as the Fresnel length or Rayleigh range and the parameter d represent the Gaussian beam waist location relative to the aperture center.

For the geometry presented in fig. 2.10 the real positions of the centers of the aperture of both the transmitter and receiver are displaced into the complex plane according to

$$\mathbf{r}' \rightarrow \tilde{\mathbf{r}}' = \mathbf{r}' + \mathbf{d}' + i\mathbf{b}'$$

$$\mathbf{r} \rightarrow \tilde{\mathbf{r}} = \mathbf{r} + \mathbf{d} + i\mathbf{b},$$

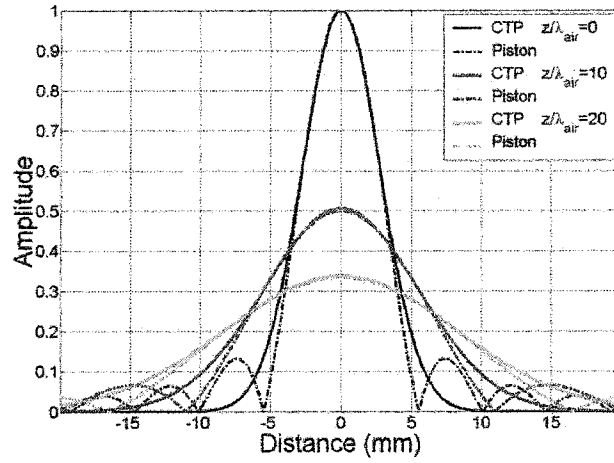


Figure 2.11 Comparison of the numerical evaluation of the pressure field of a 10 mm diameter planar transducer at 500kHz with the CTP (solid) and piston (dotted) model. The pressure field is evaluated on the x -axis at three different position ($z/\lambda_{air} = 0, 10$ and 20) along the z -axis that corresponds to the transducer's acoustical axis.

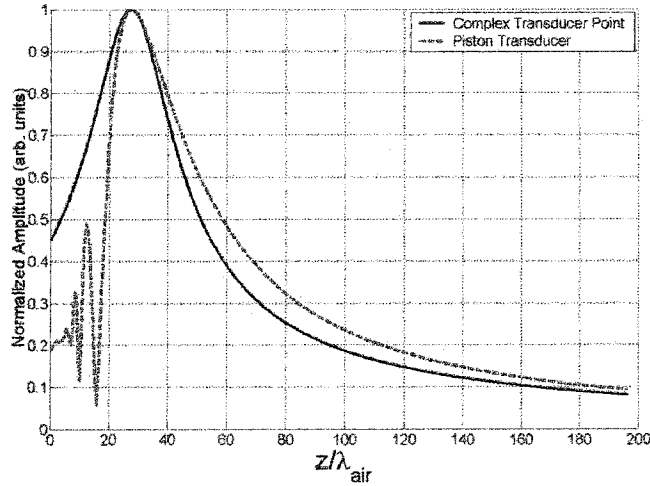


Figure 2.12 Pressure field of a 10 mm diameter focused transducer at 500kHz evaluated along acoustical axis with CTP (solid) and piston (dotted) model

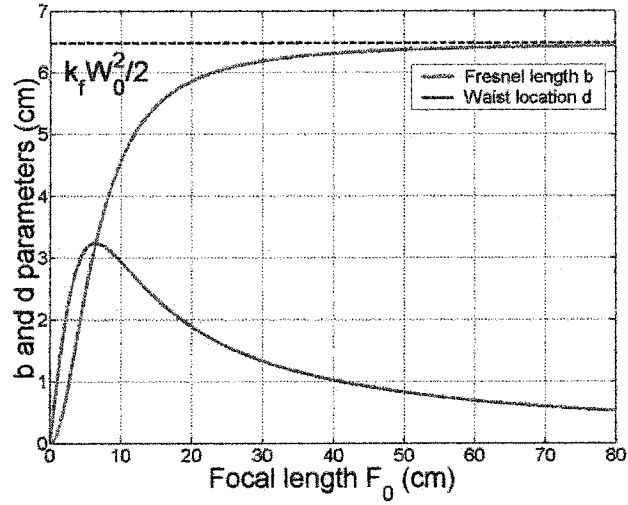


Figure 2.13 Variation of Fresnel length b and beam waist location d with focal length F_0 for 10-mm diameter focused Gaussian transducer with a $1/e$ waist width W_0 at 500 kHz.

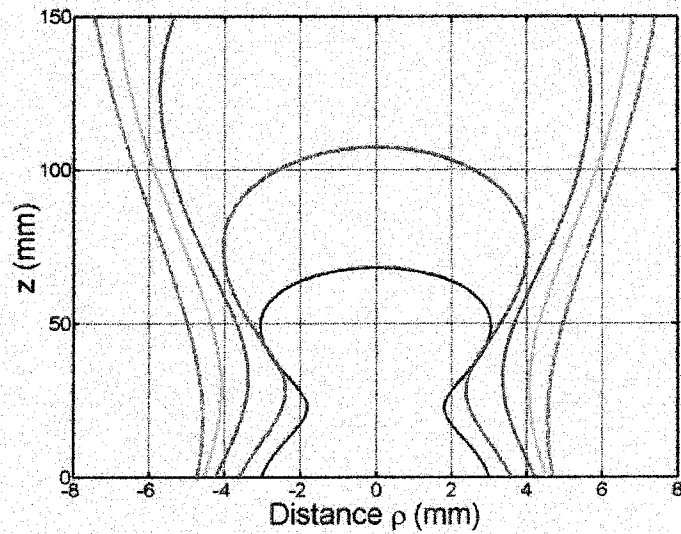


Figure 2.14 Variation of $1/e$ pressure field cross-section with focal length F_0 for 10 mm diameter focused transducer at 500kHz. The $1/e$ pressure profile is evaluated for focal length F_0 equals to: 26.5 mm (black), 37.4 mm (red), 64.7 mm (blue), 106.0 mm (green), 212.0 mm (magenta).

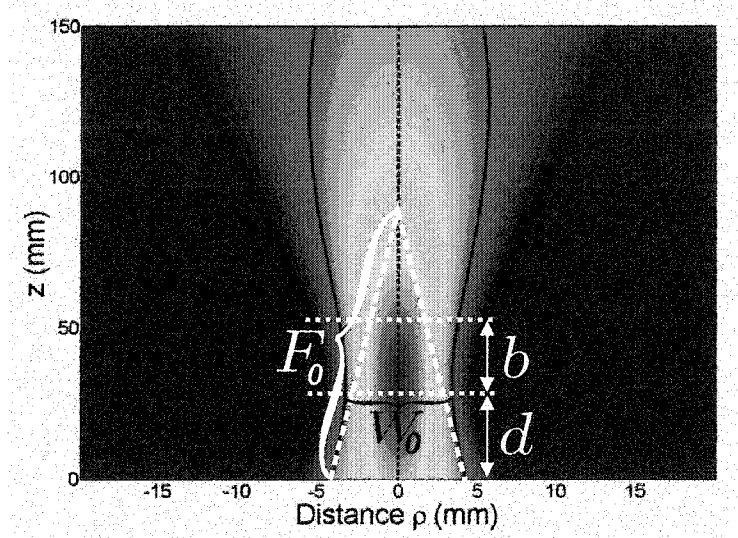


Figure 2.15 Pressure field of a 10 mm diameter focused transducer at 500kHz evaluated along acoustical axis z and in radial direction ρ . The solid black line represents $1/e$ contour plot of pressure field, d is the beam waist location and b the Fresnel length or Rayleigh range defined as the distance over which the beam radius spreads by a factor of $\sqrt{2}$.

or in the expanded form

$$\begin{aligned}\tilde{x}' &= x' + d' \sin \alpha' + ib' \sin \alpha' & \tilde{y}' &= y' & \tilde{z}' &= z' + d' \cos \alpha' + ib' \cos \alpha' \\ \tilde{x} &= x - d \sin \alpha - ib \sin \alpha & \tilde{y} &= y & \tilde{z} &= z + d \cos \alpha + ib \cos \alpha.\end{aligned}$$

The pressure field of the complex source point at the location of the complex point receiver is given by

$$p^{inc}(\tilde{\mathbf{r}} - \tilde{\mathbf{r}}') = i\omega\rho_f A_T G(\tilde{\mathbf{r}} - \tilde{\mathbf{r}}') = i\omega\rho_f A_T \frac{e^{ik_f \mathcal{R}(\tilde{\mathbf{r}} - \tilde{\mathbf{r}}')}}{4\pi \mathcal{R}(\tilde{\mathbf{r}} - \tilde{\mathbf{r}}')}.$$

and the voltage generated at the point receiver according to the Auld's reciprocity theorem [8] is given by

$$V_{\text{recv}}(\tilde{\mathbf{r}}, \omega) = i\omega\rho_f \gamma A_T A_R \frac{e^{ik_f \mathcal{R}(\tilde{\mathbf{r}} - \tilde{\mathbf{r}}')}}{4\pi \mathcal{R}(\tilde{\mathbf{r}} - \tilde{\mathbf{r}}')},$$

with A_T and A_R the dimensionless strength of the CTP and the γ a frequency-dependent parameter that depends upon the transducers' internal electronics [99]. With the expansion from equation (2.31) the received voltage can be expressed as

$$V_{\text{recv}}(\tilde{\mathbf{r}}, \omega) = -\frac{1}{8\pi^2} \omega \rho_f \gamma A_T A_R \iint_{-\infty}^{\infty} R(k_x, k_y, \omega) e^{ik_x(\tilde{x} - \tilde{x}') + ik_y(\tilde{y} - \tilde{y}') + ik_z|\tilde{z} - \tilde{z}'|} \frac{dk_x dk_y}{k_z}. \quad (2.35)$$

The term $R(k_x, k_y, \omega)$ is the plane-wave reflection coefficient of the sample plate shown in fig. 2.10. In the case of a transmission geometry, the reflection coefficient is simply replaced with the transmission coefficient, with the rest of the expression remaining unchanged. If no sample is in the path of the acoustic beam, the calculations are still valid, with the reflection or transmission coefficients equal to unity.

Equation (2.35) is the expression of the received signal for a specific frequency $f = \omega/2\pi$ sampled at the location $\tilde{\mathbf{r}}$. Now let's consider θ to be the angle between the direction of the wave vector k_f and the x -axis the projection of the wave vector on x , namely $k_x = k_f \sin \theta$. When a synthetic aperture coordinate scan is performed along the x -direction, the received voltage is sampled and recorded at discrete locations. The coherent summation of the signals for different positions along the x -axis is carried out

in the form of spatial Fourier transformation. The received voltage corresponding to the synthetic aperture coordinate scan in the x -direction is then given by

$$V_{\text{recv}}(k, \omega) = -\frac{\omega \rho_f \gamma A_T A_R}{8\pi^2} \iint_{-\infty}^{\infty} R(k_x, k_y, \omega) \frac{e^{ik_x(-d \sin \alpha - ib \sin \alpha - \tilde{x}') + ik_y(\tilde{y} - \tilde{y}') - ik_z(\tilde{z} + \tilde{z}')}}{k_z} \\ \times \left\{ \int_{-\infty}^{\infty} e^{i(k_x - k_f \sin \theta)x} dx \right\} dk_x dk_y.$$

Because the last term above in brackets is the Dirac delta function, the voltage formula becomes

$$V_{\text{recv}}(k, \omega) = -\frac{\omega \rho_f \gamma A_T A_R}{8\pi^2} \iint_{-\infty}^{\infty} R(k_x, k_y, \omega) \frac{e^{ik_x(-d \sin \alpha - ib \sin \alpha - \tilde{x}') + ik_y(\tilde{y} - \tilde{y}') - ik_z(\tilde{z} + \tilde{z}')}}{k_z} \\ \times 2\pi \delta(k_x - k_f \sin \theta) dk_x dk_y, \\ V_{\text{recv}}(k, \omega) = -\frac{\omega \rho_f \gamma A_T A_R e^{ik_f \sin \theta(-d \sin \alpha - ib \sin \alpha - \tilde{x}')}}{4\pi} \\ \times \int_{-\infty}^{\infty} R(k_f \sin \theta, k_y, \omega) \frac{e^{ik_y(\tilde{y} - \tilde{y}') - ik_z(\tilde{z} + \tilde{z}')}}{k_z} dk_y. \quad (2.36)$$

In practice, both transducers have their acoustical axis in the plane of the synthetic aperture coordinate scan; therefore, we can simplify the voltage expression for the case $y = y' = 0$. For an isotropic material, the reflection coefficient is not k_y dependent; thus the expression of the voltage is given by

$$V_{\text{recv}}(k, \omega) = -\frac{\omega \rho_f \gamma A_T A_R e^{ik_f \sin \theta(-d \sin \alpha - ib \sin \alpha - \tilde{x}')} R(k_f \sin \theta, \omega)}{4\pi} \int_{-\infty}^{\infty} \frac{e^{-ik_z(\tilde{z} + \tilde{z}')}}{k_z} dk_y.$$

Furthermore, if the transducers are cylindrically focused with a large angular beam spread in the plane of the synthetic aperture coordinate scan (x, z) but a small beam spread in the y -direction, the effect of the integration with respect of k_y becomes insignificant.

The equation (2.36) shows that a synthetic aperture coordinate scan produces only an averaged value for the reflected coefficient. In order to measure accurately the reflection

coefficient for a pair of arbitrarily oriented spherical transducers, another scan needs to be performed in the y -direction for each x -position of the synthetic aperture coordinate scan. The double spatial Fourier transform with respect to both x and y extracts all extrinsic influences in the received voltage expression

$$V_{\text{recv}}(k, \omega) = \iint_{-\infty}^{\infty} V_{\text{recv}}(x, y, \omega) e^{-ik_x x} e^{-ik_y y} dx dy, \quad (2.37)$$

or if the spherical coordinates are employed for convenience to express the wave vector projection $k_x = k_f \sin \theta_i \cos \phi_i$, $k_y = k_f \sin \theta_i \sin \phi_i$ and $k_z = k_f \cos \theta_i$. The pair (θ_i, ϕ_i) defines a plane wave from the Brekhovskikh's expansion,

$$V_{\text{recv}}(k, \omega) = \iint_{-\infty}^{\infty} V_{\text{recv}}(x, y, \omega) e^{-ik_f x \sin \theta_i \cos \phi_i} e^{-ik_f y \sin \theta_i \sin \phi_i} dx dy, \quad (2.38)$$

$$V_{\text{recv}}(k, \omega) = -\frac{\omega \rho_f \gamma A_T A_R}{2} R(k_f \sin \theta_i \cos \phi_i, k_f \sin \theta_i \sin \phi_i, \omega) \times e^{ik_f \sin \theta_i \cos \phi_i (-d \sin \alpha - ib \sin \alpha - \tilde{x}')} e^{-ik_f \tilde{y}' \sin \theta_i \sin \phi_i} \frac{e^{-ik_f \cos \theta_i (\tilde{z} + \tilde{z}')}}{k_f \cos \theta_i}. \quad (2.39)$$

The latter equation (2.39) shows that the absolute value of the received voltage is influenced by the Gaussian beams of both the transmitter and receiver. The reflection/transmission coefficient can be reconstructed, as will be shown later for a simplified case, if an additional scan is performed with the same geometrical setup but without the sample. The reflection/transmission coefficient is then obtained as the ratio of the received voltages with and without the sample, respectively. When the two-dimensional spatial scan is performed, the number of recorded waveforms increases from N to $N \times M$, where N and M are the number of steps along the x -axis and along the y -axis, respectively. The advantage of the two-dimensional spatial scan comes from the fact that all transducer beam effects are accounted for, and the received voltage is obtained through a 2D spatial and 1D temporal FFT applied on the scan data.

If any y -dependency is neglected, the problem reduces to a 2D case. Let us adopt the notation $k = k_x$ for the x -axis projection of the wavenumber. Thus $k_z = \sqrt{k_f^2 - k^2}$.

The received voltage is then given by

$$V_{\text{recv}}(x, \omega) = -\frac{1}{4\pi} \omega \rho_f \gamma A_T A_R \int_{-\infty}^{\infty} R(k, \omega) \frac{e^{ik(\tilde{x}-\tilde{x}')-i\sqrt{k_f^2-k^2}(\tilde{z}+\tilde{z}')}}{\sqrt{k_f^2-k^2}} dk. \quad (2.40)$$

The spatial Fourier transform of the received voltage corresponding to a synthetic aperture coordinate scan is obtained according to

$$V_{\text{recv}}(k, \omega) = \int_{-\infty}^{\infty} V_{\text{recv}}(x, \omega) e^{-ik_f x \sin \theta} dx. \quad (2.41)$$

Therefore, equation (2.41) becomes

$$\begin{aligned} V_{\text{recv}}(k, \omega) &= -\frac{\omega \rho_f \gamma A_T A_R}{4\pi} \int_{-\infty}^{\infty} R(k, \omega) \frac{e^{ik(-d \sin \alpha - ib \sin \alpha - \tilde{x}') - i\sqrt{k_f^2-k^2}(\tilde{z}+\tilde{z}')}}{\sqrt{k_f^2-k^2}} \\ &\quad \times \int_{-\infty}^{\infty} e^{i(k-k_f \sin \theta)x} dx dk. \end{aligned} \quad (2.42)$$

The last part of the expression in equation (2.42), the integral over x , is well known [42] to yield

$$\int_{-\infty}^{\infty} e^{i(k-k_f \sin \theta)x} dx = 2\pi \delta(k - k_f \sin \theta),$$

where $\delta(t)$ is the Dirac function. Using the well-known delta function property,

$$\int_{-\infty}^{\infty} F(k) \delta(k - k_0) dk = F(k_0),$$

the received voltage in wavenumber-frequency domain is given by

$$\begin{aligned} V_{\text{recv}}(k, \omega) &= -\frac{\omega \rho_f \gamma A_T A_R}{4\pi} \int_{-\infty}^{\infty} R(k, \omega) \frac{e^{ik(-d \sin \alpha - ib \sin \alpha - \tilde{x}') - i\sqrt{k_f^2-k^2}(\tilde{z}+\tilde{z}')}}{\sqrt{k_f^2-k^2}} 2\pi \delta(k - k_f \sin \theta) dk, \\ &= -\frac{1}{2} \omega \rho_f \gamma A_T A_R R(k_f \sin \theta, \omega) \frac{e^{ik_f \sin \theta(-d \sin \alpha - ib \sin \alpha - \tilde{x}') - ik_f \cos \theta(\tilde{z}+\tilde{z}')}}{k_f \cos \theta}. \end{aligned}$$

If the relations (2.35) are used explicitly, the received voltage can be written as

$$V_{\text{recv}}(k, \omega) = -\frac{1}{2} \omega \rho_f \gamma A_T A_R R(k_f \sin \theta, \omega) \mathcal{P} \mathcal{A}. \quad (2.43)$$

where the \mathcal{P} and \mathcal{A} contain, respectively, the phase and amplitude dependency of the signal, with their expressions given by

$$\begin{aligned}\mathcal{P} &= e^{-ik_f x' \sin \theta - ik_f (z+z') \cos \theta} e^{-ik_f d (\sin \theta \sin \alpha + \cos \theta \cos \alpha)} e^{-ik_f d' (\sin \theta \sin \alpha' + \cos \theta \cos \alpha')} \\ &= e^{-ik_f [x' \sin \theta + (z+z') \cos \theta + d \cos(\theta-\alpha) + d' \cos(\theta-\alpha')]} \\ \mathcal{A} &= \frac{e^{k_f b (\sin \theta \sin \alpha + \cos \theta \cos \alpha) + k_f b' (\sin \theta \sin \alpha' + \cos \theta \cos \alpha')}}{k_f \cos \theta} = \frac{e^{k_f [b \cos(\theta-\alpha) + b' \cos(\theta-\alpha')]} }{k_f \cos \theta}.\end{aligned}$$

Therefore, the absolute value of the received voltage, which is influenced only by the term \mathcal{A} , has the form

$$\begin{aligned}|V_{\text{rec}}(k, \omega)| &= \frac{1}{2} \omega \rho_f \gamma A_T A_R |R(k_f \sin \theta, \omega)| \frac{e^{k_f [b \cos(\theta-\alpha) + b' \cos(\theta-\alpha')]} }{k_f \cos \theta} \\ &= \frac{\omega \rho_f \gamma A_T A_R}{2 k_f \cos \theta} |R(k_f \sin \theta, \omega)| e^{k_f (b+b') - 2k_f \left[b \sin^2 \left(\frac{\theta-\alpha}{2} \right) + b' \sin^2 \left(\frac{\theta-\alpha'}{2} \right) \right]} \\ &\approx \frac{\omega \rho_f \gamma A_T A_R}{2 k_f \cos \theta} |R(k_f \sin \theta, \omega)| e^{k_f (b+b') - k_f \left[b \frac{(\theta-\alpha)^2}{2} + b' \frac{(\theta-\alpha')^2}{2} \right]}.\end{aligned}\tag{2.44}$$

The equations (2.43) and (2.44) show the influence of the extrinsic experimental parameters on the received voltage. From equation (2.43) it is clear that the vertical position of the transducers z and z' influence only the phase, term \mathcal{P} , and not the magnitude of the received voltage in the wavenumber-frequency domain. Both transmitter and receiver have a Gaussian beam profile, which is centered on the beam axis. The orientation of the beam is determined by the transducer's orientation angle α and α' , respectively. The beam width $\Delta\theta$ is determined by the Fresnel length b and b' , respectively, or by the beam waist W for a given medium and frequency $\Delta\theta = 1/\sqrt{2k_f b} = 1/k_f W$. Thus a larger angular beam spread can be achieved with a smaller Fresnel length. Equation (2.44) shows that the individual beam contributions of both transducers affect the (k, f) spectrum of the received voltage. If the transducers are identical, the parameters b and b' are equal. In this case, the optimal match between the transducers' beams is obtained for the same incident angle $\alpha = \alpha'$. The condition of having identical transducers with the same orientation is not essential for the model of the received voltage but is common

in practice. In this case, for identical transducers with the same orientation, the received voltage expression is simplified to

$$|V_{\text{recv}}(k, \omega)| \approx \frac{\omega \rho_f \gamma A_T A_R}{2k_f \cos \theta} |R(k_f \sin \theta, \omega)| e^{2k_f b - k_f b(\theta - \alpha)^2}, \quad (2.45)$$

which is similar to the expression of the received signal previously derived by Fei [35] in equation (3.13). If the receiver has an extremely small Fresnel length b (or the beam waist W , $b = k_f W^2/2$) such that it vanishes or if it is so small compared to the transmitter's Fresnel length that it can be neglected, the contribution of the receiver's directivity function to the voltage disappears. When a receiver has its aperture decreased to the size of a pinhole by an ultrasonic absorbent mask, its beam waist and Fresnel length are decreased also. Then the expression of the received voltage includes only the influence of the transmitter's Gaussian beam parameters

$$|V_{\text{recv}}(k, \omega)| \approx \frac{\omega \rho_f \gamma A_T A_R}{2k_f \cos \theta} |R(k_f \sin \theta, \omega)| e^{k_f b \left[1 - \frac{(\theta - \alpha)^2}{2}\right]}. \quad (2.46)$$

For the case when both transducers' Fresnel lengths vanish, we expect to have no beam influence in the received voltage expression; the only limitation is given by the transducers' bandwidth and the associated electronics.

$$|V_{\text{recv}}(k, \omega)| \approx \frac{\omega \rho_f \gamma A_T A_R}{2k_f \cos \theta} |R(k_f \sin \theta, \omega)|.$$

From the above formula we can conclude that it is possible to obtain the reflection coefficient from a single line scan if both transducers have a vanishing Fresnel length. In practice, even for a very small aperture size ($\sim \lambda/4$) the Fresnel length does not vanish, and its contribution therefore cannot be ignored. Thus, experimentally, the reflection or transmission coefficient can best be obtained as the ratio of the received voltages with and without the sample. The voltage received in a line scan measurement when there is no sample between the probes is called reference voltage V_{ref} and has the expression given by equation (2.44) with $R = 1$. Both scans need to be performed in the same

setup geometry in order that the only difference is the reflection/transmission coefficient contribution. Therefore, the reflection coefficient is given, according to the equation (3.15) derived by Fei [35], by

$$| R(k_f \sin \theta, \omega) | = \frac{| V_{\text{recv}}(k, \omega) |}{| V_{\text{ref}} |}. \quad (2.47)$$

The transducers' combined directivity function is contained in the reference voltage. In order to obtain individual directivity pattern of one of the transducers, the other has to be a point source/receiver. In practice, an aperture size less than half of the smallest wavelength is enough for a probe to be approximated as a point source/receiver with its directivity equal to unity in all spatial directions. For example, we shall consider a pair of identical air-coupled transducers such as those used in our experiment; the transmitter having an aperture radius of 5.0 mm and the receiver having its active area masked by an absorbent material, such as open-cell foam, with its aperture decreased to a radius equal to the smallest quarter wavelength in the probes' bandwidth. A typical bandwidth for the air-coupled transducers that were used in our experiments is 50 kHz to 1 MHz, in which the smallest wavelength is 0.343 mm given by a waveform traveling in air at the upper bound frequency 1 MHz. The pinhole mask produces an aperture radius approximatively 0.10–0.12 mm for the receiver. In this investigation the aperture was found to act as a quasi-point source/receiver from which sound diverges on the farther side uniformly in all directions. The product of the wavenumber and effective transducer's radius is then $ka=1.0991$; thus the angular part of the directivity function of this transducer has the shape of an ellipse with the values of major and minor axis so close that this ellipse can be approximated by a circle. If the pressure field of one transducer is sampled with such a point receiver along and across the acoustical beam's axis over the scan grid, its directivity pattern can be measured.

Results and discussion

The directivity patterns of planar and focused air-coupled transducers are predicted theoretically with CTP model and compared with experimental results. A comparison of the CTP and the conventional model shows that similar results are obtained for the received voltage and the pressure field. The CTP model is preferred over the conventional piston model because the latter typically requires integrations over the aperture of both transmitter and receiver, making the task of numerical computation complicated. The CTP model avoids these integrations by modeling the quasi-Gaussian transducers with point source/receiver translated into the complex plane. It should be emphasized that even though the pressure fields of a piston and a Gaussian transducer are different, the received voltage from a pair of piston and Gaussian probes respectively is nearly identical [62]. Furthermore, by using multiple complex transducer points placed along the acoustical axis rather than a single point, Fei and Chimenti [33] have shown that the CTP model reproduces all the features of a piston probe model.

The numerical evaluations of the CTP model for planar and focused transducers with the exact characteristics as the transducers used in experiment are presented in fig. 2.16 and 2.17. The transducers are a 10 mm diameter planar and a focused transducer with the focal length $F_0=26.5$ mm, both operating in air at 500kHz and 700kHz, respectively. The pressure profile is color-coded with the dark red color represents the highest amplitudes of the pressure and dark blue the lowest value. The acoustic field was generated for a grid of 500x500 points along (z -axis) and across (x -axis) the acoustical axis of the transducers. As we expected the beam spread is decreasing with the increase of the frequency as predicted by equation (2.32). Although the near field and the side lobes are not replicated by the CTP model, the far field and the general pattern of the pressure field are well represented and agree with the experimental measurements shown later in this section.

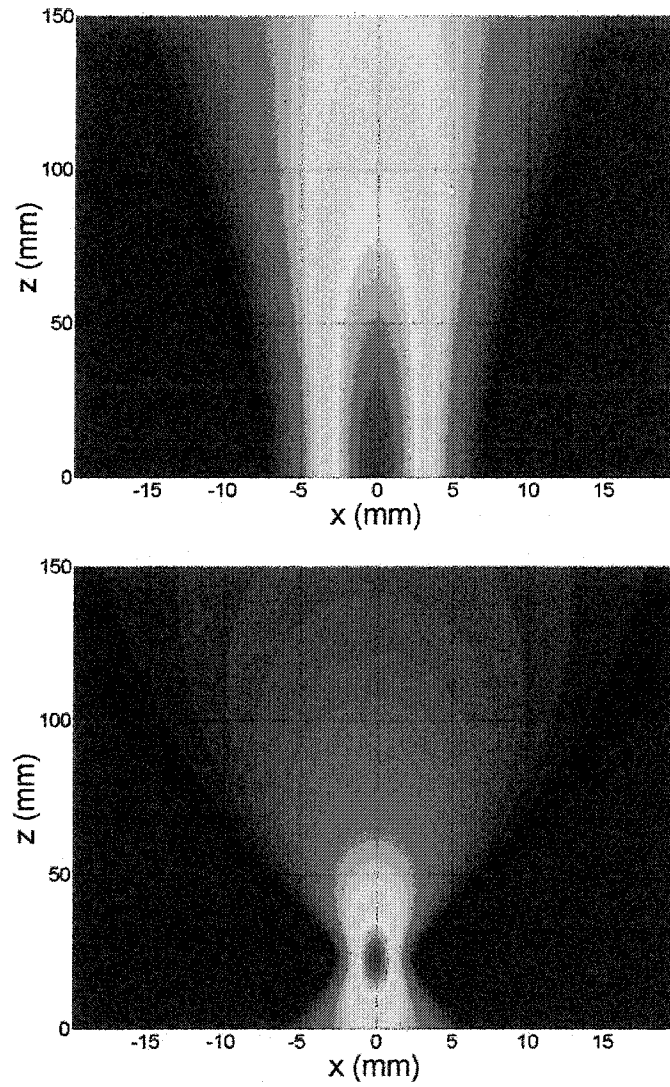


Figure 2.16 CTP Model. Pressure field of a 10 mm diameter planar (top) and focused (bottom) transducer at 500kHz. A Gaussian transducer is replaced with a complex point source to model its acoustic profile. The dark red color represents the highest amplitudes of the pressure and dark blue the lowest value.

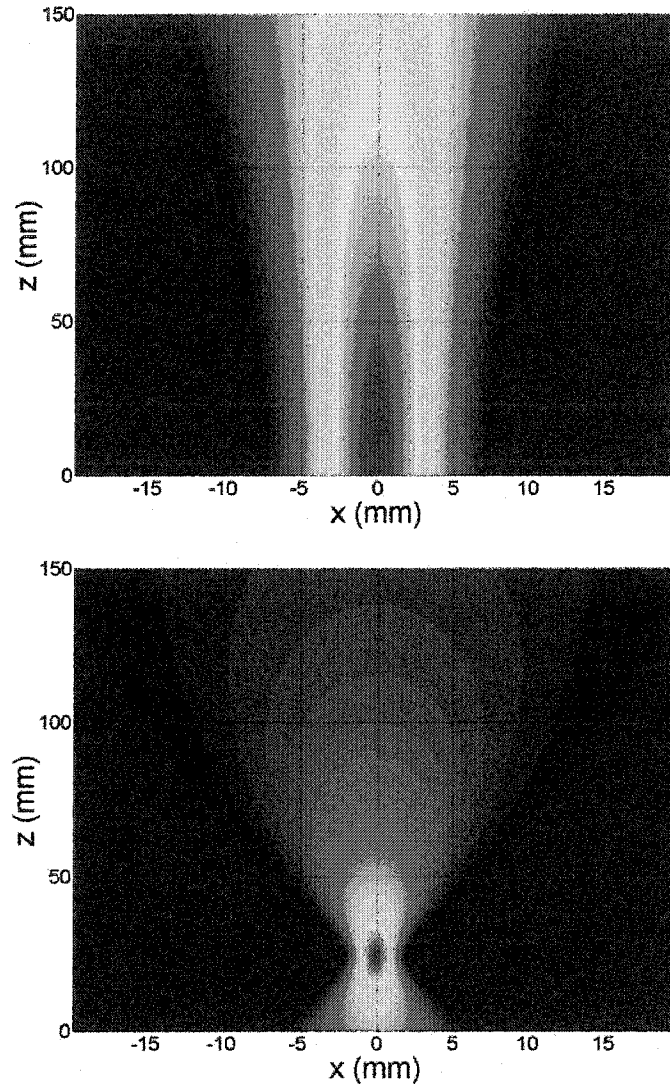


Figure 2.17 CTP Model. Pressure field of a 10 mm diameter planar (top) and focused (bottom) transducer at 700kHz. The focal length is $F_0=26.5$ mm. The numerical evaluation of the pressure field is performed over a grid of 500x500 equally spaced points in the range -20 mm to 20mm along the x -axis and 0 to 150 mm along the z -axis.

Experimental results for the directivity profile measurement

The directivity pattern of a planar capacitive transducer is measured at several distinct frequencies in the interval 0.4–1.0 MHz. The transmitter is excited with a five-cycles tone burst with an amplitude of 400 V_{pp}. The quasi-point receiver is fabricated by masking the aperture of a planar capacitive transducer with an open-cell foam disk, which presents a central 0.10-0.12 mm diameter pinhole. The acoustic field of the transmitter is then sampled in a line scan along the x -axis perpendicular to the transmitter's acoustic axis (z -direction). The length of the line scan is 80 mm, performed in 200 steps with a step size of 0.4 mm. In the z -direction, the separation distance between the transmitter and point receiver is changed from 20 mm to 152.4 mm (6 inch) in 24 steps of 6.35 mm (0.25 inch) each. The size of the scan grid is 80x132.4 mm with a cell of 0.4x6.35 mm. For each position in the scan grid, a waveform is recorded. From the spectrum of the waveform the fundamental frequency of the tone burst is then extracted and stored according to its grid position. The map of these frequency amplitudes over the scan grid produces the directivity pattern of the transmitter.

In figs. 2.18 and 2.19 is presented the pressure profile of the 5-mm radius planar capacitive foil transducer measured in air at 500kHz and 700kHz respectively. The initial separation distance between the transmitter and the quasi-point receiver is 20 mm. The amplitude of the pressure is normalized to its maximum value in the scan. The measured scan is oversampled to produce a smooth profile without changing its shape or features.

These experimental results are in good agreement with the CTP model predictions shown in fig. 2.16 and 2.17. To demonstrate the close agreement between the numerical predictions and the experiment, a comparison of the “cross-sectional” pressure field is shown in the top graph of fig. 2.20 for a planar transducer with a radius of $a=5$ mm operating in air at 700 kHz. Although the side-lobes of the field are not replicated by

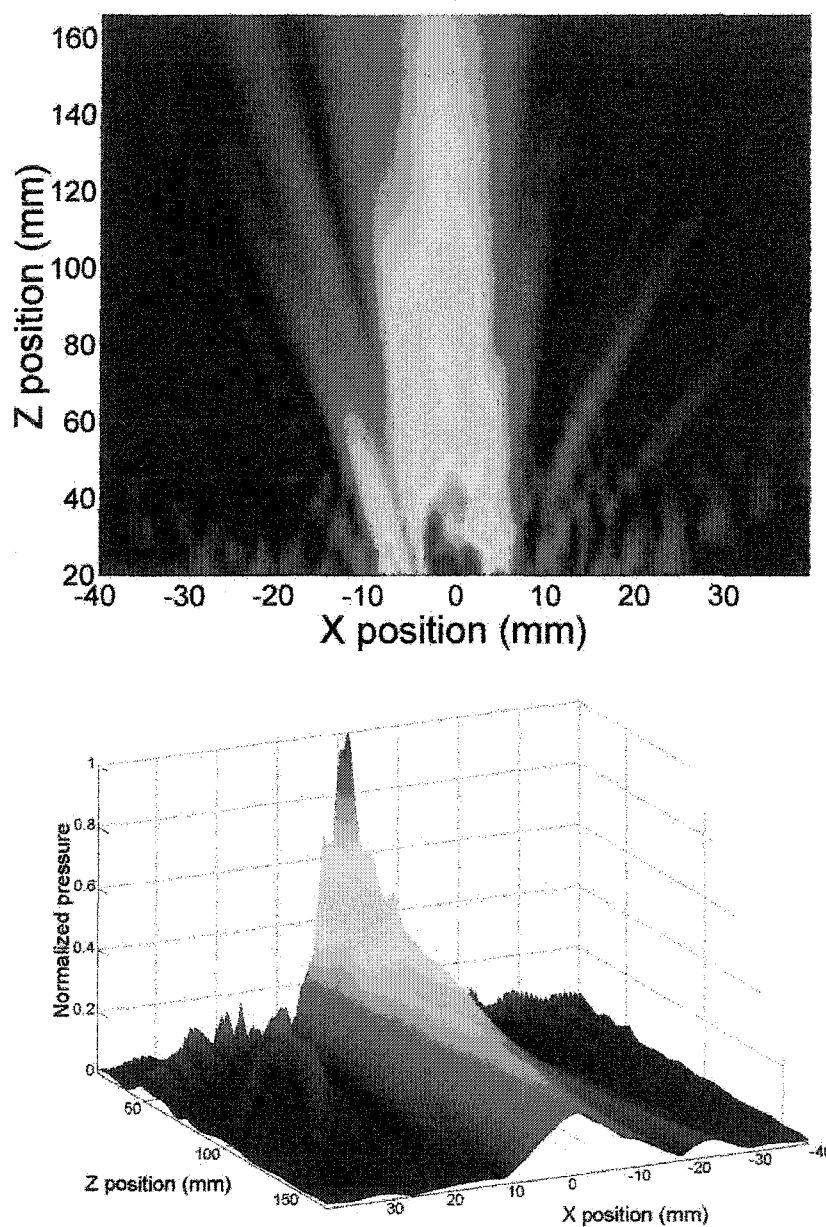


Figure 2.18 The measured directivity pressure profile (2D top image, 3D bottom graph) of the planar capacitive foil transducer with a radius of $a=5$ mm at 500 kHz

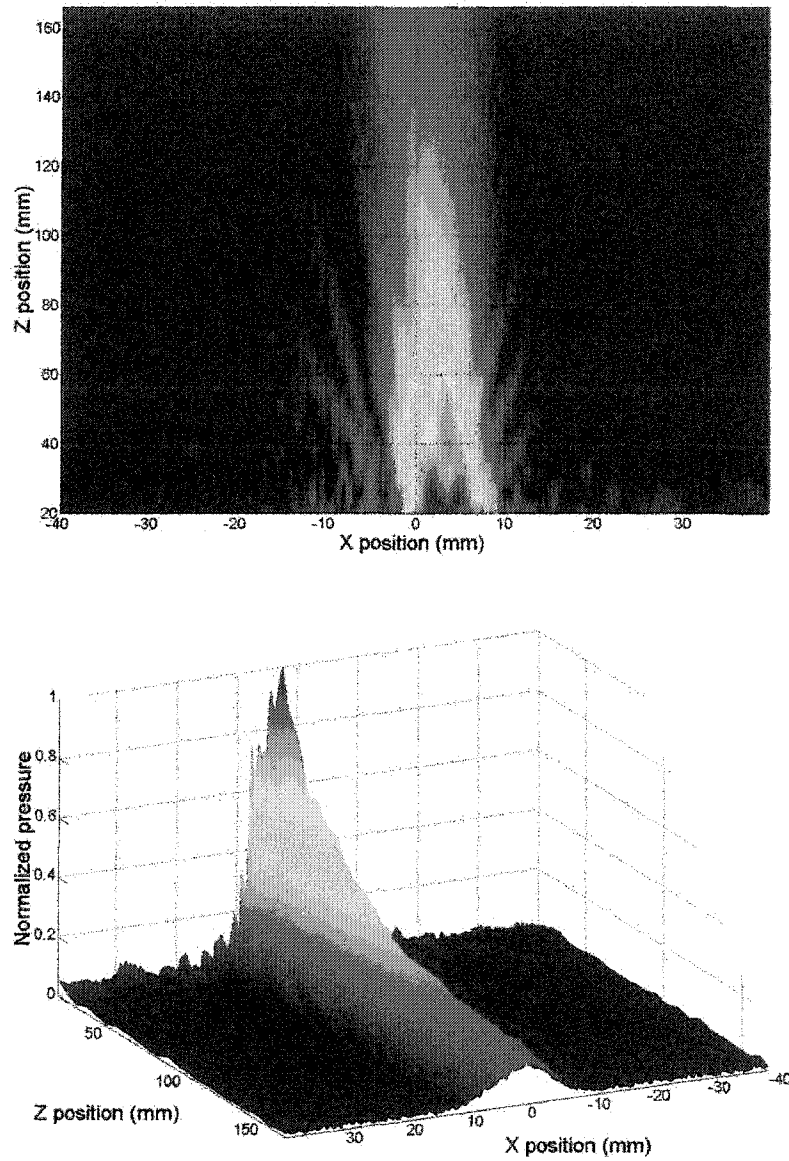


Figure 2.19 The measured directivity pressure profile (2D top image, 3D bottom graph) of the planar capacitive foil transducer with a radius of $a=5$ mm at 500 kHz

the CTP model, as we expected, the main lobe has the same general shape (Gaussian) in both cases: experiment and CTP model. However, the side lobes, of the measured field are in relatively good agreement (position and width) with the piston model prediction. Furthermore, the bottom graph in fig. 2.20 shows that the experimental pressure field along the acoustical axis of the transducer (black solid curve) is in close agreement with the model prediction (red dash curve). The small difference in the decay rate of the pressure field with the distance z is explain by considering the effect of attenuation of acoustic waves in air that is neglected in the model. In conclusion, the same general shape is observed, however, the side lobe pattern is not replicated by the single CTP model. The experimental results are presented without any enhancement. In all plots, a linear scale was used for the amplitude of the pressure field. For the 500 kHz frequency, the pressure field decays by 60% in 130 mm, while at 700 kHz the decay is 80%.

In fig. 2.21 and 2.22 is shown the pressure field of a focused probe (focusing acoustic mirror mounted on a planar capacitive foil transducer) measured in air for several distinct frequencies in the range 100–800 kHz. The scan grid is smaller than in the case of the planar probe, being concentrated on the vicinity of the focal plane. The scan is performed with 251 steps of 0.2 mm along the x -axis and 12 steps of 6.35 mm along the z -axis; the scan area is 50x76 mm centered on the acoustical axis of the transmitter.

The measured data is in good agreement with the CTP model. As we expected, the measured pressure profile shows little decay of its amplitude in the vicinity of the focal plane and its beam width is decreased with the increase in frequency.

In fig. 2.23, the experimental and predicted spectrum of the received voltage of the focused probe sampled in the focal plane are compared. The line scan is performed in the focal plane of the transmitter. For each discrete position along the x -axis a time dependent waveform is recorded. Through a 2D spatial and temporal FFT, the measured waveforms are transformed from (space-time) signals into (wavenumber-frequency) spectra. The predicted CTP spectrum is modified to compensate for the attenuation of

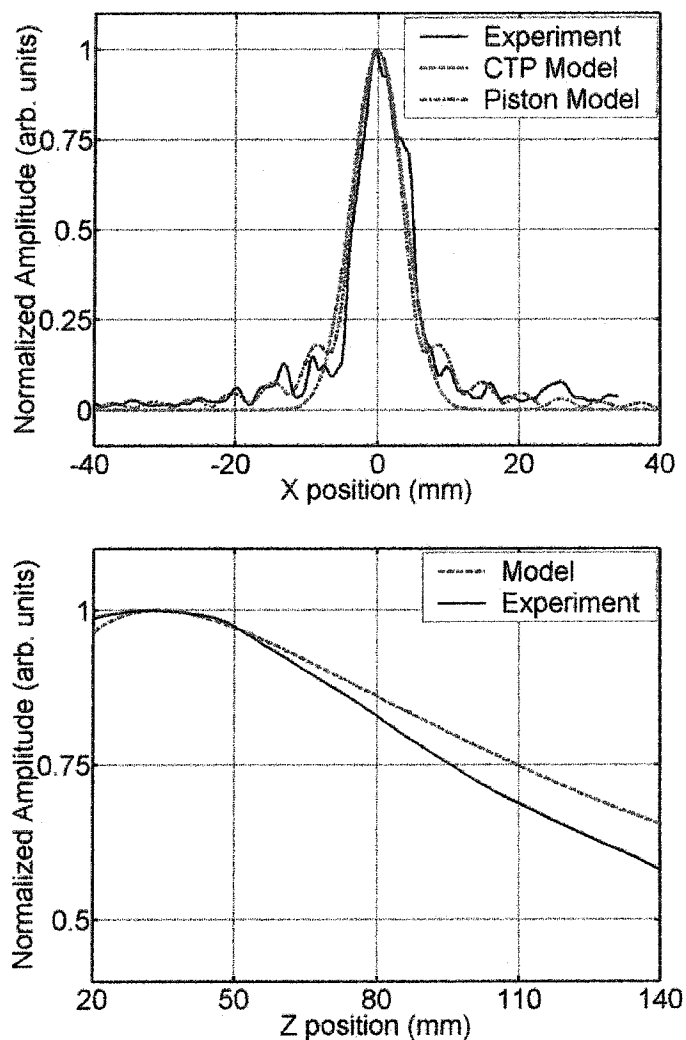


Figure 2.20 Comparison of the experimental acoustic profile with numerical prediction for a planar capacitive foil transducer with a radius of $a=5$ mm at 700 kHz. The “cross-sectional” pressure profile (top graph) is sampled at a distance $z = 20$ mm from the transducer. The measured acoustic pressure (black solid curve) is compared with CTP model (red dash line) and piston model (blue dash line). The bottom graph shows the experimental (black solid curve) and predicted (red dash line) pressure profile along the acoustical axis z .

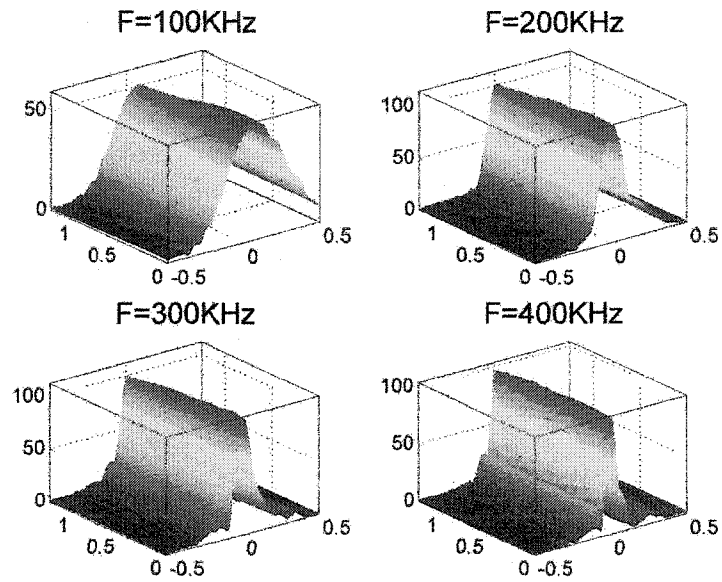


Figure 2.21 The experimental directivity pattern of the focused capacitive foil transducer measured in the frequency range 100-400 kHz close to the focal plane.

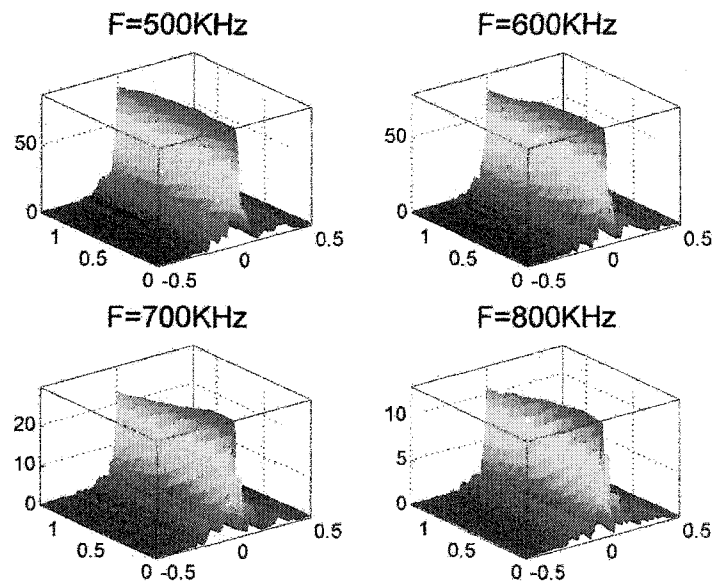


Figure 2.22 The experimental directivity pattern of the focused capacitive foil transducer measured in the frequency range 500-800 kHz close to the focal plane.

the ultrasonic waves in air that occurs with increases in frequency. The values of the amplitude in both spectra were normalized to their maxima. The amplitude is color coded, with dark blue representing the lowest value. Because the evaluation is done in a plane normal to the transmitter's acoustical axis, the CTP spectrum is symmetric with respect to $k = 0$. If only a temporal FFT is applied to the measured (space-time) voltage, the result is the spatial spectrum measured in the focal plane. In fig. 2.24 is presented the experimental (top) and predicted (bottom) spectrum of the received voltage of the focused capacitive foil transducer measured and evaluated in the focal plane of the transmitter. It can be seen that the CTP model shows good agreement with the experiment. The results shown in fig. 2.23 and 2.24 are obtained using equation (2.43) and the CTP model.

Conclusion

The characteristics of capacitive foil transducers have been studied both theoretically and experimentally. An acoustic mirror has been designed for producing focused ultrasonic beams in air and produced from CAD drawings by rapid prototyping.. A complete analytical received voltage model has been reviewed and explicit expressions have been derived for the pressure field and received voltage of both planar and focused probes. Extensive model calculations have been performed to investigate the predictions of the received voltage model and compare them with the results using conventional piston beams. The received voltage model predictions are compared with the experiment in this section and in the next chapter. An automated scan system has been developed for experimental verification of the model. The experimental results show generally good agreement with the received voltage model predictions. The capacitive foil transducers have been found to be adequate for air-coupled ultrasonic experiments.

Acknowledgments

This work was supported by the Center for Nondestructive Evaluation at Iowa State University. The author acknowledges the support of a graduate assistantship from the Institute for Physical Research and Technology at Iowa State University, and would like to thank Dr. Dong Fei for some helpful discussions on modeling and Dr. Stephen D. Holland for help in the experiments and signal processing.

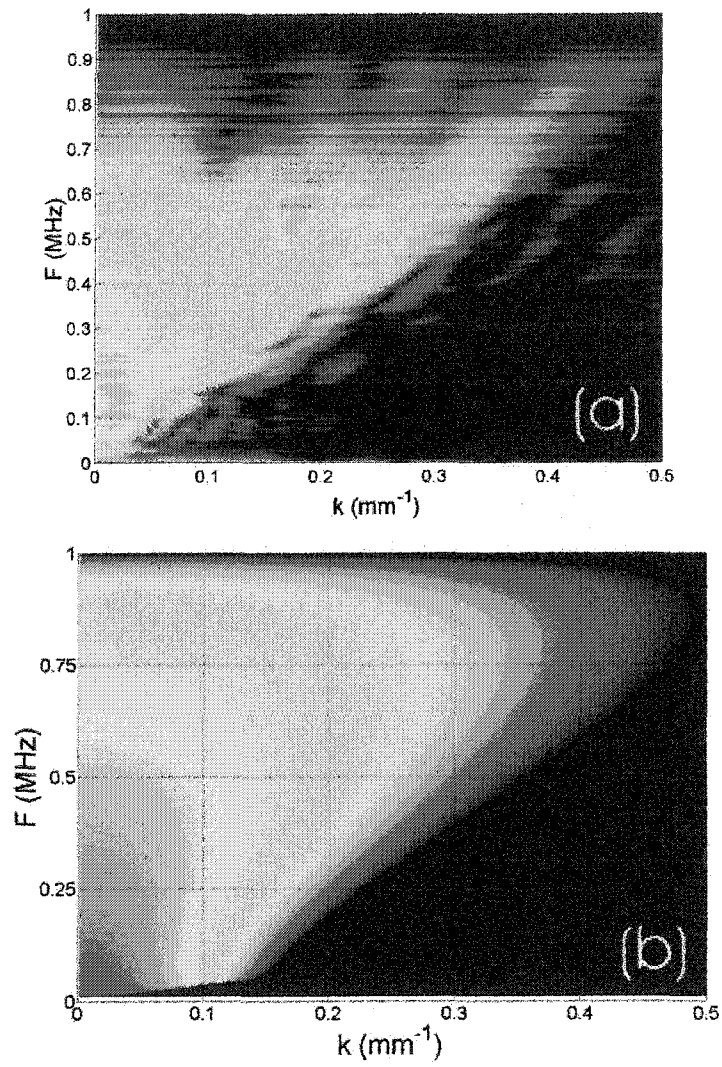


Figure 2.23 The measured (a) and predicted (b) spectrum of the received voltage of the focused capacitive foil transducer

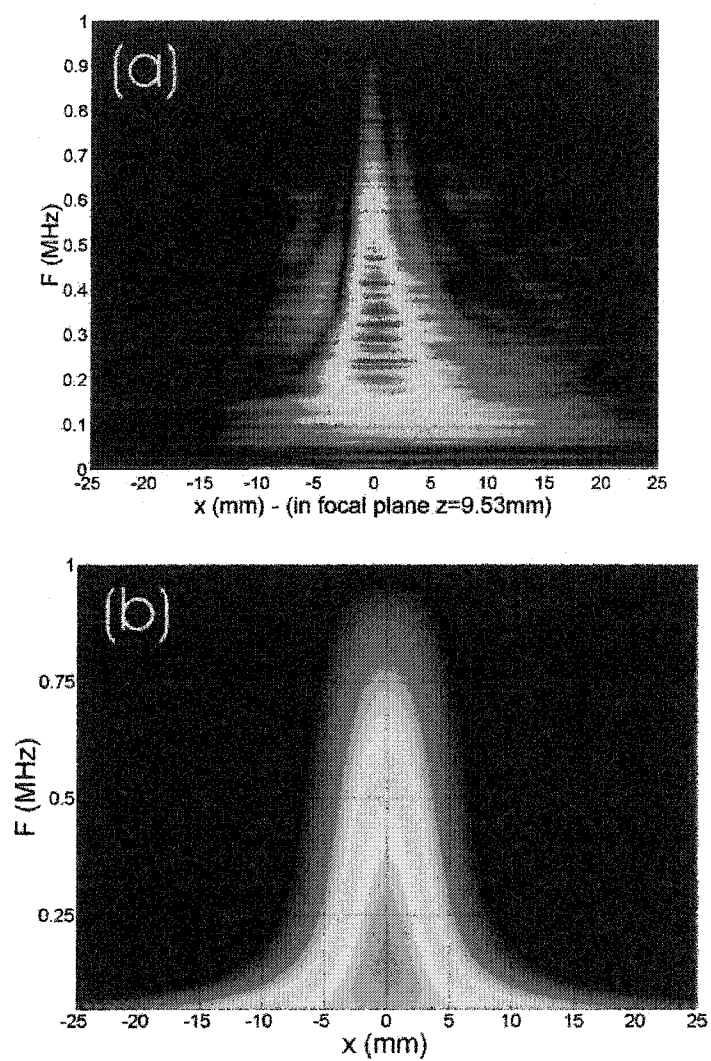


Figure 2.24 The measured (a) and predicted (b) spectrum of the received voltage of the focused capacitive foil transducer in the focal plane

CHAPTER 3 RECONSTRUCTION OF INFINITE PLATE DISPERSION SPECTRA BY USE OF FOCUSED AIR-COUPLED ULTRASOUND

Introduction and basic concepts

Although the application of guided waves to material characterization has been studied over the past 50 years, only in the past 15 to 20 years have technological advances made possible the quantitative evaluation of material properties. Interest in the study of guided waves arises from the fact that these acoustic excitations can provide valuable information about the mechanical properties of an elastic medium because of the waves' dependency on the material's viscoelastic stiffness. The demand for assurance of structural integrity, detection of environmental degradation and study of material aging can be met by a method that produces rapid and reliable estimation of elastic stiffness. Because of their potential and application in fields where safety is a constant concern, the focus of most of the studies has been composite materials. An extensive listing of the research done in this area of guided waves and their application to materials characterization can be found in the review article by Chimenti [19].

Materials characterization experiments have been performed traditionally in water immersion because of the good energy coupling and the wide availability of broadband, highly focused transducers. The development by Kuhl *et al.* [55] of a capacitive transducer and the application by Luukkala *et al.* [68] of non-contact probes to infer the

dispersion of guided wave modes in plates by identification of the transmission peaks as a function of incident angle can be considered the first steps of modern, quantitative air-coupled ultrasonics. Recent advances in the design and performance of air-coupled acoustic transducers have significantly improved the characterization of elastic material properties by ultrasonic measurements in air. Schindel *et al.* [90] and Hutchins *et al.* [50] developed an air-coupled, micromachined probe based on electrostatic transduction, leading to efficient broadband generation and detection of air-coupled ultrasound. Ladabaum and Khuri-Yakub [58] designed high frequency micromachined, air-coupled transducers with usable sensitivity as high as 11.4 MHz. Hosten and Castaings [48] adapted a parabolic mirror to a planar transmitter to generate a wide angular range in air and then used a chirp excitation to measure the phase velocity of Lamb modes. More recently, Robertson *et al.* [82] reported the design of a broadband focused capacitive foil transducer, and Gan *et al.* [39] applied pulse-compression techniques for air-coupled imaging.

Safaeinilli *et al.* [88], [89] introduced the synthetic aperture coordinate scanning technique, which smooths out the interference of the side lobes, and they developed an air-coupled method of estimating viscoelastic stiffness in plates, exploiting a detailed calculation to predict the measurable widths and relative heights of successive transmission maxima in air. Lobkis *et al.* [62] studied, theoretically and experimentally, the influence of the transducer beam and experimental geometry on the received voltage. Fei and Chimenti [31] and Fei *et al.* [32], [34] demonstrated a technique for rapid reconstruction of the transmission and reflection coefficients with a broadband, wide angular range synthetic aperture line scan performed in water immersion. A critical advance in accurate material property estimation was accomplished by Lobkis *et al.* [63], [64], in the separation of the extrinsic contributions of various geometric elements such as transducer size, location, and focal length from intrinsic material properties in the received voltage expression. Lobkis and Chimenti [65], [26] demonstrated the similarity of the received

voltage for a pair of planar piston and Gaussian transducers respectively, an important finding because it allows replacement of a pair of identical reciprocal piston transducers with a pair of Gaussian probes, with almost no loss of accuracy. This replacement simplifies significantly the numerical evaluation of the received voltage. Deschamps [30] introduced mathematical means of constructing Gaussian beams through the relocation of a real point source to a position in the complex plane. The field of this complex point source projected on the real axis is very close to the profile of a Gaussian beam. Zeroug *et al.* [99], [100] introduced a transducer model with both the transmitter and receiver replaced by complex source points and used the model to investigate the interaction of acoustic beams for various geometries of planar and cylindrical samples. Zhang *et al.* [101], [102] analyzed the effect of the inspection geometry on the measured signal and studied the differences between the two- and the three-dimensional case in the received voltage for an immersion reflection measurement.

The dispersion spectra of plate waves in the context of material elastic properties evaluation are highly redundant. Rokhlin and Chimenti [84] and Rogers [83] demonstrated that specific areas of the guided wave modes of a plate predominantly influence specific elastic stiffnesses, and Chimenti and Fei [23] and Fei *et al.* [32] validated the technique by producing rapid elastic stiffness reconstruction for reflection measurements performed with highly focused broadband water immersed probes in a single synthetic aperture coordinate scan. The reconstructed viscoelastic stiffnesses have been obtained from the measured received voltage, with an iterative inverse algorithm targeting specific portions of dispersion curves.

In the present study, we show that guided wave modes can be successfully reconstructed in an air-coupled transmission arrangement by exploiting the broad bandwidth and large angular range of our custom capacitive foil transducers [44], [45]. We implemented a new pulse compression technique, which increases the signal-to-noise ratio and produces excellent discrimination of the extrinsic contributions. The custom focused

probe is manufactured from a planar capacitive foil transducer onto which a stereolithographic parabolic mirror has been attached. The focused probe was designed to produce an approximate line focus beam with an angular range in air of approximately 16° . The focused acoustic beam and the large velocity difference between the air and the samples are exploited to produce the required wide angular range of the phase-match angles necessary for rapid reconstruction of the guided wave modes. We should emphasize that we have been able to reconstruct the complete guided waves spectra in the transducer operating bandwidth with only one transducer orientation angle and a single synthetic aperture coordinate scan. Even for water immersion tests, in which efficient energy coupling and high focusing can be easily employed, a complete reconstructed spectra is nearly impossible to achieve. A phase-match angle of almost 90° , required in some cases for the complete map of the guided wave modes, is impossible to obtain, in contrast to the situation with air-coupled tests, where this it is not necessary because of the large acoustic wavespeed difference between air and samples. Our goal is to demonstrate that by measuring the energy leakage at discrete locations along the sample with only one fixed orientation angle in the transmission setup, we can reconstruct all the essential guided wave modes simultaneously.

We implemented a digital signal processing technique, introduced by Holland and Sachse [43], that has been shown to filter out most of the destructive interference and noise sources from the received signal through a cross-correlation operation of the excitation with the received signal. Ideally, the result of the cross-correlation of these two signals is exactly the impulse response of the medium that exists between transmitter and detector. The auto-correlation of the excitation is a pulse-like function with a spectrum given by the bandwidth of the excitation. Therefore, the time domain excitation is transformed by this cross-correlation operation into a pulse-like time domain signal. In the experiments, the cross-correlated received signal has additional contributions, other than the impulse response of the sample, such as reflections from surrounding objects,

but a simple time-domain windowing process will extract only the data of interest (i.e., Rayleigh-Lamb energy leakage). A 2D-FFT transforms the measured impulse response waveforms into the k - f (wavenumber-frequency) spectra. The guided wave modes characteristic to the sample plate are observed as peaks in the amplitude of the received voltage spectra for the bandwidth and wavenumber range of the experiment. The bandwidth is specific to the air-coupled probes, but the k wavenumber range can be selected experimentally by selecting the step size of the synthetic aperture coordinate scan. Good agreement between theoretical and experimental results has been found for a wide range of materials.

Theory of the method

One physical quantity containing the material viscoelastic stiffness information accessible to investigation in an ultrasonic measurement is the transmission (TC)/reflection (RC) coefficient. The actual measured quantity is the received voltage, but this parameter has been shown [32] to be a windowed form of the (TC)/(RC). Even though the reflection measurements have the advantage of a single-sided access, the geometrical restriction on the path of a synthetic aperture coordinate scan and the large amplitude difference (80 – 100 dB) between the specular reflection signal and the leaky Lamb wave signal make this approach less desirable for an air-coupled experiment. In the case of the transmission geometry, the transducers can be easily aligned to small or large orientation angles, including normal incidence, making it possible to reconstruct all the guided mode cut-offs within the transducer frequency bandwidth. Furthermore, for an air-coupled experiment, the angular range of the phase-match angle for which all possible guide wave modes can be excited at once is less than 20° for most materials. Therefore, with a single synthetic aperture coordinate scan, all modes, including the mode cut-off frequencies, can be reconstructed at once. The importance of the mode cut-offs derive

from the simple relationship the mode cut-offs have with either the longitudinal or shear wave velocities in the thickness direction of the plate; hence the associated longitudinal and shear stiffness can be determined directly and simultaneously from the measured data [95].

Our approach in reconstruction of the guided wave modes in plates has been to measure the energy leakage in a transmission arrangement and to exploit the large angular range characteristics of both probes. The propagating guided wave modes are identifiable as peaks in the received voltage spectrum. A voltage model has been developed for comparison of the experimental results with the theoretical predictions.

Received Voltage Transducer Model

The received voltage of a pair of identical reciprocal focused piston transducers has been obtained with the received voltage transducer model. The model takes advantages of the fact that in the expression of the voltage, the combination of both transmitter and detector directivity functions can be replaced by those of two Gaussian beams with little loss of accuracy. Therefore, even though the acoustic field of each individual transducer is far from being a Gaussian beam, we can treat their combined contribution in the formula of the received voltage as though they were Gaussian transducers. This fact by itself simplifies significantly the numerical evaluation of the voltage, but in addition, it is particularly important because it allows us to simplify the model even further. The pressure field of a finite Gaussian probe is well approximated by the projection onto the real axis of the field produced by a complex point source. Therefore, a pair of two identical reciprocal finite Gaussian transducers can be replaced with a pair of complex source and receiver points. The received voltage transducer model uses these results to model finite reciprocal piston probes, with the complex point source and receiver in the expression of the received voltage.

If we consider the location of the center of the transducer aperture to be $\mathbf{r} = (x, y, z)$,

the transformation $\mathbf{r} \rightarrow \tilde{\mathbf{r}} = \mathbf{r} + \mathbf{d} + i\mathbf{b}$ will translate the location into the complex plane. The vector $\tilde{\mathbf{r}} = (\tilde{x}, \tilde{y}, \tilde{z})$ specifies the new location of the complex point source. The vector \mathbf{d} controls the transducer Gaussian beam position relative to the center of the aperture, and \mathbf{b} determines the Fresnel length and beam direction. Both \mathbf{d} and \mathbf{b} have the same direction, which is the beam propagation direction. The Fresnel length or the magnitude of \mathbf{b} is given by $b = k_f W^2/2$, with W the $1/e$ beam width at the waist location and k_f the fluid wavenumber ($k_f = \omega/c_f$, c_f velocity of sound in fluid, $\omega = 2\pi f$ the circular frequency, f frequency). Thompson and Lopes [94] indicated that the beam width at the waist location and the distance between the waist location and the center of the aperture d have the following expressions:

$$W = W_0 \frac{\beta}{(1 + \beta^2)^{1/2}} \quad \text{and} \quad d = \frac{F_0}{(1 + \beta^2)}, \quad (3.1)$$

where $\beta = 2F_0/(k_f W_0^2)$, F_0 is the focal length and W_0 is the beam width at the transducer aperture. The estimation of W_0 used in the literature is $W_0 = 0.757a$ [94], [62], [32] with a the radius of the transducer. Fig. 3.1 presents the geometry used in the experiment and in the theoretical prediction of the model. The focused probes are shown in the transmission setup. The separation distance between their acoustical axes along the plate is x_i . During the synthetic aperture line scan, one probe's position with respect to the plate is kept constant while the other probe is moved in the x-direction in equally spaced steps along the sample.

For the geometry shown in fig. 3.1, we replace both transmitter and detector with the complex transducer points in order to obtain a simplified expression of the received voltage. The spatial coordinates of the point transducers are written as

$$\begin{aligned} \tilde{x}' &= x' - d' \sin \alpha' - ib' \sin \alpha', \quad \tilde{y}' = y', \quad \tilde{z}' = z' - d' \cos \alpha' - ib' \cos \alpha' \\ \tilde{x} &= x + d \sin \alpha + ib \sin \alpha, \quad \tilde{y} = y, \quad \tilde{z} = z + d \cos \alpha + ib \cos \alpha. \end{aligned} \quad (3.2)$$

Using Auld's reciprocity theorem [7] and the spectral decomposition of the spherical waves, the received voltage $V(x, f)$ is obtained for a specific frequency f and discrete

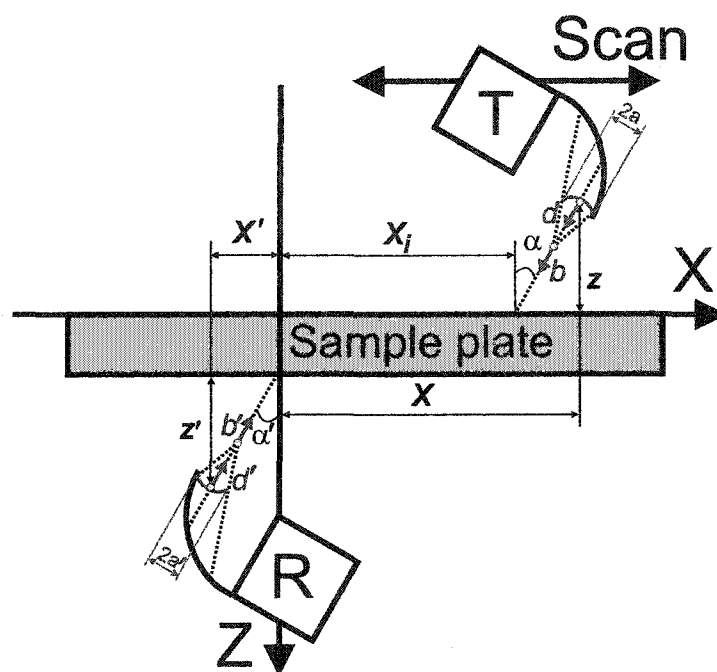


Figure 3.1 Received voltage transducer model geometry. The same setup has been used for both experimental measurements and theoretical calculations. The system of planar capacitive foil transducer and parabolic acoustic mirror has been replaced in the numerical evaluation with the equivalent focused probe.

receiving position x as

$$V(x, f) = -\frac{1}{8\pi^2} \gamma(\omega) \omega \rho_f \int_{-\infty}^{\infty} \int_{-\infty}^{\infty} T(k_x, k_y, f) e^{ik_x(\tilde{x}-\tilde{x}') + ik_y(\tilde{y}-\tilde{y}') + ik_z(\tilde{z}-\tilde{z}')} \frac{dk_x dk_y}{k_z}, \quad (3.3)$$

where $T(k_x, k_y, f)$ is the plane waves transmission coefficient. For an infinitely long line focus along the y -axis, we can consider the beams to be two-dimensional, located in the (x, z) plane. Therefore, any y -dependence of the parameters of the equation (3.3) can be neglected, simplifying the voltage expression to

$$V(x, f) = -\frac{1}{4\pi} \gamma(\omega) \omega \rho_f \int_{-\infty}^{\infty} T(k_x, f) e^{ik_x(\tilde{x}-\tilde{x}') + ik_z(\tilde{z}-\tilde{z}')} \frac{dk_x}{k_z}, \quad (3.4)$$

where $\gamma(\omega)$ contains the frequency response of probes and associated electronics, ρ_f is the density of the coupling fluid ($\rho_f = 1.2 \text{ kg/m}^3$ for air at room temperature [92]), $T(k_x, f)$ is the plane-wave transmission coefficient for the plate, and k_x and $k_z = \sqrt{k_f^2 - k_x^2}$ are the projections of the wavenumber on the x - and z -axes.

When a Fourier transform is applied to the equation (3.4) and the expression of the complex coordinates, equation (3.2), is substituted, the spectrum of the received voltage is obtained in the (k, f) domain as

$$V(k, f) = \int_{-\infty}^{\infty} V(x, f) e^{-ikx} dx \quad (3.5)$$

$$V(k, f) = \frac{-\gamma(\omega) \omega \rho_f}{4\pi} \int_{-\infty}^{\infty} T(k_x, f) \frac{\exp\{-ik_x(d \sin \alpha + ib \sin \alpha - \tilde{x}') + ik_z(\tilde{z} - \tilde{z}')\}}{k_z} \times \left(\int_{-\infty}^{\infty} e^{i(k_x - k)x} dx \right) dk_x. \quad (3.6)$$

The notation k is used in the equations (3.5) and (3.6) for an arbitrary value of wavenumber projection on the x -axis for which the voltage is calculated, whereas the notation k_x is still the wavenumber projection on the x -axis allowed to take any value in the interval $(-\infty, +\infty)$ as variable of integration. The last integral with respect to variable x is the unweighted Dirac's delta function $2\pi\delta(k_x - k)$. Therefore the expression for $V(k, f)$ can be simplified to

$$V(k, f) = \frac{1}{2} \gamma(\omega) \omega \rho_f T(k, f) \frac{\exp\{-ik(d \sin \alpha + ib \sin \alpha - \tilde{x}') + ik_z(\tilde{z} - \tilde{z}')\}}{k_z}. \quad (3.7)$$

If the wavenumber k is replaced with $k = k_f \sin(\theta)$, with $\theta = \arcsin(k/k_f)$, the phase-match angle that corresponds to a particular incident plane wave from the angular spectral decomposition, the exponent can be further simplified to

$$| e^{-ik(d \sin \alpha + ib \sin \alpha - \tilde{x}') + ik_z(\tilde{z} - \tilde{z}')} | = \exp -2k_f(b \cos(\theta - \alpha) + b' \cos(\theta - \alpha')). \quad (3.8)$$

Furthermore, using the approximation $\cos(\theta - \alpha) = 1 - 2 \sin^2((\theta - \alpha)/2) \approx 1 - 2((\theta - \alpha)/2)^2$ [42] the exponential is simplified to

$$| e^{i(-k(d \sin \alpha + ib \sin \alpha - \tilde{x}') + ik_z(\tilde{z} - \tilde{z}'))} | \approx e^{-k_f(b+b')} e^{-k_f b(\theta - \alpha)^2} e^{-k_f b'(\theta - \alpha')^2}. \quad (3.9)$$

The normalization of the absolute value of the received voltage with the factor $e^{-k_f(b+b')}$ is critical in the numerical evaluation of the voltage, as shown by Fei et al. [32], to be frequency invariant

$$| V(k, f) | = \frac{1}{2} \gamma(\omega) \omega \rho_f | T(k, f) | \frac{e^{-k_f b(\theta - \alpha)^2} e^{-k_f b'(\theta - \alpha')^2}}{k_f \cos \theta}. \quad (3.10)$$

For identical reciprocal transducers having the same radius, focal length and incident angle $a = a'$, $b = b'$ and $\alpha = \alpha'$, the received voltage expression is further simplified to

$$| V(k, f) | \approx \frac{1}{2} \gamma(\omega) \omega \rho_f | T(k, f) | \frac{e^{-2k_f b(\theta - \alpha)^2}}{k_f \cos \theta}. \quad (3.11)$$

The latter expression shows that the relative position of the transducer with respect to the sample plate has an influence only on the phase of the voltage and not on the amplitude. The angular range of the received voltage can be written in the form $\Delta\theta = (1/\sqrt{2k_f b}) = 1/(k_f W)$ and is determined by the transducer Fresnel length b or the waist beam width W . Furthermore, $\Delta\theta$ can be explicitly written as a function of the geometrical transducer parameters

$$\Delta\theta = \frac{W_0}{2F_0} \sqrt{1 + \left(\frac{2F_0}{k_f W_0^2} \right)^2} \approx \frac{0.376a}{F_0} \sqrt{1 + \left(\frac{3.5367F_0}{k_f a^2} \right)^2}. \quad (3.12)$$

For high frequency, the square root can be approximated as unity, leading to

$$\Delta\theta \approx \frac{0.376a}{F_0}, \quad f \gg \frac{1.745F_0 v_f}{\pi a^2}. \quad (3.13)$$

For example, in the case of a 10 mm diameter transducer with a focal length of 26.5 mm operating in air ($v_f = 340$ m/s) at frequencies higher than 200 kHz, the angular range $\Delta\theta$ is independent of frequency.

The influence of the extrinsic geometrical parameters on the received voltage is shown in equation (3.11) to be present only as a window function, restricting the access to the transmission coefficient spectrum to the frequency bandwidth of the probes. This is the reason why we employ focused broadband probes for the reconstruction of the guided wave modes. The angular range is significantly larger for the directivity function of a focused probe than for that of a planar probe, resulting in a wider window function and therefore better access to the spectrum of the transmission coefficient.

The received voltage transducer model has been exploited to produce a numerical evaluation of the signal for several samples that were also measured experimentally. In fig. 3.2 is shown the theoretical prediction of the spectrum of the received voltage for an aluminum 6061 plate with a thickness of 6.68 mm (0.263 inch). The numerical evaluation has been performed for 500 equally spaced steps in the frequency bandwidth 0.01–1 MHz and wavenumber range 0–0.3 mm⁻¹. The maxima of the transmission coefficient are shown in red, while the dark blue represents the lowest value for the voltage amplitude. The top x - and right y -axis show the phase-match angle in air for the given spatial and frequency bandwidth. Because the maximum angle for which the energy can be coupled into the sample in air is 7.8°, all the guided wave modes can be reconstructed at once with our focused probe. The solid and dotted curves represent the dispersive guided wave modes obtained for the same sample in vacuum. The maxima in the transmission coefficient correspond to propagating guided waves, and the close agreement with dispersive curves shows that air has little influence on the dispersive spectrum, because its density is so small compared to the solid.

Fig. 3.3 presents the numerical evaluation of the received signal for a 5.5 mm (0.215 inch) Plexiglas plate performed in 500 equally spaced steps in the frequency range 0.01

- 0.7 MHz and wavenumber range 0 - 0.4 mm⁻¹. In the case of Plexiglas, the second critical angle is close to 17°, but with the choice of a 7° orientation angle for both the transmitter and the receiver, it is shown to be possible to reconstruct all the essential guided wave modes with a 16° focused probe. A consistent result has been observed experimentally for Plexiglas.

The evaluation of our voltage model performed for a uniaxial glass-epoxy composite (SE84LV/EGL/300/400/37%, supplied by S P Systems) is presented in fig. 3.4 for a scan along the fibers and in fig. 3.5 across the fibers. The spatial and frequency bandwidths for the theoretical prediction have been chosen to be in the range 0 - 0.5 mm⁻¹ and 0.01 - 1 MHz respectively, with 500 by 500 equally spaced steps. Several modes as A_0 , S_0 , A_1 , S_1 , A_2 , S_2 from the bottom to the top of the spectrum are reconstructed in each case, with the cut-off frequency clearly defined. The spectrum presented in fig. 3.4 shows that most of the propagating energy is concentrated in the S_0 and S_1 symmetric modes while for the spectrum presented in fig. 3.5 the energy is more equally distributed for the symmetric as well as the antisymmetric modes. The phase-match angle in air is plotted in degrees on the top x- and right y-axis.

We also tested our method on two moderately anisotropic wood samples: a basswood plate of 6.350 mm (0.25 inch) thickness and balsa wood plate of 9.525 mm (0.375 inch) thickness. In both samples, the wood grain are orientated in the plane of incidence. The theoretical values of stiffness that have been used in the numerical evaluation of the received voltage and the dispersion spectrum come from the United States Forest Service and were published in the 1999 Wood Handbook [37]. These values represent average elastic material properties and are given with a $\pm 15\%$ confidence range. Fig. 3.6 and fig. 3.7 show the numerical evaluation of the received voltage for a bass and a balsa wood plate, respectively. The voltage spectra are evaluated in the 0.01–0.5 MHz frequency bandwidth to correspond with the experimental results; at frequencies above 0.5 MHz, it has been difficult to detect a transmitted signal through the wood samples. The values

of the elastic stiffness of the materials that have been used in the numerical evaluation of the received voltage are presented in table (3.1).

Transmission coefficient reconstruction

The measured received voltage is obtained in (x, t) space-time domain as time and position dependent waveforms, which have been recorded in a synthetic aperture coordinate scan for discrete positions along the surface of the plate. A 2D-FFT performed on the measured data transforms spatial-temporal waveforms into (k, f) , the wavenumber-frequency spectrum. This operation is important because, as the model shows in the equation (3.11), the intrinsic and extrinsic components can be clearly identified in the spectrum. The pulse-compression technique is employed to boost the signal-to-noise ratio. The remaining signal after the time windowing is the impulse response (transmission coefficient) of the inspected medium. The (k, f) spectrum of the received cross-correlated signal is precisely the transmission coefficient subject to the bandwidth limitation of the excitation and transducers. If the excitation signal in (k, f) domain is given by

$$V_{exc}(k, f) \approx \frac{1}{2}\gamma(\omega)\omega\rho_f \frac{e^{-2k_fb(\theta-\alpha)^2}}{k_f\cos(\theta)}, \quad (3.14)$$

where the phase is not shown, but still is considered in calculations, the received voltage will be given by equation (3.11). The cross-correlation of the excitation voltage $V_{exc}(x, -t)$ with the received voltage $V(x, t)$ will be transformed into the product

$$V_{cor}(k, f) = V(k, f)V_{exc}(k, f) \quad (3.15)$$

with the expanded expression

$$|V_{cor}(k, f)| \approx \left(\frac{1}{2}\gamma(\omega)\omega\rho_f\right)^2 |T(k, f)| \left(\frac{1}{k_f\cos(\theta)}\right)^2. \quad (3.16)$$

Therefore, the result of the cross-correlation of the excitation and measured signal transformed into the (k, f) spectra is obtained as $|V_{cor}(k, f)| \sim const |T(k, f)|$.

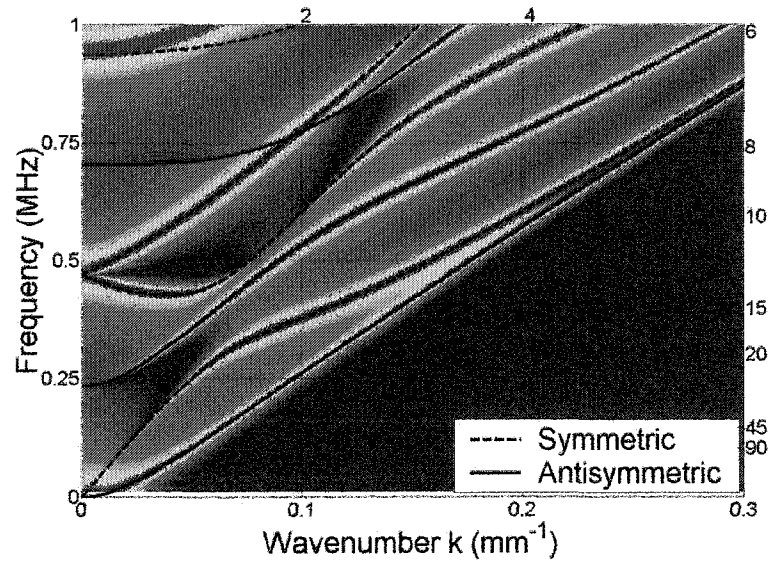


Figure 3.2 Numerical evaluation of the received voltage in air for an aluminum 6061 plate of thickness 6.68 mm (0.263 inch)

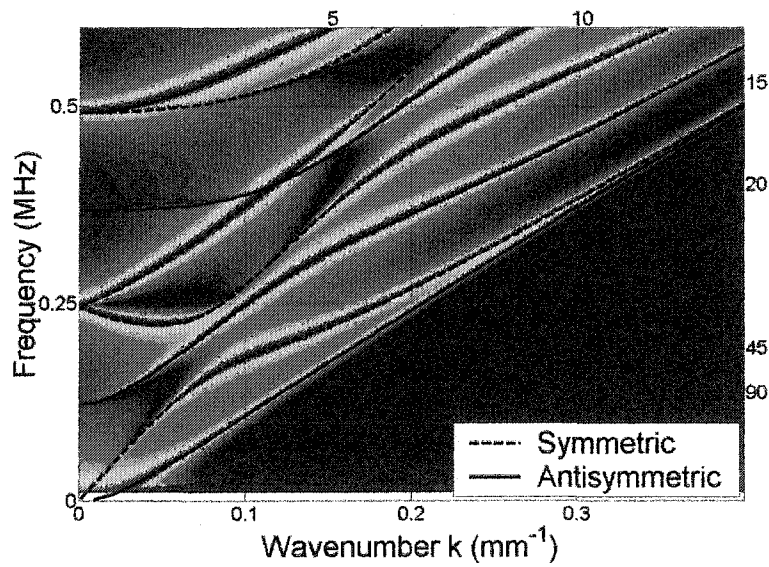


Figure 3.3 Numerical evaluation of the received voltage in air for a Plexiglas plate of thickness 5.5 mm (0.215 inch)

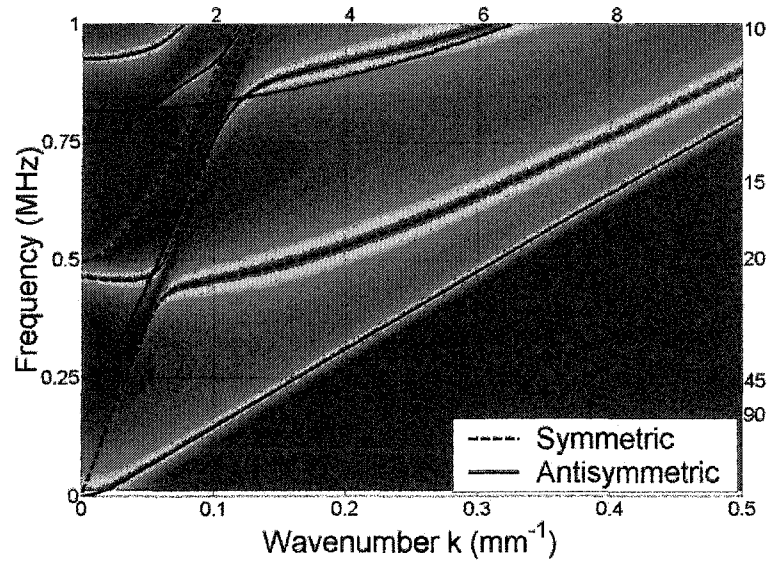


Figure 3.4 Numerical evaluation of the received voltage for a 20-ply uniaxial glass-epoxy composite. The scan is performed along the fiber direction.

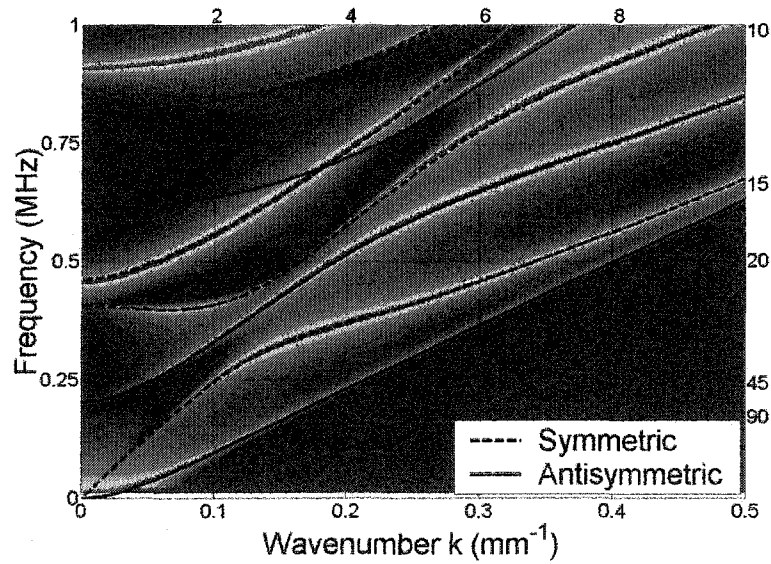


Figure 3.5 Numerical evaluation of the received voltage for a 20-ply uniaxial glass-epoxy composite. The scan is performed across the fiber direction.

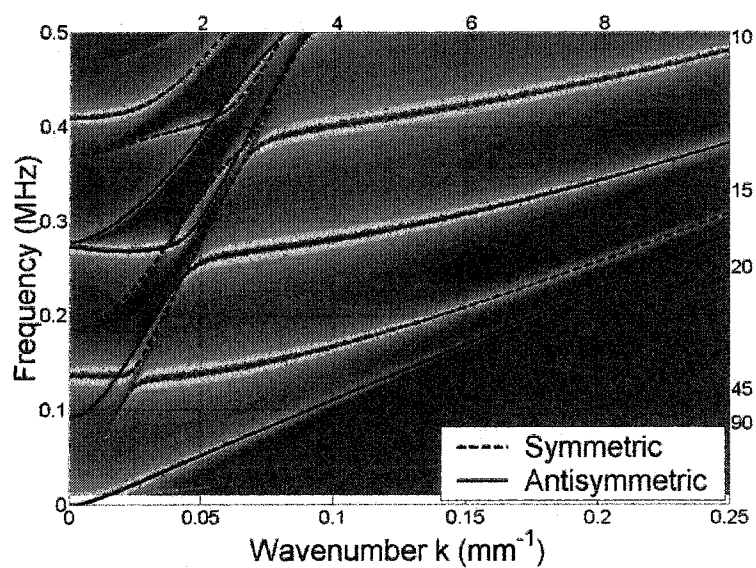


Figure 3.6 Numerical evaluation of the received voltage for a basswood plate with the thickness of 6.350 mm (0.25 inch). The wood grain is in the plane of incidence.

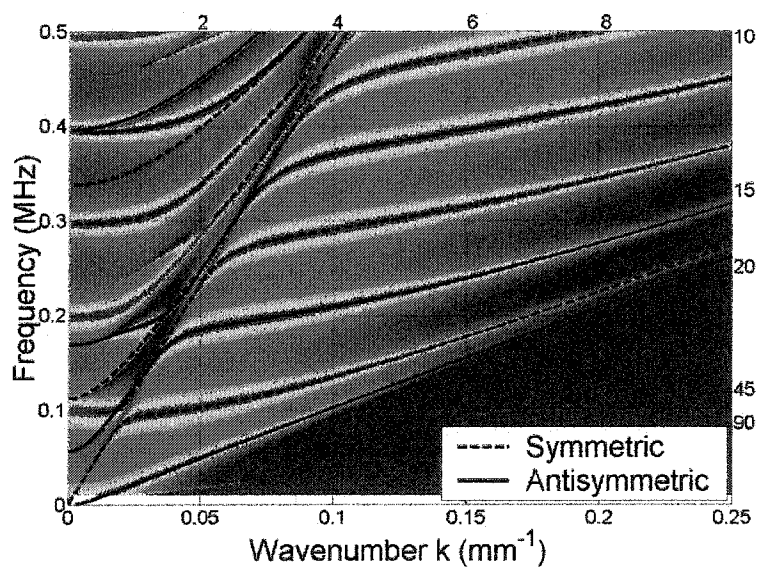


Figure 3.7 Numerical evaluation of the received voltage for a balsa wood plate with the thickness of 9.525 mm (0.375 inch). The wood grain is in the plane of incidence.

Table 3.1 Values of the elastic stiffness of some common materials

Material	Stiffness (GPa)								
	C_{11}	C_{12}	C_{13}	C_{22}	C_{23}	C_{33}	C_{44}	C_{55}	C_{66}
Aluminum 6061 ^a $\rho = 2.70 \text{ g/cm}^3$	107.50	54.59	54.59	107.50	54.59	107.50	26.45	26.45	26.45
Aluminum 2024 ^b $\rho = 2.70 \text{ g/cm}^3$	109.56	55.63	55.63	109.56	55.63	109.56	26.96	26.96	26.96
Plexiglas ^c $\rho = 1.19 \text{ g/cm}^3$	8.62	4.32	4.32	8.62	4.32	8.62	2.15	2.15	2.15
Unidirectional Aramid-epoxy ^d $\rho = 1.60 \text{ g/cm}^3$	8.64	5.31	5.31	8.64	5.31	8.64	1.76	1.76	1.76
Unidirectional Glass-epoxy ^e SE84LV/EGL $\rho = 1.50 \text{ g/cm}^3$	86.60	9.00	6.40	13.50	6.80	14.00	2.72	4.06	4.70
Basswood ^f $\rho = 0.37 \text{ g/cm}^3$	11.43	0.33	0.55	0.45	0.41	1.11	0.62	0.51	0.11
Balsa ^g $\rho = 0.16 \text{ g/cm}^3$	3.60	0.28	0.31	0.19	0.19	3.60	0.13	0.18	0.002

^aA. R. Selfridge *Approximative material properties in isotropic materials* IEEE Trans. on Sonics and Ultrasonics, SU-32, No. 3, 381-395, (1985).

^bA. Safaeinili, O. I. Lobkis and D. E. Chimenti *Quantitative materials characterization using air-coupled leaky Lamb waves* Ultrasonics, 34, 393-396, (1996).

^cA. R. Selfridge [93]

^dSafaeinili et al. [89]

^eSE84LV/EGL/300/400/37% supplied by S P Systems [5]

^fUnited States Forest Service, Wood Handbook (1999) [37]

^gUnited States Forest Service, Wood Handbook (1999) [37]

Focused probe parameters

In the air-coupled experiment, the relatively large difference in wavespeed between air and most engineering materials constitutes an advantage. For example, the second critical angle in air is $\approx 7.8^\circ$ for aluminum and $\approx 18^\circ$ for Plexiglas, the latter value being close to the second critical angle of a large range of composite materials. If the orientation angle of the transducers are chosen such that the acoustic beam spread lies in the range of normal incidence up to the second critical angle, the incoming acoustic energy can be coupled efficiently into the sample. Therefore, with a relatively low focused beam, most if not all of the essential guided wave modes can be excited at the same time. For the reason just referred to, Fei and Chimenti [31] showed that it is critical to have both the transmitter and receiver focused.

To achieve the required angular range, a parabolic acoustic mirror has been designed. A detailed description of the focused probe can be found in the previous chapter. The acoustic mirror/planar transducer system has similar characteristics as a cylindrically focused probe with a diameter of 10 mm and a focal length of 26.5 mm in air.

Experimental procedure

The experimental arrangement used to obtain all air-coupled measurements has been a transmission pitch-catch setup, in which one of the probes and the plate have been held fixed while the other probe sampled the energy leakage along a linear path parallel to the plate surface. Both the transmitter and the receiver have been kept in the same plane during the scan for all the experiments. The symmetry of the setup geometry with respect to the transducers' acoustical axes plane reduces the problem to two dimensions. The problem is therefore simplified to the plane (x, z) , where x is the scanning direction parallel to the plate and z is the axis perpendicular on the plate defining the separation between probes and sample. A synthetic aperture coordinate scan is performed along

The data acquisition system has been developed for optimal sensitivity, flexibility, and robustness, given the specific requirements of air-coupled experiments. This system has been designed to generate high amplitude arbitrary waveforms and to support high-speed data acquisition and processing. The diagram of the setup of the air-coupled ultrasonic experiment is presented in fig. 3.8.

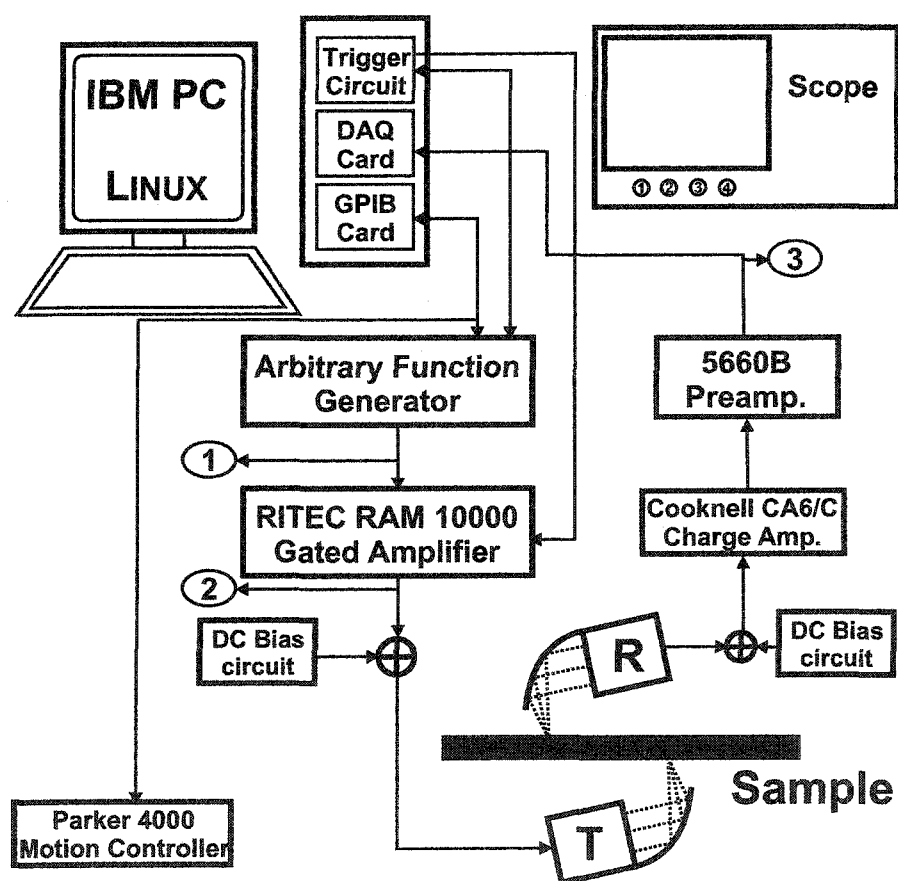


Figure 3.8 Experimental setup for air-coupled ultrasonic measurements

The experimental apparatus is completely computer-controlled through a GPIB data bus and an additional custom-built trigger circuit. Data acquisition is performed with an internal DAQ card PCI-DAS4020-12 that provides 10 MSamples/s on four 12-bit channels as well as digital I/O lines and two 12-bit DACs. This card acts as a fully functional oscilloscope with custom signal processing capabilities. The trigger circuit manages both the start and end of the RF amplifier gates and the speed of the measurement process. GPIB data bus is utilized for motion control, upload of the waveforms from the PC's memory to the arbitrary function generator, and control of the parameters of the gated amplifier and the arbitrary function generator. An arbitrary function generator HP/Agilent 33120 generates the custom excitation waveforms, which have been uploaded from the computer memory. A high-power, gated amplifier RITEC RAM 10000 is used to amplify the excitation to the energy level required by an air-coupled experiment. Transient signals from the gate triggers are suppressed by dithering of the beginning and end of the amplifier's rectangular window and by averaging of the received signals. The low-noise, two-dimensional position system Parker MC4000 has a step resolution of 0.01 mm. The transducers are capacitive foil probes with a cylindrical focus produced by the attached parabolic mirror, as described earlier.

The measurement process is controlled by the computer through the trigger of the start and end of the gate amplifier ramp and by the trigger rate of the measurement. The arbitrary waveform is generated in the computer memory by the DAQ program and then uploaded into the arbitrary function generator's flash memory. The system removes the constraints of using a classic tone-burst excitation signal and makes possible the use of any custom-generated waveform. This feature is advantageous because it allows the investigator to use synthetically generated waveforms to customize experiments.

The synthesized waveform is fed to the input of the RITEC RAM 10000 gate amplifier and brought to an amplitude level appropriate for air measurements [90]. The output signal of the RAM 10000 is applied over a DC bias circuit to the terminals of the

transmitter. The bias is required by the capacitive foil transducer to function; therefore, the transmitter and the receiver each has its own bias circuit. The receiver output is connected through a charge amplifier to its own DC bias circuit. The reception of an ultrasonic wave in air at the membrane will vary the capacitance of the foil dielectric, producing a dynamically varying charge in electrodes. Compared with piezoelectric transducers, capacitive foil transducers provide better sensitivity owing to the dramatically lower acoustic impedance mismatch between air and the detector's membrane. From the electrical standpoint, the electrostatic transducer can be described as a variable capacitor owing to the changes in distance between electrodes. These variations of the electrodes' separations can be understood as the influence of the arriving mechanical waves on the thin dielectric film that now acts from the mechanical standpoint, as a vibrating membrane. These characteristics of capacitive foil transducers explain that the various membrane resonances couple directly into the probe output and are affected by the membrane tension controlled by the bias voltage, whereas the air pocket resonances must drive the membrane first. Both phenomena are highly influenced by the membrane mass. Therefore, the transmitter has a thicker dielectric film ($10.0 - 12.5 \mu\text{m}$) than the detector, in which the film is about $2.5 - 5.0 \mu\text{m}$ thick, with an aluminum metallic layer of $100 - 500 \text{ \AA}$ (Mylar and Kepton films were supplied by Sheldahl Inc., MN). An aluminum layer is preferred over the gold layer because of aluminum's lower specific gravity.

After the arriving ultrasonic wave produces a variation of charge in the detector, this variation is translated into voltage through a charge amplifier Cooknell CA6/C and further amplified by a low-noise preamplifier Panametrics 5660B. The received voltage is acquired by the PCI-DAS4020-12 card and processed in real time in the computer's memory.

The conventional tone-burst excitation would be inadequate if it were to be used here, because the bandwidth and energy requirements cannot be fulfilled simultaneously. The

necessary bandwidth would translate to a one- or two-cycle burst, which would not couple enough energy into the air or sample. A longer tone-burst is too narrow-band to excite even a relatively small number of guided wave modes. Pulse excitations, although they have significantly larger bandwidth, have the transient signal energy concentrated in a short period of time. This characteristic makes pulse excitation inadequate for use with air-coupled capacitive foil transducers that require high energy excitations but have amplitude and duration restrictions on the transient voltages. Thus, in our experiment, the excitation signals, which are subject to amplitude and duration restrictions, must have broad bandwidth and carry high energy. The amplitude constraint is due to the dielectric breakdown, the mechanical and electrical limitation of the metal film and backplate. The duration of an excitation is limited by the duty cycle of the gated amplifier to approximately $200\ \mu\text{s}$. The excitation signal is custom designed to fulfill the requirements of broad bandwidth and high energy injected into the medium throughout the allotted time period. The signal found to provide the best results was a computer-generated random phase noise, which has been designed to have a bandwidth of 50 kHz–1 MHz and a length of 170–180 μs with a cosine ramp window [79]. In fig. 3.9, a typical random phase noise excitation (i.e., spectrum, phase, and time domain waveform) signal is presented. The absolute value of the signal is designed to have a broad bandwidth and is combined with the randomly generated phase to produce the complex spectrum of the excitation. An inverse FFT transforms the complex spectrum into time domain waveform as presented in the third graph of fig. 3.9.

Data acquisition and processing

A serious drawback of any air-coupled measurement is the inherent low signal-to-noise ratio that makes difficult the extraction of the useful information from the measured signal. To improve the signal-to-noise ratio of the measurements, a pulse-compression technique, introduced by Holland and Sachse [43], and associated with high-speed data

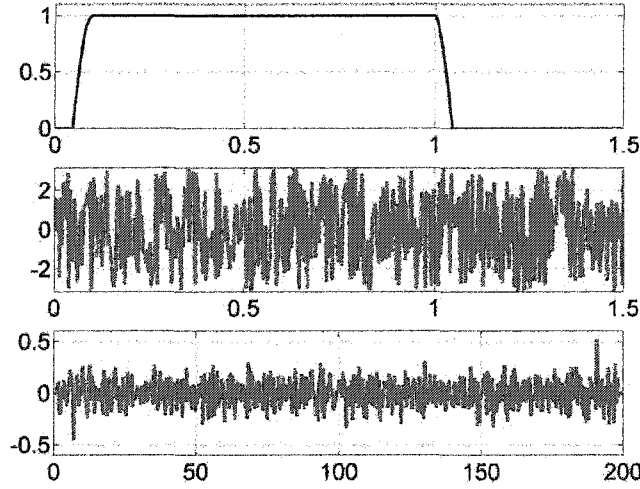


Figure 3.9 Random phase noise excitation: first two graphs represent the absolute value and phase of the signal spectrum (bandwidth 50 kHz–1 MHz), third is the actual time domain signal with a length of 200 μ s.

acquisition and real time processing has been adapted to this experiment. The synthetic aperture coordinate scan technique, introduced by Safaeinili *et al.* [88], [89], has been used to reconstruct the plane-wave transmission coefficient in air-coupled experiments.

The measurement process is controlled by an PC running Linux. The acquisition and real-time processing software run as a server application, allowing flexible control over the network. The random-phase noise signal is customized on the PC and loaded via an IEEE-488 interface into the arbitrary function generator memory. For the rest of the measurement, this signal is used as the excitation. The output of the function generator is further amplified by RITEC RAM 10000 to 200–250 V_{pp} for a Mylar foil with 12.5 μ m thickness and -225 V DC bias. After traveling through the medium, the ultrasonic

signal arrives at the receiver membrane and is converted by the capacitive foil transducer into a varying charge. The detector has a 2.5- μm Mylar film and 100 V DC bias. A charge amplifier Cooknell CA6/C transforms and amplifies the charge into voltage that is further amplified from 40 or 60 dB by a low-noise preamplifier Panametrics 5660B. The received voltage is then acquired by the acquisition card in the computer and recorded for either real time or post processing.

At any given moment of the measurement process, the following waveforms are stored in the computer's memory: the initial arbitrary waveform, the output of the arbitrary waveform generator, the output of the gated amplifier and the received signal corresponding to a specific location along the plate. We denote the broadband excitation signal (random phase noise) by $s(t)$. This signal $s(t)$ is stored and monitored at the output of each component before being applied to the transmitter. The impulse response of the system $h(t)$ is assumed to be linear and time invariant. The received signal $r(t)$ must then be given by [79]

$$r(t) = s(t) \otimes h(t), \quad (3.17)$$

where ' \otimes ' defines the convolution operator. The goal is to find the impulse response $h(t)$ of the measured medium. By performing the cross-correlation of the excitation signal $s(t)$ with the received signal $r(t)$, we can prove that the result is precisely the impulse response of the inspected medium restricted to the bandwidth of the excitation $s(t)$.

The measured signal $r(t)$ is cross-correlated with the excitation signal $s(t)$ and the result is similar to that obtained by performing the convolution of $r(t)$ and $s(-t)$. Therefore, we can write

$$r(t) \otimes s(-t) = (s(t) \otimes h(t)) \otimes s(-t). \quad (3.18)$$

Rearranging the right side of the equation (commute and reassociate), we obtain

$$r(t) \otimes s(-t) = (s(t) \otimes s(-t)) \otimes h(t). \quad (3.19)$$

The result of $s(t) \otimes s(-t)$ is a zero phase signal (equivalent to $S(f) \cdot \overline{S(f)}$ in the frequency domain). Because $s(t) \otimes s(-t)$ is a broadband signal with zero phase, it can be modeled as an impulse $\delta(t)$ in the time domain. Therefore the correlation between the received and excitation signals will be given by

$$r(t) \otimes s(-t) = \delta(t) \otimes h(t) = h(t) \quad (3.20)$$

for the bandwidth of $s(t)$ [79].

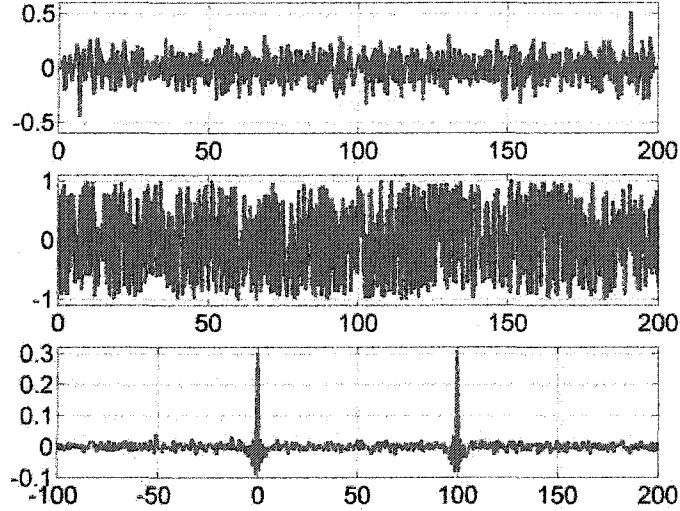


Figure 3.10 Typical results for impulse response $h(t)$ measurements with the pulse-compression technique. From the top: random phase noise excitation, received signal, impulse response of the medium.

An example of the data processing method is illustrated in fig. 3.10. The top graph shows the excitation $s(t)$, a typical random-phase noise signal with a bandwidth of approximately 1 MHz and a length of 200 μs . To model the received voltage, $r(t)$,

the following signals have been summed: the excitation $s(t)$, the $100\ \mu\text{s}$ delayed excitation ($s(t + 100\ \mu\text{s})$), and a random generated white noise. The first term in the simulated received voltage corresponds to the electro-magnetic interference in the detector, whereas the second term represents the response obtained from the excitation propagating through the inspected medium. The peak-to-peak amplitude of the white noise signal has been chosen to have a value ten times higher than the excitation $s(t)$ to illustrate an air-coupled ultrasonic measurement in which the signals are buried in the noise. The received voltage has been simulated to correspond to 100 trigger events. A different white noise signal has been randomly generated for each event. The bottom graph in fig. 3.10 shows the average of the cross-correlation of the received signal $r(t)$ and the excitation $s(t)$. The number of averages, 100, corresponds to the number of trigger events. A good signal-to-noise ratio is observed in fig. 3.10, just as with the actual experiment. The first peak, a quasi-pulse signal, is located at $t = 0\ \text{s}$ and corresponds to the initial excitation detected as electro-magnetic interference in the receiver. The second peak, related to the delayed excitation $s(t + 100\ \mu\text{s})$, is located at $t = 100\ \mu\text{s}$ and simulates the impulse response $h(t)$ of the inspected medium. The $h(t)$ signal contains the transmission coefficient information, which is used in the reconstruction of the dispersion curves.

The statistical analysis of a time series typically answers to questions about the randomness of the data, the presence of underlying trends, cyclic or seasonal effects, uncertainty of typical value and reasonable predictions of future observations. A commonly used test for checking the randomness in a data set is the autocorrelation plot [15]. The randomness is ascertained by computing autocorrelations for data values at varying time lags. If data is random we expect the autocorrelations to take values near zero for all time lag-separations otherwise for one or more autocorrelations that are significantly non-zero or show identifiable trends the data is considered non-random. The autocorrelation plot is a graphical technique but it has been exploited in a test proposed

by Ljung and Box [61] to produce a quantitative test for randomness. The Ljung-Box test also referred to as “portmanteau” test is based on the autocorrelation plot, but instead of testing randomness at each distinct lag, it tests the “overall” randomness based on a number of lags.

The typical assumptions for a data set tested for randomness are: the data points are equally-spaced, there are no missing values in the set and the number of samples is large. All of these assumptions are true for the random-phase data set that is the object of our analysis presented in the second graph of fig. 3.9. Furthermore the data set is stationary and ergodic being invariant time invariant and having its time and ensemble averaging equivalent. In other words a single-time recording of the process contains all possible statistical variations of the process, no additional information can be gained by observing this ensemble of sample signals over the information obtained from one recording of the signal.

To analyze the random-phase signal for randomness we employed the United States National Institute of Standards and Technology *Dataplot* statistical software [71]. Two tests have been performed on the random-phase data set: first being the qualitative autocorrelation plot shown in fig. 3.11 and second the quantitative Ljung-Box test with the result presented in table. 3.2.

The conclusions that can be drawn from this plot (fig. 3.11) are: first that with the exception of lag 0, which is always 1 by definition, almost all of the autocorrelations fall within the 95% confidence limits, and second there is no apparent pattern in the values of the autocorrelations. This absence of a pattern such as monotonic increase or decrease or cyclic change of sign, being an indication we expect to see if the data are in fact random. One lag outside the 95% and few others slightly at the border of 99% confidence limits do not necessarily indicate non-randomness. We might expect about one out of twenty lags to be statistically significant due to random fluctuations. As a technical note, the confidence interval is simply the proportion of samples expected to

be contained in that interval centered on the ensemble mean value. Furthermore the result of Ljung-Box test applied to the random-phase data set and presented in table. 3.2 proves that in fact the data is random.

The geometric arrangement of the experiment is presented in fig. 3.12, where the transmitter and receiver are shown with the parabolic acoustic mirror in place, in a transmission setting. One of the transducers is held fixed during the synthetic aperture coordinate scan, while the other is sampling the acoustic field leakage along the plate. The positions of both transducers have been kept in the same plane (x, z) , plane of incidence, at all times during the measurement. The x -direction is pointing along the plate while the z -direction is perpendicular to the sample. Because the transducers are cylindrically focused with their focal line along the y -axis, the y -dependence is neglected, and the problem is reduced to one of two-dimensions. The receiver voltage is recorded as a time-dependent signal for discrete coordinate positions on the line scan along the plate (x -direction). This synthetic aperture coordinate scan technique has been introduced by Safaeinili *et al.* [88], [89], and has been used by Zhang [104] and Fei [35] to reconstruct the plane-wave transmission/reflection coefficient in water- and air-coupled experiments.

The spatial scan step Δx size defines the maximum value of the wavenumber k accessible for inspection; Δx is much less than the smallest wavelength of the guided wave modes of interest. The value of the step size of the line scan Δx was chosen in the range $0.1 \text{ mm} \leq \Delta x \leq 0.3 \text{ mm}$. The total number of steps in the x -direction varies from 50 to 300 steps, depending on the elastic properties of the material. The received voltage is digitized into 10000 points of data at a sampling frequency of 10 MHz, with $0.01 \text{ } \mu\text{s}/\text{div}$ and is averaged depending on the material from 100 to 6000 times. The time window in which the RF signal is acquired and the spatial scan range Δx are set to be large enough to record all the receiver output signals of significant amplitude. The received signals outside of the time and spatial ranges of the scan are typically smaller than 2% of the largest signal amplitude in a scan and are therefore ignored.

Table 3.2 Output of the Ljung-Box randomness test performed on the random-phase signal with *Dataplot* statistical software

Ljung-Box test for randomness		
1. Statistics		
Number of observations	186	
Lag tested	45	
Lag 1 Autocorrelation	-0.5584814E-01	
Lag 2 Autocorrelation	0.2670012	
Lag 3 Autocorrelation	-0.9577191E-01	
Ljung-Box test statistic	44.42097	
2. Percent points of the reference chi-square distribution for Ljung-Box test statistic (reject hypothesis of randomness if test statistic value is greater than percent point value)		
0	% point	0.000000
50	% point	44.33512
75	% point	50.98495
90	% point	57.50530
95	% point	61.65623
99	% point	69.95683
3. Conclusion (at the 5% level) THE DATA ARE RANDOM.		

For each position in the synthetic aperture coordinate scan, the signal is digitized and recorded. The received voltage is cross-correlated with the excitation signal and the result averaged for a number of trigger events. An example of data processing with the pulse-compression method previously explained is shown in fig. 3.13. The waveforms shown in different colors in fig. 3.13 are recorded at seven evenly spaced locations. The electro-magnetic interference in the receiver is observed at $t = 0$ s, while the leakage of the Rayleigh-Lamb waves can be seen in the range $200 - 500 \mu\text{s}$. The signals detected later than $500 \mu\text{s}$ are reflections of acoustic waves from surrounding objects. To extract the part of the signal related only to the tested sample, a time window for the interval $200 - 500 \mu\text{s}$ is applied. A 2D-FFT transforms the temporal-spatial signals into the wavenumber-frequency spectra. The peaks in the spectra are maxima of the transmission coefficient and correspond to the guided wave modes in the sample.

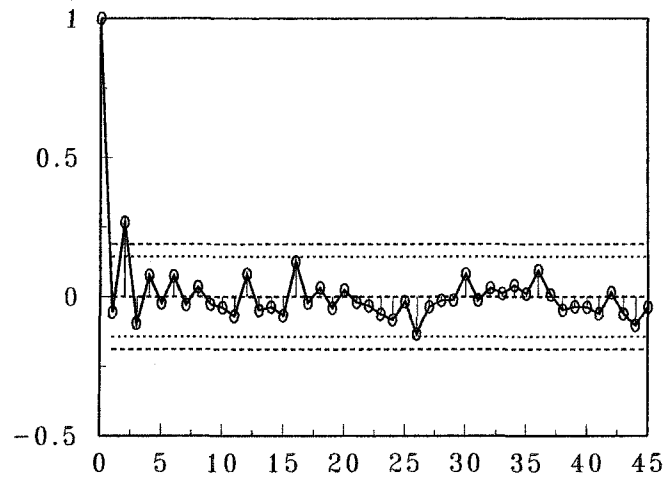
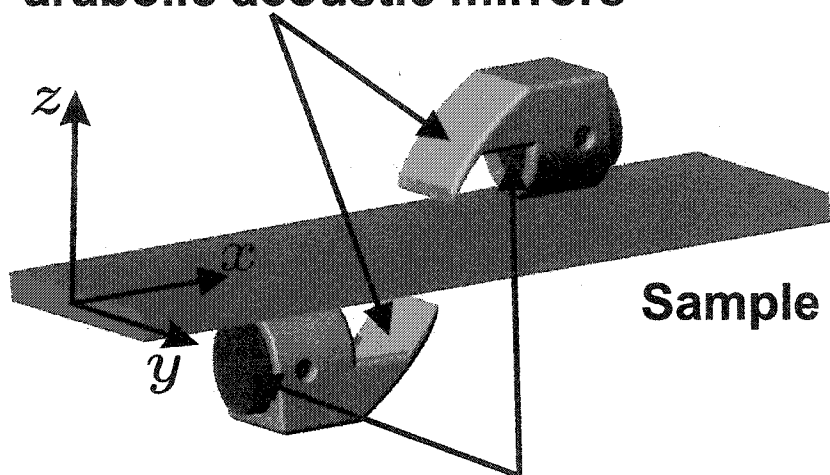


Figure 3.11 Statistical analysis of the random-phase signal: Autocorrelation plot. The x -axis represents the numbers of lags performed and the y -axis the values of the autocorrelation. The dotted curves is the 99% confidence interval while the dashed curve is the 95% confidence interval.

Parabolic acoustic mirrors



Capacitive foil transducers

Figure 3.12 Air-coupled experimental geometry. The parabolic acoustic mirrors are built with a stereolithographic process (rapid prototyping) directly from a SolidWorks CAD model.

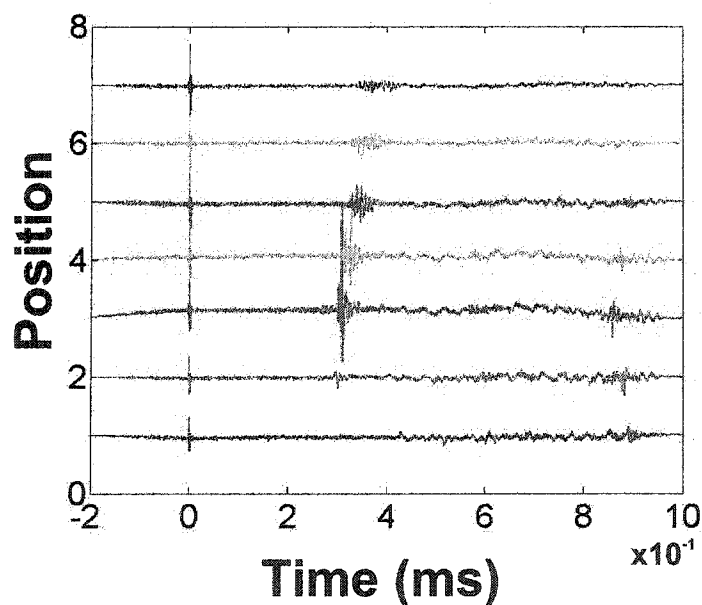


Figure 3.13 Typical impulse-response sampled at discrete locations along the plate. Each waveform is obtained as the result of the cross-correlation of the excitation with the received signal.

Results and discussion

The technique described in this chapter has been used in the reconstruction of the dispersion spectra for a variety of materials such as Plexiglas and aluminum, composite fibrous and layered materials, and wood. Critical parameters of the measurements are the path length over which the synthetic aperture coordinate scan is performed [104], [35] as well as the number of steps. The scan length determines the resolution on the wavenumber axis, while the number of steps determines the number of points on both x and k axis. The spatial step size or the spatial sampling frequency controls the maximum wavenumber obtainable. For each particular sample, the excitation waveform has been customized to achieve the maximum bandwidth, amplitude and spectral resolution, enhancing the unequivocal identification of the guided wave modes. Even though for certain samples, such as aluminum, a larger number of averages of the cross-correlated signal have been required, for most composites the reconstructed dispersion spectra have been obtained in real-time with very few averages.

Reference dispersion curves have been produced and plotted on top of the measurement results to ease comparison of the experimental results with the theoretically predicted results. No image enhancement has been performed on the experimental data.

Isotropic samples

The spectrum of the received voltage for a Plexiglas plate with a thickness of 5.5 mm (0.215 inch) is shown in fig. 3.14. The excitation signal has a broadband spectrum of about 800 kHz, with the starting frequency at 100 kHz. The incident angle has been set to a value of 7° . The second critical angle for Plexiglas is 18° . The measured spectrum reconstructs almost the entire phase-match angle range because the incident plane waves are spread from normal incidence to about 15° or 16° , and hence are very close to the angle of total reflection. Several guided wave modes are well defined and shown in red

color in fig. 3.14. These modes correspond (from bottom to top) to the A_0 , S_0 , A_1 , S_1 , A_2 , S_2 , S_3 , and A_3 modes. The guided wave modes, as the first symmetric mode S_0 , that have large out-of-plane displacements [95] are shown to couple energy more efficiently to a pressure wave in the air as shown by their higher brightness in the transmission coefficient spectrum. Good agreement with theoretical dispersion curves, Rayleigh-Lamb modes, that were calculated from waveguide theory, and numerical evaluation of the model received voltage model, that is presented in fig. 3.3, is observed because air is a tenuous medium. The low aerial density, $\rho_{air} = 1.2 \text{ g/m}^3$ [?], which produces high losses and weak signals, causes large acoustic impedance mismatches at the air-sample interfaces, such as air-aluminum $Z_{air}=0.0004 \text{ MRayl}$ and $Z_{aluminum}=17.33 \text{ MRayl}$. This difference implies also that the leakage losses of a propagating plate wave are generally negligible and the transmission maxima practically coincide with the Rayleigh-Lamb modes of the plate.

The RF signal has been sampled for a path along the x -axis corresponding to a synthetic aperture coordinate scan with a length of 160 mm and a step size of $\Delta x=2 \text{ mm}$. The scan started at $x_1 = -20 \text{ mm}$ and ended at $x_{80} = 140 \text{ mm}$ in the range in which the received voltage showed a relatively good, approximately 30, signal-to-noise ratio. Outside this interval, the signal has been found to have a value too low (less than 2% of the largest signal amplitude in a scan) to provide any additional information and therefore has been ignored. Zero position in the scan corresponds to the situation where the probes have their focus at the same location on the x -axis. Even though the signal is much smaller in the negative x -axis direction ($x_i \leq 0$ for the geometry shown in fig. 3.1), it still provides useful information, especially for those modes with negative group velocities, for example S_1 . Group velocity of a guided wave mode at a particular wavenumber-frequency point on the dispersion curve is determined by measuring the slope $d\omega/dk$ of the dispersion curve at that particular point (k, f) . The S_1 mode presents a negative group velocity between its cut-off ($k = 0$) and its minimum, as shown in fig. 3.14. The

spatial FFT produces both a positive and a negative wavenumber spectrum, and the negative group velocities modes can be extracted from the negative side of the spatial spectrum. The dotted curves plotted on top of the measured (k, f) spectrum correspond to the theoretically calculated guided wave modes, using the published average value of the stiffness of the Plexiglas. Although no fitting or matching has been performed on the measured data, good agreement between the experiment and the theory is seen.

The spectrum of the received voltage for an aluminum 6061 plate with a thickness of 6.68 mm (0.263 inch) is presented in fig. 3.15. This measurement has been significantly more time-consuming than the Plexiglas study because of the larger number of averages, 6000 to 9000, performed on the received cross-correlated signals, which has been required for reconstruction of the guided wave modes. The signal-to-noise ratio of the received voltage is approximately 20 in this experiment. The synthetic aperture coordinate scan was performed along the x -axis for a 300 mm total length, starting at $x_1 = -25$ mm and ending at $x_{150} = 275$ mm, with a step size $\Delta x = 2$ mm. The orientation angle was chosen to be 2° such that the angular range of the incident beam ($-6^\circ \leq \Delta\theta \leq 10^\circ$) excites the essential guided wave modes in aluminum plate (with 7.8° second critical angle). These settings allowed access to the wavenumber up to 0.5 mm^{-1} with a spatial spectral resolution of $(1/300) \text{ mm}^{-1}$. A common technique to improve the appearance of the spectrum without adding any new information has been zero padding of the data. The dashed and solid curves on the figure are calculated by use of published values for the elastic parameters of the aluminum [93] and are presented in table 3.1. Each of the peaks in the voltage spectrum corresponds to a different guided wave mode, their brightness is related to particular guided wave mode capacity to couple energy efficiently into air shown as a higher brightness in the transmission coefficient spectrum. In addition, incident beam orientation and focusing as well as transducer bandwidth influence the intensity of the measured guided wave modes by limiting the measurement region of the voltage spectrum. Good agreement of the experiment and the theory as

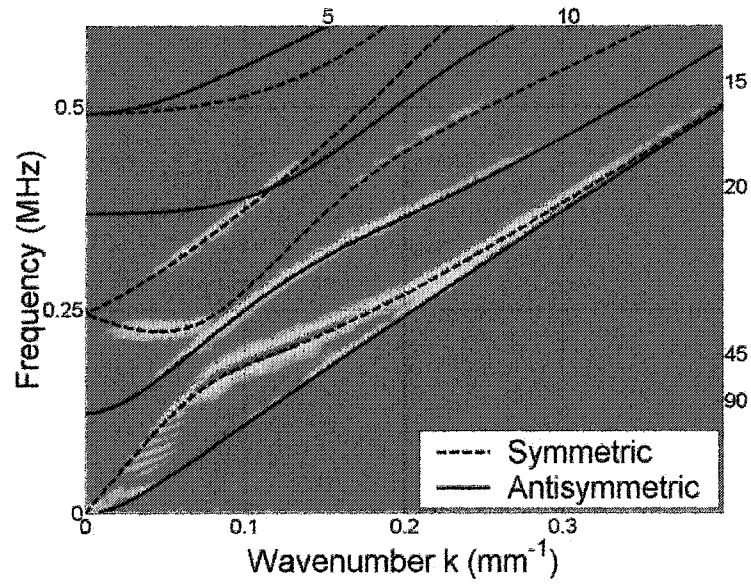


Figure 3.14 Measured voltage spectra for a Plexiglas plate. The curves represent the simulated antisymmetric (solid) and respectively symmetric (dashed) guided wave modes for the same plate in vacuum.

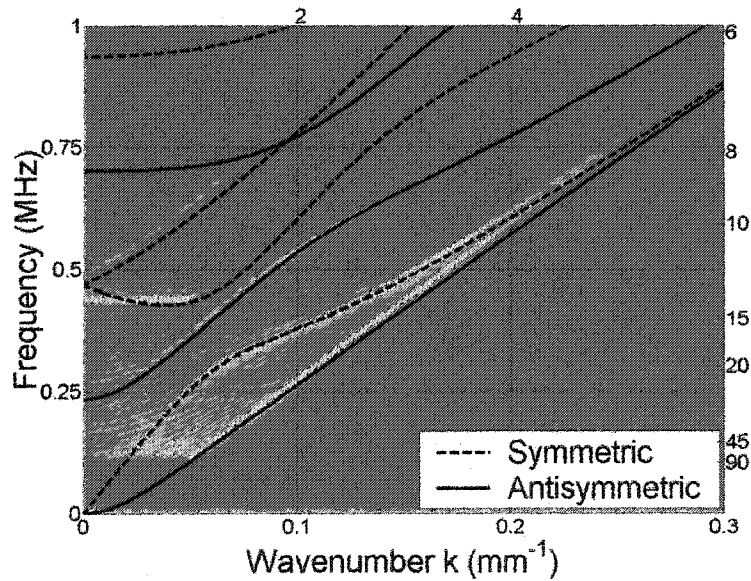


Figure 3.15 Measured voltage spectra for an aluminum 6061 plate. The curves represent the simulated antisymmetric (solid) and respectively symmetric (dashed) guided wave modes for the same plate in vacuum.

presented by the numerical evaluation of the received voltage model in fig. 3.2 is shown. The very small difference between the locus of the transmission coefficient peaks and the dispersion curves is a result of the usage in the theoretical model of average elastic stiffnesses published in literature and presented in table 3.1 rather than the actual values of a specific sample.

Composite material plates

The above method certainly not limited to isotropic materials such as Plexiglas and aluminum can be extended to anisotropic materials especially composites. Because of the interest in evaluation of elastic properties of composite materials, two types of composite – fibrous and a layered – have been inspected with our method. The first sample is a uniaxial glass-epoxy composite (SE84LV/EGL/300/400/37%, supplied by S P Systems [5]). The measurements have been performed on a path along, and across, the direction of the fibers. Fig. 3.16 shows the spectra of the received voltage measured along (top) and across (bottom) the fibers. Because the orientation angle has been set to 6° , the incident angular range is about 14° from normal. The composite is 3.3 mm thick and has been constructed from 20 pre-preg plies. The scan has been performed along the x -axis in the fiber direction starting at $x_1 = -36$ mm and ending at $x_{86} = 136$ mm and across the fibers from $x_1 = 20$ mm to $x_{50} = 80$ mm, with a step size of $\Delta x = 2$ mm. The length of the scan across the fibers has been limited by the size of the sample. This decrease in scan length produced a noisier, and hence lower quality, spectrum. The custom excitation signal used was a random phase noise with a bandwidth (100 kHz–900 kHz). The positions of peaks of the measured signals (peaks in the transmission coefficient) are in nearly the same locations as the dispersion curves and in excellent agreement when compared with the numerical evaluation of the model presented in fig. 3.4 and 3.5. As already stated, the tenuous nature of air, the low aerial density, is responsible for the fact that the peaks of the transmission coefficient and the Rayleigh-Lamb modes of the

medium coincide.

The layered composite plates, aluminum-aramid(90°) ARALL1 and ARALL3, are made from successive aluminum and aramid(90°) layers: ARALL1, with 5 aluminum and 4 aramid(90°) layers, and ARALL3, with 4 aluminum and 3 aramid(90°) layers. In fig. 3.17 the measured spectra are shown for the ARALL1 (top) and ARALL3 (bottom) layered composites. For the theoretical dispersion curves calculation, the values reported by Lobkis [63] have been used. The scan for the ARALL1 sample was performed for 200 mm along the x -axis, from $x_1 = -80$ mm to $x_{100} = 120$ mm with a step size of $\Delta x = 2$ mm. The orientation angle was set to $\alpha = 3^\circ$ with the incident beam having an angular spread $-5^\circ \leq \Delta\theta \leq 11^\circ$. The ARALL3 sample has been scanned from $x_1 = -60$ mm to $x_{100} = 140$ mm, with the same step size of $\Delta x = 2$ mm. The incident angle in this case has been set to $\alpha = 5^\circ$ ($-3^\circ \leq \Delta\theta \leq 13^\circ$). Only two guided wave modes are shown on the spectrum of the measured data for the ARALL3 composites, while for ARALL1 some higher order modes are observed. The small number of dispersive modes shown in the bandwidth of the probes is explained by the low value of the sample's thickness. Still, the results shown for the A_0 and S_0 are in clear agreement with the theoretical dotted curves.

Moderately anisotropic samples - wood plates

Any wood sample has an inherent anisotropy and different elastic properties from point to point, showing great variations even for samples taken from the same tree. The theoretical values of the stiffness of such materials will be only estimates; actual values vary from sample to sample and even along the same plate. Two wood samples have been selected for inspection: a basswood plate 6.350 mm thick and a balsa wood plate 9.525 mm thick. In both samples, the wood grain are orientated in the plane of incidence. The acoustic impedances of both basswood and balsa wood are very close to that of air, producing a good energy coupling to the samples. Both wood samples showed large

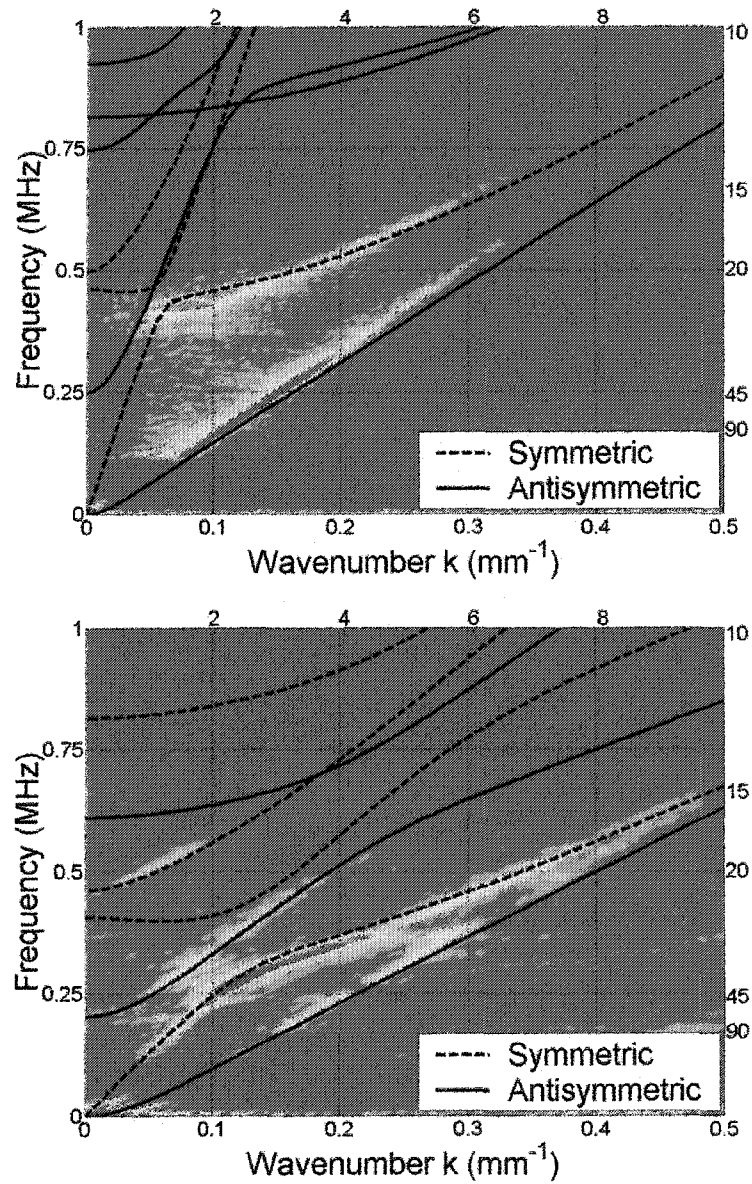


Figure 3.16 Measured voltage spectrum for a uniaxial glass-epoxy composite plate. The scan is performed along (top), and across (bottom), the fibers direction. The curves represent the simulated antisymmetric (solid) and symmetric (dashed) dispersive guided wave modes.

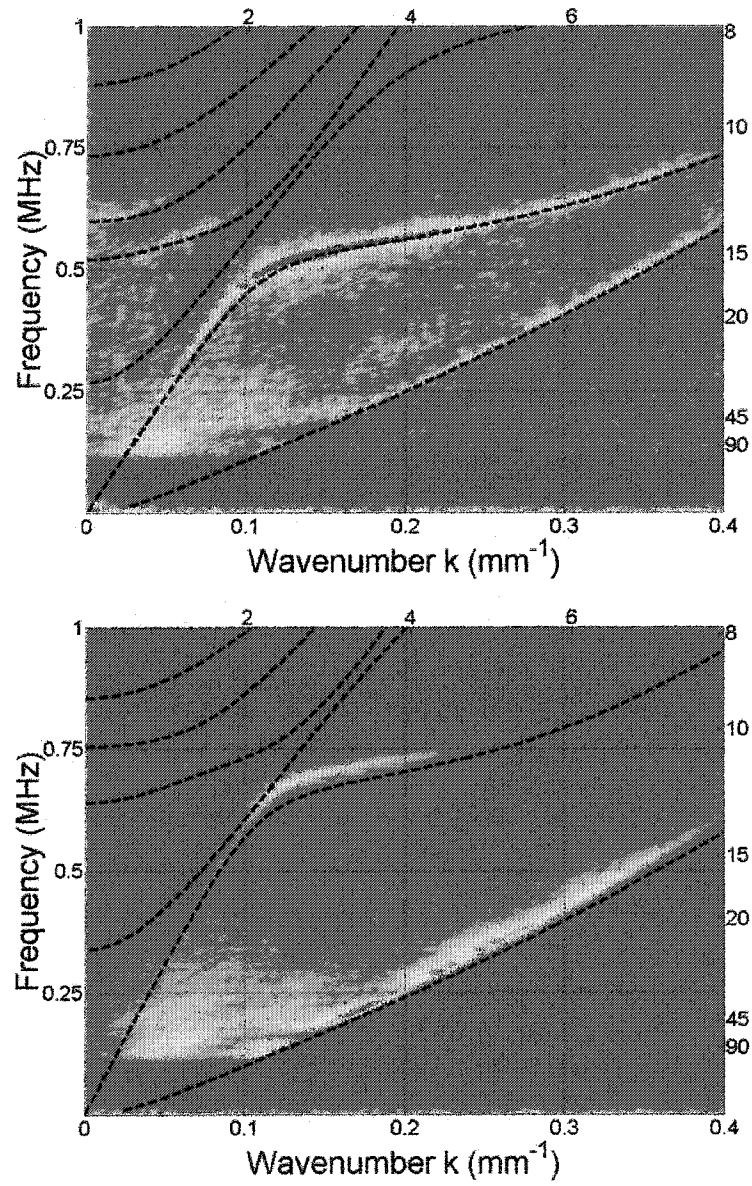


Figure 3.17 Measured voltage spectrum for layered composite plates: AR-ALL1 (top) and ARALL3 (bottom). The curves represent the simulated guided wave modes for the same plate in vacuum.

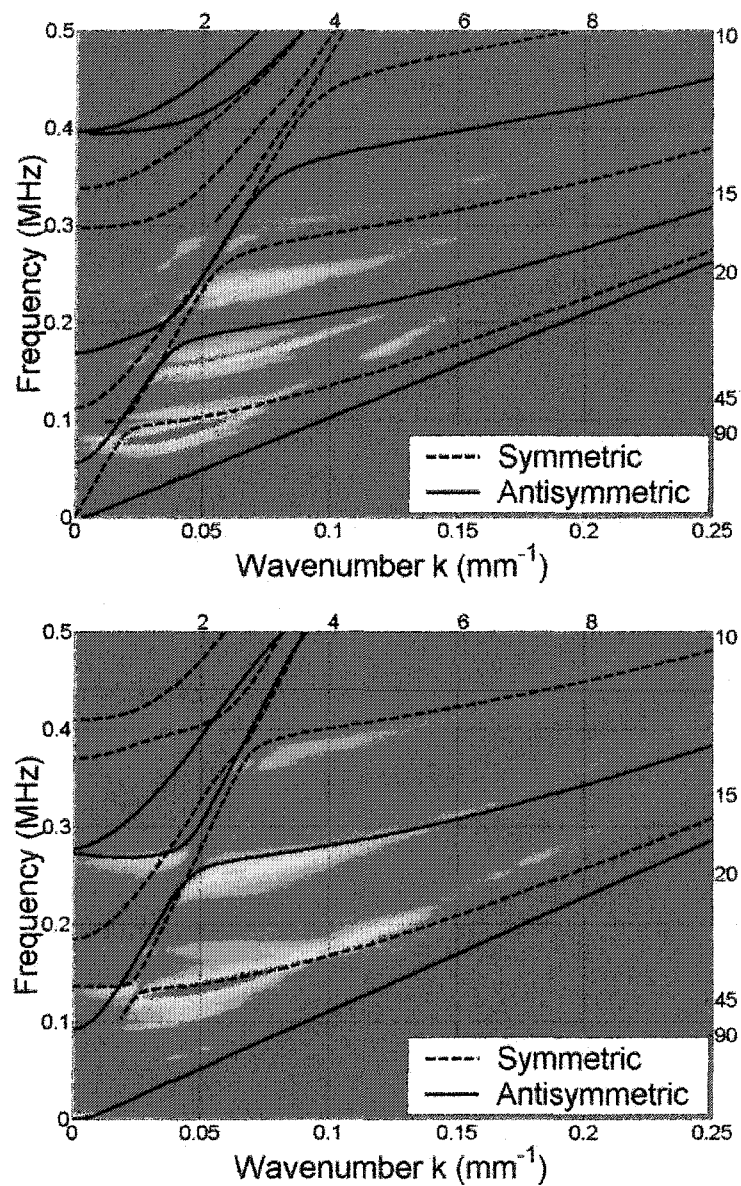


Figure 3.18 Measured voltage spectra for basswood (top) and balsa (bottom) wood plates. The curves represent the predicted anti-symmetric (solid) and respectively symmetric (dashed) guided wave modes.

attenuation of ultrasonic waves for frequencies above 500 kHz. The propagating guided waves were damped significantly along the plates (x -axis), making it difficult to perform long synthetic aperture coordinate scans.

In the case of basswood sample, the received voltage has been sampled for a path along the x -axis corresponding to a synthetic aperture coordinate scan with a length of 270 mm and a step size of $\Delta x = 3$ mm. The scan started at $x_1 = -30$ mm and ended at $x_{90} = 240$ mm in the range in which the received voltage showed a relatively good signal-to-noise ratio. The custom excitation signal has been designed to have its spectrum in the bandwidth 50 kHz to 600 kHz. In the case of the balsa wood, the line scan along the x -axis has been performed for a length of 240 mm (starting at $x_1 = -20$ mm and ending at $x_{80} = 220$ mm) with a $\Delta x = 3$ mm step size. The transducer orientation angle has been set to the value of $\alpha = 5^\circ$. In spite of the significant difference between the measured spectra and the theoretical model (fig. 3.6 and 3.7), the inspection method has been shown to provide important information about guided wave mode structure for each tested wood sample. It is important to emphasize that the values used in the model (1999 Wood Handbook of the United States Forest Service [37]) are estimations only, and the measured voltage spectra show a large number of guided wave modes to produce a good reconstruction of the actual values of elastic stiffness.

Estimation of the viscoelastic stiffness

The importance of experimentally determining the effective elastic property of materials, especially those with a complex microstructure such as composite materials is drawn from the demand for assurance of structural integrity, detection of environmental degradation and study of material aging. Knowledge of mechanical properties, i.e., elastic stiffnesses, and environmental impact on these properties is crucial to good engineering design.

To determine the elastic property of thin plates, the plane-wave transmission or reflec-

tion coefficient spectra have been commonly used by numerous researchers, as Chimenti extensively listed in a recent review [19]. Hosten *et al.* [47] exploited inhomogeneous waves to study lossy media, much as Weaver *et al.* [96] used point sources to generate transient waves to characterize composite laminates. To infer the viscoelastic stiffness of plates, without using group-velocity methods, Rokhlin and Wang [85] used time-of-flight in a through-transmission arrangement.

A critical contribution has been made by Rokhlin and Chimenti [84], and by Rogers [83] who demonstrated that specific areas of the plate dispersion spectrum have a predominant impact on specific elastic stiffnesses. Karim *et al.* [51] have used a simplex optimization algorithm to reconstruct the elastic stiffness from a full set of the reflection dispersion data. A similar approach has been taken by Sachse and Pao [87] for measuring the group and phase velocities of dispersive Lamb waves, by Alleyne and Cawley [3] for analyzing the scattering signals from defects in plates, and by Hosten *et al.* [46] for evaluating elastic constants in composite materials using air-coupled ultrasonic bulk waves.

Safaeinilli *et al.* [88], [89] developed an air-coupled method of estimating viscoelastic stiffness in plates, exploiting a detailed calculation to predict the measurable widths and relative heights of successive transmission maxima in air and are first to introduce the synthetic aperture coordinate scanning technique to extract from the measured signal the interference of the side lobes. Chimenti and Fei [23] and Fei *et al.* [32], [34]. developed this technique even further by producing rapid elastic stiffness reconstruction for reflection measurements performed with highly focused broadband water immersed probes in a single synthetic aperture coordinate scan. The reconstructed viscoelastic stiffnesses have been obtained by these researchers from the measured received voltage, with an iterative inverse algorithm targeting specific portions of dispersion curves. Their approach has been to begin the viscoelastic stiffnesses reconstruction from areas of the dispersion curves that depend heavily on one or two constants and to continue to add

data from other parts of the dispersion curves where additional constants can be easily extracted, until all relevant viscoelastic stiffnesses have been obtained with the desired error margin.

Conclusion

The broadband large angular range synthetic aperture coordinate scan technique has been applied to the reconstruction of the dispersion guided wave modes in an air-coupled ultrasonic experiment. A parabolic acoustic mirror has been designed to produce sufficient angular focusing to be able to excite and detect, through the phase-match coupling, most of the guided wave modes in the frequency bandwidth of non-contact probes. A pulse compression technique has been applied to the received voltage and demonstrated to extract only the impulse response of the inspected medium. This DSP technique has been shown to be a valuable tool in the process of filtering out the interference and noise sources.

A theoretical model for the received voltage has been adapted for comparison with the experiment. The experiments have been performed on both isotropic and anisotropic sample plates. The predicted locus of the guided wave modes for the tested sample has been shown to match well the peaks in the spectra of the received voltage. Good agreement has been found between the experiment and the theoretical prediction, even for wood samples, with their inherent variability of material properties.

Acknowledgments

This work was supported by the Center for Nondestructive Evaluation at Iowa State University. The author acknowledges the support of a graduate assistantship from the Institute for Physical Research and Technology at Iowa State University, and would like to thank Dr. Stephen D. Holland for help in the experiments and signal processing.

GENERAL CONCLUSIONS

Summary

In this dissertation, we have presented results of a study of the propagation of ultrasonic guided waves in composite plates. We have focused our analysis and experiments on two important nondestructive evaluation and materials characterization problems related to composites: the interface bond condition and non-contact elastic properties evaluation. New experimental techniques and theoretical methods have been developed in our approach to solve and to better understand those problems. We have studied the physical principles behind the experiments and have developed numerical models for comparison.

The study of the interface bond condition has been performed for a layered composite (glass-epoxy/balsa wood) known in industrial applications as the marine composite. The interest in this specific material comes from the fact that under certain loading conditions the bonding between the glass-epoxy facesheet and balsa is altered, producing a closed disbond also known as “kissing-disbond” (KDB). We developed a novel technique to detect this particular type of defect, which conventional normal incidence ultrasonic methods have failed to find. Our approach has been to select a propagating guided wave mode specific only to the facesheet and nonexistent in the spectrum of the ideal bond marine composite as a whole. Once this mode is found, we employ a fixed pitch-catch reflection setup and perform a C-scan of the sample. The presence of a minimum in the received leaky Lamb wave spectrum is a clear indication of a KSD. We have successfully

detected KSD in carried-to-completion experiments involving various artificially created defects. We exploited the global transfer matrix method to obtain the predicted reflection coefficient and the received voltage for various interface conditions. Good agreement between theoretical predictions and experimental values has been shown.

For non-contact elastic material properties evaluation, we have designed and developed methods for broadband focused measurements in air. The weak and inefficient generation of ultrasonic waves in air of the conventional transducers has motivated us to employ capacitive foil transducers in our experiments. To produce the desired wide angular range of the acoustic beam in air, we designed reflective parabolic mirrors. We have studied extensively, both theoretically and experimentally the characteristics of the air-coupled focused probes. Measurement of the acoustic pressure profile of the capacitive foil transducers has been performed in both planar and focused configurations. We have shown that our system is adequate to generate and detect acoustic waves in air. Our computationally efficient received voltage model has been compared with conventional models, and its numerical predictions have been found to be in good agreement with experimental results.

The direct correlation of the elastic material properties with the modes of the propagating wave in a plate has motivated us to develop a technique suitable for rapid non-contact reconstruction of the guided waves spectra. We exploited our custom broadband focused air-coupled system and a synthetic aperture scan technique to produce, in one line scan with only one incident angle, an almost complete spectrum of the Rayleigh-Lamb waves of various engineering materials subject to the bandwidth limitation of the transducers. We implemented a new pulse compression DSP method that, along with our fast data acquisition and processing capabilities, allowed us to perform rapid reconstruction and evaluation of the guided waves spectra. When we tested our method on numerous materials, the results were found to be in good agreement with theoretical predictions. The theory developed in this work has been a valuable tool in assisting us

to interpret the experimental results of various experiments.

Recommendations for future research

Our study of interface bond condition was limited to marine composites. Even though the experiments with those particular composites have been challenging because of the complexity of the materials, and although the results have been conclusive, we feel that further research needs to be done to expand our technique for detection of KSD in other layered composites. Furthermore, this method potentially has application in the detection of the closed delamination inside a composite plate. In order to apply this technique to the control of the manufacturing process of composite laminates considerable effort is also needed.

Efforts to obtain air-coupled ultrasonic measurements have been impeded by several experimental characteristics of our system, even though meaningful progress has been made. First, the duty cycle of the gated amplifier hindered the data acquisition speed of the measurements. The actual value highly recommended by the manufacturer, ten times less than the nominal value, has limited the experiments to an acquisition frequency of 15Hz. Though the parabolic mirrors have produced the desired wide angular range, we feel that the design of a native focused electrostatic probe would significantly improve the data quality. Finally, a careful comparison of results of the two- and three-dimensional experiments would be beneficial in identifying of the influence of the focusing mirror on the features of the reconstructed spectra.

APPENDIX A REFLECTION COEFFICIENT FOR A LAYERED COMPOSITE

The intent of this appendix is to show, in details, the derivation of the reflection coefficient of a layered elastic plate (i.e. glass-epoxy/balsa marine composite) in two experimental configurations: fluid loaded elastic layer/substrate system and immersed layered plate. The reason these two configurations were chosen is that both geometries are equally valid for modeling the marine composite; the numerical evaluation of the reflection coefficient of the marine composite does not show any significant difference when the results from both setups are compared. This is not surprising for the double-layer marine composite plate with the thickness of its balsa layer much larger (1 in) than the glass-epoxy layer (0.08 in) and with the wood grains orientated perpendicular to the interface. Even though the marine composite sample is a multilayered plate, the thickness and acoustic damping of the balsa layer allows us to treat it as a layer/substrate system.

The formulation presented here follows partially the approach establish by Nayfeh [77], [73]. The displacements and stresses for waves in unbounded elastic media are derived and expressed in the same fashion as the latter reference. The derivation of the reflection coefficient however is performed here using the Global Matrix approach rather than the Transfer Matrix preferred by Nayfeh. The Global Matrix Method was favored for being more stable in numerical evaluations of the reflection coefficients. An extensive study of these methods was done relatively recent by Lowe [66].

Formal solution for wave propagation in an unbounded elastic medium

The equation of motion for a generally anisotropic elastic medium is shown [73] to have the expression

$$\rho \ddot{u}_i = C_{ijkl} \frac{\partial^2 u_k}{\partial x_l \partial x_j}. \quad (\text{A.1})$$

where u_i are the projection of the displacement on the x_i -axis with $i = 1, 2, 3$, ρ is the density, and C_{ijkl} is the stiffness tensor of the elastic medium [59]. To ease the mathematical manipulation of equations, a good convention is to write the tensor C_{ijkl} in matrix notation. The contracted index notation consists in reducing by half the number of indices by replacing the pairs as follows, $11 \rightarrow 1$; $22 \rightarrow 2$; $33 \rightarrow 3$; $23 \rightarrow 4$; $13 \rightarrow 5$; $12 \rightarrow 6$. With this rule the stiffness tensor C_{ijkl} is rewritten as a stiffness matrix $C_{ijkl} \mapsto C_{IJ}$ with $i, j, k, \ell = 1, 2, 3$, and $I, J = 1, 2, \dots, 6$.

For a plane wave propagating in the plane $x_2 = 0$ under plane strain conditions, the motion is independent of x_2 and the formal solutions for the displacements u_i from the equation (A.1) are sought in the form

$$u_j = U_j e^{i\xi(x_1 + \alpha x_3 - vt)}, \quad (\text{A.2})$$

where U_j the displacement amplitude, $i = \sqrt{-1}$ in the imaginary unit, ξ is the x_1 -projection of the wavevector, α is the unknown ratio of the wavevector projection on x_3 and x_1 directions, and v is the phase velocity $v = \omega/\xi$ along x_1 . Application of the formal solution (A.2) to the equation of motion (A.1) for an elastic material with a monoclinic symmetry leads to three coupled equations

$$K_{ij}(\alpha)U_j = 0, \quad (i, j = 1, 2, 3), \quad (\text{A.3})$$

where the K_{ij} matrix is symmetric and its elements are

$$\begin{aligned} K_{11} &= C_{11} + C_{55}\alpha^2 - \rho v^2 & K_{12} &= C_{16} + C_{45}\alpha^2 \\ K_{22} &= C_{66} + C_{44}\alpha^2 - \rho v^2 & K_{13} &= (C_{13} + C_{55})\alpha \\ K_{33} &= C_{55} + C_{33}\alpha^2 - \rho v^2 & K_{23} &= (C_{36} + C_{45})\alpha. \end{aligned} \quad (\text{A.4})$$

In order to have a nontrivial solution for the displacement amplitudes U_1 , U_2 and U_3 the determinant of matrix K_{ij} must vanish. The condition $\det([K_{ij}])=0$ yields a secular equation in α that can be solved for different values of the phase velocity v ,

$$\alpha^6 + A_1\alpha^4 + A_2\alpha^2 + A_3 = 0. \quad (\text{A.5})$$

The coefficients of the equation (A.5) are explicitly listed below, as a function of the stiffness, density and phase velocity

$$\begin{aligned} A_1 = & [C_{11}C_{33}C_{44} - C_{13}^2C_{44} + 2C_{13}C_{36}C_{45} - 2C_{13}C_{44}C_{55} + 2C_{13}C_{45}^2 - 2C_{16}C_{33}C_{45} \\ & + C_{33}C_{55}C_{66} - C_{36}^2C_{55} - (C_{33}C_{44} + C_{33}C_{55} + C_{44}C_{55} - C_{45}^2)\rho v^2]/\Delta \end{aligned} \quad (\text{A.6a})$$

$$\begin{aligned} A_2 = & [C_{11}C_{33}C_{66} - C_{11}C_{36}^2 - 2C_{11}C_{36}C_{45} + C_{11}C_{44}C_{55} - C_{11}C_{45}^2 - C_{13}^2C_{66} \\ & + 2C_{13}C_{16}C_{36} + 2C_{13}C_{16}C_{45} - 2C_{13}C_{55}C_{66} - C_{16}^2C_{33} + 2C_{16}C_{36}C_{55} \\ & - (C_{11}C_{33} + C_{11}C_{44} - C_{13}^2 - 2C_{13}C_{55} - 2C_{16}C_{45} + C_{33}C_{66} - C_{36}^2 \\ & - 2C_{36}C_{45} + C_{44}C_{55} - C_{45}^2 + C_{55}C_{66})\rho v^2 + (C_{33} + C_{44} + C_{55})\rho^2 v^4]/\Delta \end{aligned} \quad (\text{A.6b})$$

$$\begin{aligned} A_3 = & [C_{11}C_{55}C_{66} - C_{16}^2C_{55} - (C_{11}C_{55} + C_{11}C_{66} - C_{16}^2 + C_{55}C_{66})\rho v^2 \\ & + (C_{11} + C_{55} + C_{66})\rho^2 v^4 - \rho^3 v^6]/\Delta \end{aligned} \quad (\text{A.6c})$$

$$\Delta = [C_{33}C_{44}C_{55} - C_{33}C_{45}^2] \quad (\text{A.6d})$$

Equation (A.5) has three distinct solutions for α^2 thus the solutions for α are obtained in pairs as

$$\alpha_1 = -\alpha_2, \quad \alpha_3 = -\alpha_4, \quad \alpha_5 = -\alpha_6, \quad (\text{A.7})$$

where α_1 and α_2 , α_3 and α_4 and respectively α_5 and α_6 correspond to the first, second and third solution in α^2 . Because the determinant $\det(K_{ij})$ is zero we can solve the equation (A.3) only for two of the displacement amplitudes as function of the third. Let's

consider the ratios of the displacements for all values of α_q , $q=1,2,\dots,6$ as $V_q = U_{2q}/U_{1q}$ and $W_q = U_{3q}/U_{1q}$ or explicitly as

$$V_q = (K_1 K_{23} - K_{13} K_{12}) / (K_{13} K_{22} - K_{12} K_{23}) \quad (\text{A.8a})$$

$$W_q = (K_{11} K_{23} - K_{12} K_{13}) / (K_{12} K_{33} - K_{23} K_{13}) \quad (\text{A.8b})$$

Using the superposition method, the formal solution for the displacements is obtained as

$$(u_1, u_2, u_3) = \sum_{q=1}^6 (1, V_q, W_q) U_{1q} e^{i\xi\alpha_q x_3}, \quad (\text{A.9})$$

and with the stress-strain relationship [59]

$$\sigma_{ij} = \frac{1}{2} C_{ij} \left(\frac{\partial u_i}{\partial x_j} + \frac{\partial u_j}{\partial x_i} \right), \quad i, j = 1, 2, 3 \quad (\text{A.10})$$

the stresses are obtained in the form

$$(\sigma_{33}^*, \sigma_{13}^*, \sigma_{23}^*) = \sum_{q=1}^6 (D_{1q}, D_{2q}, D_{3q}) U_{1q} e^{i\xi\alpha_q x_3}. \quad (\text{A.11})$$

The notation σ_{j3}^* , in the last equation, replaces $\sigma_{j3}/i\xi$ for $j=1,2,3$ for convenience. The coefficients D_{jq} , $j=1,2,3$ from the stress expression are

$$D_{1q} = C_{13} + C_{36}W_q + C_{33}\alpha W_q, \quad (\text{A.12a})$$

$$D_{2q} = C_{55}(a + W_q) + C_{45}\alpha W_q, \quad (\text{A.12b})$$

$$D_{3q} = C_{45}(a + W_q) + C_{44}\alpha W_q. \quad (\text{A.12c})$$

Because the solution of the equation (A.5) is obtained in pairs, the displacements and stresses amplitudes retain similar properties as

$$W_1 = -W_2 \quad W_3 = -W_4 \quad W_5 = -W_6 \quad (\text{A.13a})$$

$$V_1 = V_2 \quad V_3 = V_4 \quad V_5 = V_6 \quad (\text{A.13b})$$

$$D_{11} = D_{12} \quad D_{13} = D_{14} \quad D_{15} = D_{16} \quad (\text{A.13c})$$

$$D_{21} = -D_{22} \quad D_{23} = -D_{24} \quad D_{25} = -D_{26} \quad (\text{A.13d})$$

$$D_{31} = -D_{32} \quad D_{33} = -D_{34} \quad D_{35} = -D_{36} \quad (\text{A.13e})$$

Now, using the above properties, we can combine the displacements and stresses into an expanded matrix form that can be easily adapted to various boundary conditions. This expression (A.14) is exploited later to derive the reflection coefficient.

$$\begin{pmatrix} u_1 \\ u_2 \\ u_3 \\ \sigma_{33}^* \\ \sigma_{13}^* \\ \sigma_{23}^* \end{pmatrix} = \begin{pmatrix} 1 & 1 & 1 & 1 & 1 & 1 \\ V_1 & V_1 & V_3 & V_3 & V_5 & V_5 \\ W_1 & -W_1 & W_3 & -W_3 & W_5 & -W_5 \\ D_{11} & D_{11} & D_{13} & D_{13} & D_{15} & D_{15} \\ D_{21} & -D_{21} & D_{23} & -D_{23} & D_{25} & -D_{25} \\ D_{31} & -D_{31} & D_{33} & -D_{33} & D_{35} & -D_{35} \end{pmatrix} \begin{pmatrix} U_{11}E_1 \\ U_{12}E_2 \\ U_{13}E_3 \\ U_{14}E_4 \\ U_{15}E_5 \\ U_{16}E_6 \end{pmatrix} \quad (\text{A.14})$$

with $E_q = e^{i\xi\alpha_q x_3}$ for $q=1,2,\dots,6$.

In the case of the elastic materials with a higher symmetry, *i.e.* orthotropic, for propagation directions that do not coincide with any of the principal axes directions, the formal solutions derived for the monoclinic material can be used as well. When the propagation is considered along one of the axes of symmetry some of the stiffnesses vanish and the monoclinic derivation cannot be applied. Let's consider now specifically the propagation to be along one of the axes of symmetry, namely x_1 for an orthotropic material. The equation of motion written explicitly defines two decoupled motions: one in the sagittal plane for longitudinal and vertically polarized shear (SV) wave assuming plane strain condition and the second for a horizontally polarized shear (SH) wave. The formal solution for SH waves, sought in the same form as (A.2), is given by

$$u_2 = \sum_{q=1}^2 U_{2q} e^{i\xi\alpha_q x_3}, \quad (\text{A.15a})$$

$$\sigma_{23} = \sum_{q=1}^2 i\xi D_{2q} U_{2q} e^{i\xi\alpha_q x_3}, \quad (\text{A.15b})$$

with

$$\alpha_1 = -\alpha_2 = \sqrt{\frac{\rho v^2 - C_{66}}{C_{44}}}, \quad (\text{A.16a})$$

$$D_{21} = -D_{22} = \alpha_1 C_{44}. \quad (\text{A.16b})$$

For a wave propagating in the sagittal plane, the formal solution is obtained as

$$(u_1, u_3) = \sum_{q=1}^4 (1, W_q) U_{1q} e^{i\xi \alpha_q x_3} \quad (\text{A.17a})$$

$$(\sigma_{33}, \sigma_{13}) = \sum_{q=1}^4 i\xi (D_{1q}, D_{3q}) U_{1q} e^{i\xi \alpha_q x_3}. \quad (\text{A.17b})$$

The K_{ij} matrix is reduced to a 2x2 matrix with the elements

$$\begin{aligned} K_{11} &= C_{11} + C_{55}\alpha^2 - \rho v^2, \\ K_{12} &= (C_{13} + C_{55})\alpha, \\ K_{22} &= C_{55} + C_{33}\alpha^2 - \rho v^2. \end{aligned} \quad (\text{A.18})$$

The existence of a nontrivial solution produces the equation in α

$$A\alpha^4 + B\alpha^2 + C = 0, \quad (\text{A.19})$$

with

$$\begin{aligned} A &= C_{33}C_{55}, \\ B &= (C_{11} - \rho v^2)C_{33} + (C_{55} - \rho v^2)C_{55} - (C_{13} + C_{55})^2, \\ C &= (C_{11} - \rho v^2)(C_{55} - \rho v^2). \end{aligned}$$

The equation (A.19) admits two solution for α^2 thus four in α with: $\alpha_1 = -\alpha_2$ and $\alpha_3 = -\alpha_4$. The displacement amplitude ratio W_q and the stress terms D_{1q} , D_{3q} are

$$W_q = \frac{(C_{13} + C_{55})\alpha_q}{\rho v^2 - C_{55} - \alpha^2 C_{33}}, \quad (\text{A.20a})$$

$$D_{1q} = C_{13} + \alpha_q C_{33} W_q, \quad (\text{A.20b})$$

$$D_{3q} = C_{55}(\alpha_q + W_q), \quad (\text{A.20c})$$

for $q = \overline{1, 4}$. As was shown before

$$W_1 = -W_2 \qquad W_3 = -W_4 \qquad (\text{A.21a})$$

$$D_{11} = D_{12} \qquad D_{13} = D_{14} \qquad (\text{A.21b})$$

$$D_{31} = -D_{32} \qquad D_{33} = -D_{34} \qquad (\text{A.21c})$$

because of the relationship that exists between the solutions of equation (A.19).

For any propagating direction in an isotropic material the motion is decoupled in sagittal plane motion and SH waves. The formal solution is then further simplified because of the higher symmetry but the same expressions, as that described for the case of the orthotropic material, can be used. The formal solution for the fluid media was found to have the same form as Nayfeh [73] ch. 5, pp. 80. The displacements and stresses can be expressed in a form similar to equation (A.14) for all the cases mentioned. The matrix expression is useful for evaluating the reflection and transmission coefficients for various configurations. In the following paragraph two cases are shown explicitly: a fluid loaded orthotropic plate with a solid substrate, and a completely immersed plate with two monoclinic layers.

Fluid loaded elastic layer with a solid substrate

The system a fluid loaded elastic layer with a solid substrate is shown in fig. (1.8) The fluid is considered to be nonviscous. The boundary conditions for the fluid-layer interface ($x_3 = -d/2$) are

$$\begin{aligned} u_3^f(-d/2) &= u_3^p(-d/2), \\ \sigma_{33}^f(-d/2) &= \sigma_{33}^p(-d/2), \\ 0 &= \sigma_{13}^p(-d/2), \end{aligned} \qquad (\text{A.22})$$

and for layer-substrate interface ($x_3 = d/2$) are

$$\begin{aligned}
 u_1^p(d/2) &= \eta_1 u_1^s(d/2), \\
 u_3^p(d/2) &= \eta_2 u_3^s(d/2), \\
 \sigma_{33}^p(d/2) &= \eta_3 \sigma_{33}^s(d/2), \\
 \sigma_{13}^p(d/2) &= \eta_4 \sigma_{13}^s(d/2).
 \end{aligned} \tag{A.23}$$

The superscript f, p and respectively s denotes the fluid, the elastic layer and respectively the substrate. The coefficient η_i describes the bonding between the plate and substrate, taking values in the interval $0 \leq \eta_i \leq 1$, $i = \overline{1, 4}$ (the actual values of η_i that were used in simulations are listed in the parameter files on the attached CD-ROM). A rigid bonding requires continuity of the displacements and stresses across the plate-substrate interface ($\eta_i = 1$, $i = \overline{1, 4}$). The case in which η_i vanishes ($\eta_i = 0$, $i = \overline{1, 4}$) represents the fluid-plate-vacuum problem. The smooth interface can be modeled by setting $\eta_2 = \eta_3 = 1$ and $\eta_1 = \eta_4 = 0$ and the rough interface with intermediate values for η_i , $i = \overline{1, 4}$. Using the appropriate formal solutions for fluid, plate and substrate, we can arrange the boundary conditions (A.22) and (A.23) into a system of seven equations where the unknown are the displacement amplitudes in the layer U_{1j}^p , $j = \overline{1, 4}$, the reflection coefficient R in the fluid, the longitudinal wave transmission coefficient T_L and the vertical shear transmission coefficient T_{SV} in the substrate.

If the amplitude of the incident wave in the fluid, U_1^f , is arbitrarily chosen to be unity for convenience, the amplitude of the reflected wave back in the fluid, U_2^f , can be identify with the reflection coefficient R . Also the amplitudes of the waves propagating into the solid substrate will be obtained as $U_1^s = T_L$, $U_3^s = T_{SV}$, and $U_2^s = U_4^s = 0$. The last two amplitudes vanish because there are no incoming waves from the substrate to the layer. After arranging the boundary equations into a system of equations we obtain a 9 by 7 matrix but two of the columns can be eliminated because they are multiplied with the vanishing amplitudes in the solid substrate namely U_2^s and U_4^s . Thus the matrix of the system of equations is reduced to a size of 7x7 as shown below.

$$\begin{bmatrix}
W_1^p \overline{E_1} & -W_1^p E_1 & W_3^p \overline{E_3} & -W_3^p E_3 & \alpha_f & 0 & 0 \\
D_{11}^p \overline{E_1} & D_{11}^p E_1 & D_{13}^p \overline{E_3} & D_{13}^p E_3 & -\rho_f v^2 & 0 & 0 \\
D_{31}^p \overline{E_1} & -D_{31}^p E_1 & D_{33}^p \overline{E_3} & -D_{33}^p E_3 & 0 & 0 & 0 \\
E_1 & \overline{E_1} & E_3 & \overline{E_3} & 0 & \eta_1 & \eta_1 \\
W_1^p E_1 & -W_1^p \overline{E_1} & W_3^p E_3 & -W_3^p \overline{E_3} & 0 & \eta_2 W_1^s & \eta_2 W_3^s \\
D_{11}^p E_1 & D_{11}^p \overline{E_1} & D_{13}^p E_3 & D_{13}^p \overline{E_3} & 0 & \eta_3 D_{11}^s & \eta_3 D_{13}^s \\
D_{31}^p E_1 & -D_{31}^p \overline{E_1} & D_{33}^p E_3 & -D_{33}^p \overline{E_3} & 0 & \eta_4 D_{31}^s & \eta_4 D_{33}^s
\end{bmatrix}
\begin{pmatrix} U_{11}^p \\ U_{12}^p \\ U_{13}^p \\ U_{14}^p \\ R \\ T_L \\ T_{SV} \end{pmatrix} = \begin{pmatrix} \alpha_f \\ \rho_f v^2 \\ 0 \\ 0 \\ 0 \\ 0 \\ 0 \end{pmatrix} \quad (\text{A.24})$$

with $E_1 = e^{i\xi\alpha_1 d/2}$, $\overline{E_1} = e^{-i\xi\alpha_1 d/2}$, $E_3 = e^{i\xi\alpha_3 d/2}$, $\overline{E_3} = e^{-i\xi\alpha_3 d/2}$. Using the notations

$$\begin{aligned}
E_1 + \overline{E_1} &= e^{i\xi\alpha_1 d/2} + e^{-i\xi\alpha_1 d/2} = 2 \cos(\xi\alpha_1 d/2) = 2 \cos_1, \\
E_1 - \overline{E_1} &= e^{i\xi\alpha_1 d/2} - e^{-i\xi\alpha_1 d/2} = 2i \sin(\xi\alpha_1 d/2) = 2i \sin_1, \\
E_3 + \overline{E_3} &= e^{i\xi\alpha_3 d/2} + e^{-i\xi\alpha_3 d/2} = 2 \cos(\xi\alpha_3 d/2) = 2 \cos_3, \\
E_3 - \overline{E_3} &= e^{i\xi\alpha_3 d/2} - e^{-i\xi\alpha_3 d/2} = 2i \sin(\xi\alpha_3 d/2) = 2i \sin_3,
\end{aligned} \quad (\text{A.25})$$

we multiply with -1 the 2^{nd} and 4^{th} column and we add them to the 1^{st} respectively 3^{rd} column followed by the addition of the initial 1^{st} and 3^{rd} column to the 2^{nd} and respectively 4^{th} column. These operations yield

$$\begin{bmatrix}
2W_1^p \cos_1 & -2iW_1^p \sin_1 & 2W_3^p \cos_3 & -2iW_3^p \sin_3 & \alpha_f & 0 & 0 \\
-2iD_{11}^p \sin_1 & 2D_{11}^p \cos_1 & -2iD_{13}^p \sin_3 & 2D_{13}^p \cos_3 & -\rho_f v^2 & 0 & 0 \\
2D_{31}^p \cos_1 & -2iD_{31}^p \sin_1 & 2D_{33}^p \cos_3 & -2iD_{33}^p \sin_3 & 0 & 0 & 0 \\
2i \sin_1 & 2 \cos_1 & 2i \sin_3 & 2 \cos_3 & 0 & \eta_1 & \eta_1 \\
2W_1^p \cos_1 & 2iW_1^p \sin_1 & 2W_3^p \cos_3 & 2iW_3^p \sin_3 & 0 & \eta_2 W_1^s & \eta_2 W_3^s \\
2iD_{11}^p \sin_1 & 2D_{11}^p \cos_1 & 2iD_{13}^p \sin_3 & 2D_{13}^p \cos_3 & 0 & \eta_3 D_{11}^s & \eta_3 D_{13}^s \\
2D_{31}^p \cos_1 & 2iD_{31}^p \sin_1 & 2D_{33}^p \cos_3 & 2iD_{33}^p \sin_3 & 0 & \eta_4 D_{31}^s & \eta_4 D_{33}^s
\end{bmatrix} \quad (\text{A.26})$$

We factor out the coefficient 2 from first 4 columns and -1 from the 2^{nd} row and add the 4^{th} , 5^{th} and 6^{th} rows to the 1^{st} , 2^{nd} and respectively 3^{rd} rows and subsequently subtract

half of the 1st, 2nd and 3rd rows from 4th, 5th and respectively 6th rows.

$$\begin{bmatrix} W_1^p \cos_1 & 0 & W_3^p \cos_3 & 0 & \alpha_f & \eta_2 W_1^s & \eta_2 W_3^s \\ iD_{11}^p \sin_1 & 0 & iD_{13}^p \sin_3 & 0 & \rho_f v^2 & \eta_3 D_{11}^s & \eta_3 D_{13}^s \\ D_{31}^p \cos_1 & 0 & D_{33}^p \cos_3 & 0 & 0 & \eta_4 D_{31}^s & \eta_4 D_{33}^s \\ i \sin_1 & \cos_1 & i \sin_3 & \cos_3 & 0 & 2\eta_1 & 2\eta_1 \\ 0 & iW_1^p \sin_1 & 0 & iW_3^p \sin_3 & -\alpha_f & \eta_2 W_1^s & \eta_2 W_3^s \\ 0 & D_{11}^p \cos_1 & 0 & D_{13}^p \cos_3 & -\rho_f v^2 & \eta_3 D_{11}^s & \eta_3 D_{13}^s \\ 0 & iD_{31}^p \sin_1 & 0 & iD_{33}^p \sin_3 & 0 & \eta_4 D_{31}^s & \eta_4 D_{33}^s \end{bmatrix} \quad (\text{A.27})$$

We divide the 1st and 3rd columns with \cos_1 respectively \cos_3 and similarly the 2nd and 4th columns with \sin_1 respectively \sin_3 . The rearranged determinant is

$$\begin{bmatrix} 1 & W_1^p & W_3^p & 0 & 0 & \eta_2 W_1^s & \eta_2 W_3^s \\ -i\rho_f v^2/\alpha_f & D_{11}^p T_1 & D_{13}^p T_3 & 0 & 0 & -i\eta_3 D_{11}^s & -i\eta_3 D_{13}^s \\ 0 & D_{31}^p & D_{33}^p & 0 & 0 & \eta_4 D_{31}^s & \eta_4 D_{33}^s \\ 0 & iT_1 & iT_3 & C_1 & C_3 & 2\eta_1 & 2\eta_1 \\ i & 0 & 0 & W_1^p & W_3^p & -i\eta_2 W_1^s & -i\eta_2 W_3^s \\ -\rho_f v^2/\alpha_f & 0 & 0 & D_{11}^p C_1 & D_{13}^p C_3 & \eta_3 D_{11}^s & \eta_3 D_{13}^s \\ 0 & 0 & 0 & D_{31}^p & D_{33}^p & -i\eta_4 D_{31}^s & -i\eta_4 D_{33}^s \end{bmatrix} \quad (\text{A.28})$$

With the notation: $F = \rho_f v^2/\alpha_f$, $W_1 = \eta_2 W_1^s$, $W_3 = \eta_2 W_3^s$, $D_{11} = -i\eta_3 D_{11}^s$, $D_{13} = -i\eta_3 D_{13}^s$, $D_{31} = \eta_4 D_{31}^s$, $D_{33} = \eta_4 D_{33}^s$ and $Q = 2\eta_1$ the determinant becomes

$$\begin{bmatrix} 1 & W_1^p & W_3^p & 0 & 0 & W_1 & W_3 \\ -iF & D_{11}^p T_1 & D_{13}^p T_3 & 0 & 0 & -iD_{11} & -iD_{13} \\ 0 & D_{31}^p & D_{33}^p & 0 & 0 & D_{31} & D_{33} \\ 0 & iT_1 & iT_3 & C_1 & C_3 & Q & Q \\ i & 0 & 0 & W_1^p & W_3^p & -iW_1 & -iW_3 \\ -F & 0 & 0 & D_{11}^p C_1 & D_{13}^p C_3 & D_{11} & D_{13} \\ 0 & 0 & 0 & D_{31}^p & D_{33}^p & -iD_{31} & -iD_{33} \end{bmatrix} \quad (\text{A.29})$$

Using Cramer's rule [42], the reflection coefficient can be easily derived as

$$R = \frac{\Delta_R}{\Delta} = \frac{(\Delta_1 + i\Delta_5) - F(\Delta_6 + i\Delta_2)}{(\Delta_1 + i\Delta_5) + F(\Delta_6 + i\Delta_2)}, \quad (\text{A.30})$$

with the terms Δ_i , ($i = 1, 2, 5, 6$) the determinants of 6x6 matrices. The exact expressions of these parameters are obtained using the Maple program, RCIsb.mws included on the attached CD-ROM. If the notations $\Delta_{ps} = (\Delta_1 + i\Delta_5)$ and $Y_{ps} = (\Delta_6 + i\Delta_2)$ are used the expression of the reflection coefficient reduces to the familiar form (1.8)

$$R = \frac{\Delta_{ps} - Y_{ps}}{\Delta_{ps} + Y_{ps}} \quad (\text{A.31})$$

with the terms $\Delta_{ps} = (\Delta_1 + i\Delta_5)$ and $Y_{ps} = (\Delta_6 + i\Delta_2)$ given by

$$\begin{aligned} \Delta_{ps} = & i [D_{11}D_{33} - D_{31}D_{13}] \{A(W_1^p C_3 - W_3^p C_1) + (D_{33}^p T_1 - D_{31}^p T_3) \\ & (W_1^p D_{13}^p C_3 - W_3^p D_{11}^p C_1) - T_1 T_3 (D_{11}^p - D_{33}^p) (W_1^p D_{33}^p - W_3^p D_{31}^p) + \\ & + (W_1^p T_3 - W_3^p T_1) S - C_1 C_3 (D_{11}^p - D_{13}^p) (W_1^p D_{33}^p - W_3^p D_{31}^p) + \\ & + (W_1^p D_{13}^p T_3 - W_3^p D_{11}^p T_1) (D_{33}^p C_1 - D_{31}^p C_3) \} + \\ & + 2i [W_3 D_{11} - W_1 D_{13}] \{A(D_{33}^p C_1 - D_{31}^p C_3) + S(D_{33}^p T_1 - D_{31}^p T_3)\} + \\ & + 2 [W_3 D_{31} - W_1 D_{33}] \{(AC_1 C_3 - ST_1 T_3) (D_{11}^p - D_{13}^p)\} + \\ & + [(D_{11} - D_{13})Q] \{A(W_1^p D_{33}^p - W_3^p D_{31}^p) - (W_1^p D_{33}^p - W_3^p D_{31}^p) S\} + \\ & + i [(D_{31} - D_{33})Q] \{A(W_1^p D_{13}^p C_3 - W_3^p D_{11}^p C_1) + \\ & + (W_1^p D_{13}^p T_3 - W_3^p D_{11}^p T_1) S\} + \\ & + 2i [(W_1 - W_3)Q] \{AS\} \end{aligned} \quad (\text{A.32})$$

$$\begin{aligned}
Y_{ps} = & 2[D_{11}D_{33} - D_{31}D_{13}] \{ (D_{33}^p W_1^p - D_{31}^p W_3^p) [W_1^p(T_3 - C_3) - W_3^p(T_1 - C_1)] \} + \\
& + 2[W_1D_{13} - W_3D_{11}] \{ (D_{33}^p W_1^p - D_{31}^p W_3^p) [(D_{31}^p(T_3 - C_3) - D_{33}^p(T_1 - C_2))] \} + \\
& + i[W_3D_{31} - W_1D_{33}] \{ T_1T_3(D_{11}^p - D_{13}^p)(D_{33}^p W_1^p - D_{31}^p W_3^p) + \\
& + (W_3^p C_1 - W_1^p C_3)A + (W_1^p D_{13}^p T_3 - W_3^p D_{11}^p T_1)(D_{33}^p C_1 - D_{31}^p C_3) - \\
& - (D_{31}^p T_3 - D_{33}^p T_1)(D_{13}^p W_1^p C_3 - D_{11}^p W_3^p C_1) - \\
& - C_1 C_3 (D_{33}^p W_1^p - D_{31}^p W_3^p)(D_{31}^p - D_{11}^p) - (W_1^p T_3 - W_3^p T_1)S \} + \\
& + 2i[(D_{11} - D_{13})Q] \{ (D_{33}^p W_1^p - D_{31}^p W_3^p) \} + \\
& + [(D_{31} - D_{33})Q] \{ (W_1^p D_{13}^p T_3 - W_3^p D_{11}^p T_1)(D_{33}^p W_1^p - D_{31}^p W_3^p) + \\
& + i(D_{33}^p W_1^p - D_{31}^p W_3^p)(D_{13}^p W_1^p C_3 - D_{11}^p W_3^p C_1) \} + \\
& + [(W_1 - W_3)Q] \{ (D_{33}^p W_1^p - D_{31}^p W_3^p)A - (D_{33}^p W_1^p - D_{31}^p W_3^p)S \}
\end{aligned} \tag{A.33}$$

In fig. A.1 is presented the numerical evaluation of the reflection coefficient for the water loaded glass-epoxy/balsa system with ideal bonding. The geometrical setup is shown in fig. 1.8. The thickness of the glass-epoxy layer is 0.08 in. The wood grains are perpendicular to the interface. The reflection coefficient is evaluated for 500x500 frequency-wavenumber values equally spaced in the range 0 - 2 MHz and respectively 0 - 5 mm^{-1} . The red color represents the lowest amplitude while the dark blue the highest value (≈ 1). The minima in the reflection coefficient are indications of a propagating guided wave mode. With the same setup parameters the reflection coefficient is evaluated for the KDB case and presented in fig. A.2. The net difference between the spectra of the same composite in the case of a good bond and a KDB is shown in fig. A.3. The red color shows here the maxima in the net difference between the two spectra. It can be seen that the maxima is concentrated around a phase-match angle of $15^\circ \pm 3^\circ$. The same result was observed experimentally and exploited to distinguish KDB areas in the C-Scan of the sample.

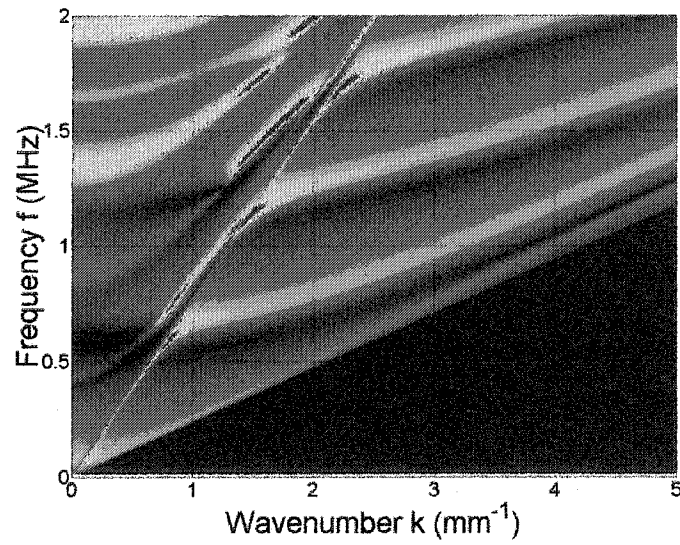


Figure A.1 Numerical evaluation of the reflection coefficient for a water loaded glass-epoxy/balsa system. The bonding between top layer and the balsa substrate is considered ideal.

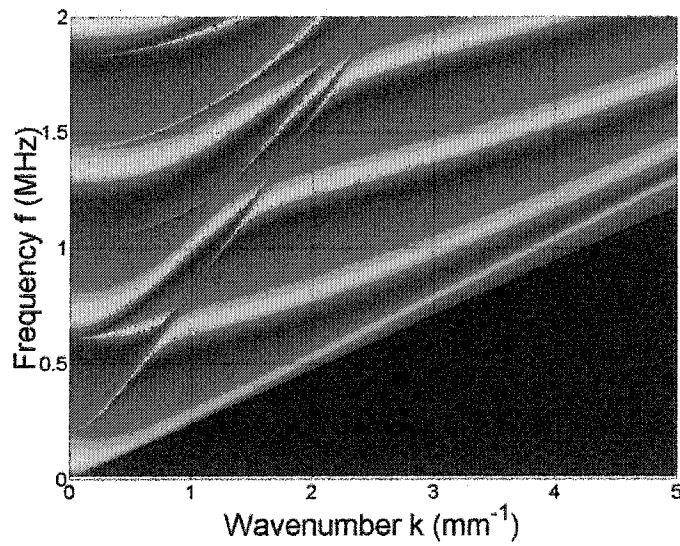


Figure A.2 Numerical evaluation of the reflection coefficient for a water loaded glass-epoxy/balsa system for the KDB case. All parameters are kept constant from the previous case except for the boundary conditions.

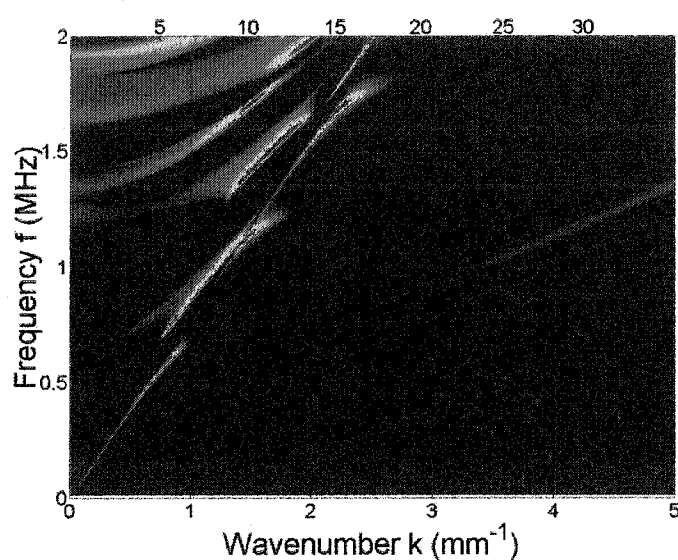


Figure A.3 The difference in the numerical evaluation of the reflection coefficient between the good bond and KDB cases. The top horizontal and right vertical axes show the phase-match angle in water. The largest difference is concentrated at $15^\circ \pm 3^\circ$. For a frequency of 1MHz the maximum is located at 17° which it is in good agreement with the experiment.

Completely immersed double layer elastic plate

The fluid loaded multilayer elastic plate is shown in fig. (A.4). Both the upper (superscript u) and lower (superscript d) fluids are considered to be nonviscous. The thickness of the first layer (A) is d_A and of the second layer (B) is d_B . There are three boundary conditions for each fluid-solid interface and four for the solid-solid interlayer bond, ten equations in total.

The boundary conditions for the upper fluid-layer A interface ($x_3 = -d_A$) are

$$\begin{aligned} u_3^u(-d_A) &= u_3^a(-d_A), \\ \sigma_{33}^u(-d_A) &= \sigma_{33}^a(-d_A), \\ 0 &= \sigma_{13}^a(-d_A), \end{aligned} \tag{A.34}$$

for interlayer interface ($x_3 = 0$) are

$$\begin{aligned} u_1^a(0) &= \eta_1 u_1^s(0), \\ u_3^a(0) &= \eta_2 u_3^s(0), \\ \sigma_{33}^a(0) &= \eta_3 \sigma_{33}^b(0), \\ \sigma_{13}^a(0) &= \eta_4 \sigma_{13}^b(0), \end{aligned} \tag{A.35}$$

and for the layer B - lower fluid interface ($x_3 = d_B$) are

$$\begin{aligned} u_3^b(d_B) &= u_3^d(d_B), \\ \sigma_{33}^b(d_B) &= \sigma_{33}^d(d_B), \\ \sigma_{13}^b(d_B) &= 0. \end{aligned} \tag{A.36}$$

As we done in the previous section, the amplitude of the incident wave in fluid in arbitrarily considered to be unity, $U_1^u = 1$. The result of this convenient assumption is that the amplitude of the reflected respectively transmitted wave into fluid can be identified with the reflection respectively transmission coefficient, $U_2^u = R$ and $U_1^d = T$. The amplitude $U_3^d = 0$ because there is no incoming wave from the lower fluid. The boundary conditions can be arranged in a system of nine equation with nine unknowns.

The system of equation can then be solved for any of the variables: the reflection and transmission coefficients and eight displacement amplitudes, four for each solid layer. The resulting matrix is given by

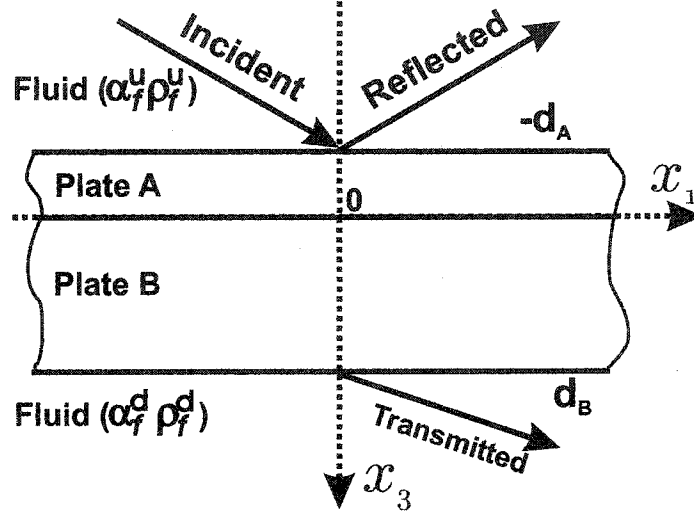


Figure A.4 Scattering from a fluid loaded two layers plate. The x_1 axis is parallel to the interfaces and located at the boundary between plates. The thicknesses of the plates are d_A for plate A and respectively d_B for plate B. Two different fluids can be considered for both top and bottom interfaces.

$$\begin{bmatrix}
 W_1^a \overline{E_1^a} & -W_1^a E_1^a & W_3^a \overline{E_3^a} & -W_3^a E_3^a & \alpha_f^u & 0 & 0 & 0 & 0 & 0 \\
 D_{11}^a \overline{E_1^a} & D_{11}^a E_1^a & D_{13}^a \overline{E_3^a} & D_{13}^a E_3^a & -\rho_f^u v^2 & 0 & 0 & 0 & 0 & 0 \\
 D_{31}^a \overline{E_1^a} & -D_{31}^a E_1^a & D_{33}^a \overline{E_3^a} & -D_{33}^a E_3^a & 0 & 0 & 0 & 0 & 0 & 0 \\
 E_1^a & \overline{E_1^a} & E_3^a & \overline{E_3^a} & 0 & \eta_1 \overline{E_1^b} & \eta_1 E_1^b & \eta_1 \overline{E_3^b} & \eta_1 E_3^b & 0 \\
 W_1^a E_1^a & -W_1^a \overline{E_1^a} & W_3^a E_3^a & -W_3^a \overline{E_3^a} & 0 & \eta_2 W_1^b \overline{E_1^b} & -\eta_2 W_1^b E_1^b & \eta_2 W_3^b \overline{E_3^b} & -\eta_2 W_3^b E_3^b & 0 \\
 D_{11}^a E_1^a & D_{11}^a \overline{E_1^a} & D_{13}^a E_3^a & D_{13}^a \overline{E_3^a} & 0 & \eta_3 D_{11}^b \overline{E_1^b} & \eta_3 D_{11}^b E_1^b & \eta_3 D_{13}^b \overline{E_3^b} & \eta_3 D_{13}^b E_3^b & 0 \\
 D_{31}^a E_1^a & -D_{31}^a \overline{E_1^a} & D_{33}^a E_3^a & -D_{33}^a \overline{E_3^a} & 0 & \eta_4 D_{31}^b \overline{E_1^b} & -\eta_4 D_{31}^b E_1^b & \eta_4 D_{33}^b \overline{E_3^b} & -\eta_4 D_{33}^b E_3^b & 0 \\
 0 & 0 & 0 & 0 & 0 & W_1^b E_1^b & -W_1^b \overline{E_1^b} & W_3^b E_3^b & -W_3^b \overline{E_3^b} & \alpha_f^l \\
 0 & 0 & 0 & 0 & 0 & D_{11}^b E_1^b & D_{11}^b \overline{E_1^b} & D_{13}^b E_3^b & D_{13}^b \overline{E_3^b} & -\rho_f^l v^2 \\
 0 & 0 & 0 & 0 & 0 & D_{31}^b E_1^b & -D_{31}^b \overline{E_1^b} & D_{33}^b E_3^b & -D_{33}^b \overline{E_3^b} & 0
 \end{bmatrix} \quad (A.37)$$

Following the same procedure from the previous section the determinant is simplified to

$$\begin{bmatrix}
 W_1^a & W_3^a & \eta_2 W_1^b & \eta_2 W_3^b & 0 & 0 & 0 & 0 & 1 & 1 \\
 D_{11}^a T_1^a & D_{13}^a T_3^a & -\eta_3 D_{11}^b T_1^b & -\eta_3 D_{13}^b T_3^b & 0 & 0 & 0 & 0 & -iU & -i(\eta_3/\eta_2)L \\
 D_{31}^a & D_{33}^a & \eta_4 D_{31}^b & \eta_4 D_{33}^b & 0 & 0 & 0 & 0 & 0 & 0 \\
 iT_1^a & iT_3^a & -i\eta_1 T_1^b & -i\eta_1 T_3^b & C_1^a & C_3^a & \eta_1 C_1^b & \eta_1 C_3^b & 0 & 0 \\
 0 & 0 & \eta_2 W_1^b & \eta_2 W_3^b & iW_1^a & iW_3^a & 0 & 0 & -1 & 1 \\
 0 & 0 & i\eta_3 D_{11}^b T_1^b & i\eta_3 D_{13}^b T_3^b & -D_{11}^a C_1^a & -D_{13}^a C_3^a & 0 & 0 & U & -(\eta_3/\eta_2)L \\
 0 & 0 & \eta_4 D_{31}^b & \eta_4 D_{33}^b & iD_{31}^a & iD_{33}^a & 0 & 0 & 0 & 0 \\
 0 & 0 & 0 & 0 & W_1^a & W_3^a & -\eta_2 W_1^b & -\eta_2 W_3^b & i & i \\
 0 & 0 & 0 & 0 & D_{11}^a C_1^a & D_{13}^a C_3^a & \eta_3 D_{11}^b C_1^b & \eta_3 D_{13}^b C_3^b & -U & -(\eta_3/\eta_2)L \\
 0 & 0 & 0 & 0 & D_{31}^a & D_{33}^a & -\eta_4 D_{31}^b & -\eta_4 D_{33}^b & 0 & 0
 \end{bmatrix} \quad (\text{A.38})$$

with L and U are the fluids contributions and are given by the equations (A.39) and respectively (A.40).

$$L = \frac{\bar{\rho}_f^l c^2}{\bar{\alpha}_f^l}, \quad (\text{A.39})$$

for the lower fluid and

$$U = \frac{\bar{\rho}_f^u c^2}{\bar{\alpha}_f^u}, \quad (\text{A.40})$$

Using Cramer's rule the reflection coefficient is then derived as

$$R = \frac{\Delta_R}{\Delta} = \frac{[M_1 - L(M_2 + M_3)] - U[(M_2 - M_3) - LM_4]}{[M_1 - L(M_2 + M_3)] + U[(M_2 - M_3) - LM_4]}. \quad (\text{A.41})$$

The terms M_i , ($i = 1..4$), are sums of 7x7 determinants. Both layers influence is coupled for each of the M_i , ($i = 1..4$) determinants. The exact expressions of these parameters are obtained using Maple. The Maple program, RCIImmersedMultilayer.mws, that produces the exact expression of the reflected coefficient is included on the attached CD-ROM.

Boundary conditions for various types of interface condition

To illustrate the interface conditions employed in the stress-jump model [73] we consider the planar boundary between two distinct media: upper medium \mathcal{U} (superscript u) and bottom medium \mathcal{B} (superscript b). Without losing the generality we consider the interface to coincide with the plane (x, y) with medium \mathcal{U} lying in the halfspace $z \leq 0$ and medium \mathcal{B} in the halfspace $z \geq 0$.

The following cases are commonly used throughout this work:

- Welded interface or ideal rigid bonding
 - continuity of the displacement and stress components

$$\begin{aligned} u_i^u &= u_i^b, \quad i = 1, 2, 3 \\ \sigma_{j3}^u &= \sigma_{j3}^b, \quad j = 1, 2, 3. \end{aligned} \tag{A.42}$$

- Smooth interface
 - continuity only of the normal displacement and stress components
 - shear stress components are zero for both media

$$\begin{aligned} u_3^u &= u_3^b, \\ \sigma_{33}^u &= \sigma_{33}^b \\ \sigma_{13}^u &= \sigma_{13}^b = \sigma_{23}^u = \sigma_{23}^b = 0. \end{aligned} \tag{A.43}$$

- Rough interface
 - continuity of the normal displacement and stress components
 - partial transmission of shear stress

$$\begin{aligned}
u_3^u &= u_3^b, \\
\sigma_{33}^u &= \sigma_{33}^b \\
u_1^u &= \eta_1 u_1^b, \\
u_2^u &= \eta_2 u_2^b, \\
\sigma_{13}^u &= \eta_3 \sigma_{13}^b, \\
\sigma_{23}^u &= \eta_4 \sigma_{23}^b,
\end{aligned} \tag{A.44}$$

with the parameter $0 \leq \eta_i \leq 1, i = 1 \dots 4$.

- Stress-free interface (vacuum)
 - all stress components are vanishing

$$\sigma_{i3}^u = \sigma_{i3}^b, \quad i = 1, 2, 3. \tag{A.45}$$

APPENDIX B ADDITIONAL INFORMATION ON THE COMPUTER PROGRAMS USED IN THE NUMERICAL EVALUATIONS OF THE ANALYTICAL MODELS

This appendix provides additional information on the various programs used in the thesis for the numerical prediction of the theoretical models. The programs can be found on the attached CD-ROM in the folder [drive letter]: \Programs. All programs, which were used in the numerical predictions of the model, are written in FORTRAN and some of them require the installation of the IMSL FORTRAN Math library. This library is protected by the copyright laws and it cannot be included on the disk. To acquire a license or find out additional information concerning this math library please visit <http://www.vni.com/products/imsl/>. The programs are organized in the order of their usage in the thesis.

Reflection from the glass-epoxy layer-balsa substrate

RCMarineComposite.f90

This program can be found in the folder ... \Programs \Reflection \RCMarineComposite. It is used for calculation of the reflection coefficient or received signal from the glass-epoxy layer-balsa substrate system as a function of the wavenumber and frequency. The bond condition between the layer and substrate is accounted for with the help of a simple stress-jump model. according to the expression developed in Appendix A.

The input parameters are divided in two categories: the transducer characteris-

tics and experimental geometry stored in the input file *TDATA_v1.dat* and the elastic medium properties stored in the input file *MDATA_v1.dat*. The numerical result is saved in three separate files as the absolute, real and respectively the imaginary values of the reflection coefficient or received voltage. The input parameters required by this program are the following

V_R:	the data output switch (1-voltage, 2-reflection coefficient),
tS:	the transmitter type (1-planar, 2-focused),
aS:	the transmitter radius (m),
tS:	the transmitter focal length (m),
alphaS:	the transmitter incident angle (deg.),
tR:	the receiver type (1-planar, 2-focused),
aR:	the receiver radius (m),
tR:	the receiver focal length (m),
alphaR:	the receiver incident angle (deg.),
fmin:	the start value of the frequency (MHz),
fstep:	the frequency step size (MHz),
fN:	the number of frequency steps,
kmin:	the start value of the wavenumber (m),
kstep:	the wavenumber step size (m),
kN:	the number of wavenumber steps,
DensityF:	the density of the fluid (kg/m^3),
VelocityF:	the wave velocity in the fluid (m/s),
rho:	the density of the layer (kg/m^3),
d:	the thickness of the layer (m),

- C: the elastic stiffness of the layer (MPa),
- rhoS: the density of the substrate (kg/m^3),
- CS: the elastic stiffness of the substrate (MPa).

The name of the output files can be changed by modifying the default name in the *MDATA.v1.dat* file.

Reflection coefficient calculation for a layered substrate

RCIsub.mws

This program can be found in the folder ...\\Programs \\Maple and shows the detailed calculation of the reflection coefficient for the glass-epoxy layer-balsa substrate system according to the expressions developed in Appendix A. Requires Maple 7.0 or later versions.

Reflection from the glass-epoxy balsa layered plate

RCImmersedMultilayer.f90

This program can be found in the folder ...\\Programs \\Reflection \\RCImmersedMultilayer. It is used for calculation of the reflection coefficient or received signal from the two layers plate glass-epoxy/balsa as a function of the wavenumber and frequency. The bond condition between the layer and substrate is accounted for with the help of a simple stress-jump model, according to the expression developed in Appendix A.

The input parameters are divided in two categories: the transducer characteristics and experimental geometry stored in the input file *TDATA.v2.dat* and the elastic medium properties stored in the input file *MDATA.v2.dat*. The numerical result is saved in three separate files as the absolute, real and respectively the imaginary values of the reflection coefficient or received voltage. The input parameters required by this program are the same as those of the RCMarineComposite.f90 plus the thickness of the

balsa plate dS . The name of the output files can be changed by modifying the default name in the *MDATA_v2.dat* file.

Reflection coefficient calculation for a layered plate glass-epoxy/balsa

RImmersedMultilayer.mws

This program can be found in the folder ...\\Programs \\Maple and shows the detailed calculation of the reflection coefficient for the two layers plate glass-epoxy/balsa according to the expressions developed in Appendix A. Requires Maple 7.0 or later versions.

Pressure field of a planar or focused Gaussian transducer

GaussianDirectivity_SCTP.f90

This program can be found in the folder ...\\Programs \\Directivity\\SCTP_VOLTAGE. It is used for calculation of the directivity pattern or received voltage from a planar or focused transducer as a function of the wavenumber and frequency. The program follows the expression developed in the chapter 2.

The input parameters are stored in the input file *INPUTDATA_v1.dat* and are the following

- T_R: the experimental geometry switch (1-transmission, 2-reflection),
- D_M: the data output switch (1-directivity, 2-voltage),
- DensityF: the density of the fluid (kg/m^3),
- VelocityF: the wave velocity in the fluid (m/s),
- rho: the density of the layer (kg/m^3),
- d: the thickness of the layer (m),
- C: the elastic stiffness of the layer (MPa),

tS: the transmitter type (1-planar, 2-focused),
 aS: the transmitter radius (m),
 tS: the transmitter focal length (m),
 alphaS: the transmitter incident angle (deg.),
 tR: the receiver type (1-planar, 2-focused),
 aR: the receiver radius (m),
 tR: the receiver focal length (m),
 alphaR: the receiver incident angle (deg.),
 fmin: the start value of the frequency (MHz),
 fstep: the frequency step size (MHz),
 fN: the number of frequency steps,
 kmin: the start value of the wavenumber (m),
 kstep: the wavenumber step size (m),
 kN: the number of wavenumber steps,

The numerical result is saved in three separate files as the absolute, real and respectively the imaginary values. The name of the output files can be changed by modifying the default names in the last six lines of the *INPUTDATA_v1.dat* file.

Pressure field of a planar or focused Gaussian transducer

GaussianDirectivity_MCTP.f90

This program can be found in the folder ...\\Programs\\Directivity\\MCTP_VOLTAGE and it is used for calculation of the directivity pattern or received voltage from a planar or focused transducer as a function of the wavenumber and frequency using multiple CTPs. The input parameters are stored in the input file *INPUTDATA_v2.dat* and are similar to the GaussianDirectivity_SCTP.f90 program. In addition to those parameters

N is the number of CTPs and A_n and B_n are the coefficients of the complex points according to Wen [97].

Received voltage from a plate in air-coupled transmission

Voltage_KF_CTP.f90

This program can be found in the folder ...\\Programs \\Transmission\\AirCoupledU and it is used for calculation of the received voltage from a planar or focused transducer as a function of the wavenumber and frequency in a pitch-catch transmission setup in air. The input parameters are stored in the input file *InputDATA_[MaterialName].dat* and are similar to the GaussianDirectivity_SCTP.f90 program.

BIBLIOGRAPHY

- [1] J. D. Achenbach, "*Wave propagation in elastic solids*," North-Holland series in applied mathematics and mechanics, 16, North-Holland publishing company, (1973).
- [2] J. D. Achenbach and H. Epstein, "*Dynamic interaction of a layer and a half space*," J. Eng. Mech. Div., 93, 5, 27-42 (1967).
- [3] D. Alleyne and P. Cawley, "*A two-dimensional Fourier transform method for the measurement of propagating multimode signals*," JASA, 89, 1159-1168, (1991).
- [4] M. Almqvist, A. Holm, H. W. Persson, K. Lindström, "*Characterization of air-coupled ultrasonic transducers in the frequency range 40kHz-2MHz using light diffraction tomography*," Ultrasonic, 37, 565-575, (2000).
- [5] M. F. Amateau, "*Engineering composite materials*," Penn State University Press, (2003).
- [6] G. B. Arfken, "*Mathematical methods for physicists*," Academic Press, (1985).
- [7] B. A. Auld,, "*Acoustic Fields and Waves in Solids*," 2nd ed., Robert E. Krieger Press, Malabar, FL, (1989).
- [8] B. A. Auld, "*General electro-mechanical reciprocity relations applied to the calculation of elastic wave scattering coefficients*," Wave Motion, 1, 3-10, (1979).
- [9] Y. Bar-Cohen, "*NDE of fiber-reinforced composite materials - a review*," Material Evaluation, 44, 446-454, (1986).

- [10] Y. Bar-Cohen, A. K. Mal and S. S. Lih, "*NDE of composite materials using ultrasonic oblique insonification*," *Material Evaluation*, 51, 1285-1296, (1993).
- [11] D. J. Barnard, J. J. Peters, and D. K. Hsu, "*Development of a magnetic cam for the computer aided tap test system*," *Review of Progress in QNDE*, 20, eds. D. O. Thompson and D. E. Chimenti, Plenum, New York, 1966-1971, (2000).
- [12] A. G. Bashford, "*Field characterization of an air-coupled micromachined ultrasonic capacitance transducer*," *JASA*, 101, 315-322, (1997).
- [13] G. Benny, G. Hayward and R. Chapman, "*Beam profile measurements and simulations for ultrasonic transducer operating in air*," *JASA*, 107, 2089-2100, (2000).
- [14] H. L. Bertoni and T. Tamir, "*Unified theory of Rayleigh-angle phenomena for acoustic beams at liquid-solid interfaces*," *Applied Physics*, 2, 157-172, (1973).
- [15] G. E. P. Box and G. Jenkins, "*Time series analysis: forecasting and control*," Holden-Day, (1976).
- [16] L. M. Brekhovskikh, "*Waves in layered media*," Academic Press, (1960).
- [17] L. J. Bond, C.-H. Chiang, and C. M. Fortunko, "*Absorption of ultrasonic waves in air at high frequencies (1020 MHz)*," *JASA*, 92, 2006-2015, (1992).
- [18] H. Carr and C. Wykes,, "*Diagnostic measurements in capacitive transducers*," *Ultrasonics*, 31, 13-20, (1993).
- [19] D. E. Chimenti, "*Guided waves in plates and their use in material characterization*," *Applied Mechanical Review*, 50, 247-284, (1997).
- [20] D. E. Chimenti and R. W. Martin, "*Nondestructive evaluation of composite laminates by leaky Lamb waves*," *Ultrasonics*, 29, 13-21, (1991).

- [21] D. E. Chimenti and C. M. Fortunko, “*Characterization of composite prepreg with gas-coupled ultrasonics*,” *Ultrasonics*, 32, 261-264, (1994).
- [22] D. E. Chimenti, J. Zhang, S. Zeroug and L. B. Felsen, “*Interaction of acoustic beams with fluid-loaded elastic structures*,” *JASA*, 95, 45-59, (1994).
- [23] D. E. Chimenti and D. Fei, “*Scattering coefficient reconstruction in plates using focused acoustic beams*,” *Int. J. Solids Struct.*, 39, 5495-5513, (2002).
- [24] D. E. Chimenti and A. H. Nayfeh, “*Leaky Lamb waves in fibrous composite laminates*,” *Journal of Applied Physics*, 58, 4531-38 (1985).
- [25] D. E. Chimenti and Sorin V. Teles, “*Ultrasonic technology for evaluation of bond-lines in glass-epoxy, balsa-core composites*,” Report on NSWC Contract Award N00167-00-M-0694, (2001).
- [26] D. E. Chimenti and O. I. Lobkis, “*Similarity of Gaussian and piston transducer voltages*,” *Review of Quantitative NDE*, ed. by D. O. Thompson and D. E. Chimenti, 22, 836-843, (2003).
- [27] V. Dayal, V. K. Kinra, “*Leaky Lamb waves in an anisotropic plate*,” *JASA*, 85, 2268-2276, (1989).
- [28] United States Department of defense handbook, “*Composite materials handbook. Volume 2 Polymer matrix composites materials properties*,” MIL-HDBK-17-2F, (2002).
- [29] M. Deschamps and B. Hosten, “*The effects of viscoelasticity on the reflection and transmission of ultrasonic waves by an orthotropic plate*,” *JASA*, 91, 2007-2015, (1992).
- [30] G. A. Deschamps, “*Gaussian beam as a bundle of complex rays*,” *Electron. Lett.*, 7, 684-685 (1971).

- [31] D. Fei and D. E. Chimenti, "*Single-scan elastic property estimation in plates*," Acoustics Research Letters Online, 2, 49-54, (2001).
- [32] D. Fei, D. E. Chimenti, and S. V. Teles, "*Material property estimation in thin plates using focused, synthetic-aperture acoustic beams*," JASA, 113, 2599-2610, (2003).
- [33] D. Fei and D. E. Chimenti, "*Complex transducer point model of focused-beam property estimation in plates*," Review of Quantitative NDE, ed. by D. O. Thompson and D. E. Chimenti, 21, 1377-1384, (2002)
- [34] D. Fei, D. E. Chimenti, and S. V. Teles, "*Rapid transmission coefficient reconstruction and material property estimation in plates*," Review of Quantitative NDE, ed. by D. O. Thompson and D. E. Chimenti, 21, 1400-1407, (2002)
- [35] D. Fei, "*Lay-up characterization and elastic property determination in composite laminates*," PhD dissertation, Iowa State University, (2001).
- [36] G. W. Farnell and E. L. Adler, "*Elastic Wave Propagation in Thin Layers*," edited by R. N. Thurston and W. P. Mason in Physical Acoustics, IX, Academic, New York, 35127, (1972).
- [37] Forest Products Laboratory, "*Wood handbook. Wood as an engineering material*," Gen. Tech. Rep. FPL-GTR-113, United States Department of Agriculture, Forest Service, Forest Products Laboratory Madison WI, (1999).
- [38] A. Gachagan, G. Hayward, S. P. Kelly and W. Galbraith, "*Characterization of air-coupled transducers*," IEEE Trans. Ultrasonics, Ferroelectrics, and Frequency Control, 43, 1-6, (1996).

- [39] T. H. Gan, D. A. Hutchins, D. R. Billson and D. W. Schindel, "*The use of broadband acoustic transducers and pulse-compression techniques for air-coupled ultrasonic imaging*," *Ultrasonics*, 43, 678-689, (1996).
- [40] T. Gudra, M. Pluta and Z. Kojro, "*The measurement and numerical modeling of the diffraction field of a spherical ultrasonic transducer working in the air at frequency of 1.3 MHz*," *Ultrasonics*, 38, 794-798, (2000).
- [41] M. F. Hamilton, "*Comparison of three transient solutions for the axial pressure in a focused sound beam*," *JASA*, 92, 527-532, (1992).
- [42] John W. Harris and Horst Stocker, "*Handbook of mathematics and computational science*," Springer, (1998).
- [43] S. D. Holland and W. Sachse, "*A time-resolved method for nonlinear ultrasonic measurements*," *Ultrasonics*, 40, 629-642, (2002).
- [44] S. D. Holland, S. V. Teles, and D. E. Chimenti, "*Quantitative air-coupled ultrasonic materials characterization with highly focussed acoustic beams*," *Review of Progress in Quantitative NDE*, 23, eds D. O. Thompson and D. E. Chimenti, Plenum Press, New York, 1376-1382, (2004).
- [45] S. D. Holland, S. V. Teles, and D. E. Chimenti, "*Air-coupled, focused ultrasonic dispersion spectrum reconstruction in plates*," *JASA*, 115, 2866-2873, (2004).
- [46] B. Hosten, D. A. Hutchins, and D. W. Schindel, "*Measurement of elastic constants in composite materials using air-coupled ultrasonic bulk waves*," *JASA*, 99, 2116-2123, (1996).
- [47] B. Hosten, M. Deschamps, and B. R. Tittmann, "*Inhomogeneous wave generation and propagation in lossy anisotropic solids. Application to the characterization of viscoelastic composite materials*," *JASA*, 82, 1763-1770, (1987).

- [48] B. Hosten and M. Castaings, "*Parabolic mirror and air-coupled transducer for multimodal plate wave detection*," Review of Progress in QNDE, 22, eds. D. O. Thompson and D. E. Chimenti, Plenum, New York, 1243-1250, (2002).
- [49] D. K. Hsu, D. J. Barnard, J. J. Peters, and V. Dayal, "*Physical basis of tap test as a quantitative imaging tool for composite structures on aircraft*," Review of Progress in QNDE, 19, eds. D. O. Thompson and D. E. Chimenti, Plenum, New York, 1857-1863, (1999).
- [50] D. A. Hutchins, D. W. Schindel, A. G. Bashford and W. M. D. Wright, "*Advances in electrostatic transduction*," Ultrasonics, 36, 1-6, (1998).
- [51] M. R. Karim, A. K. Mal, and Y. Bar-Cohen, "*Inversion of leaky Lamb wave by simplex algorithm*," JASA, 88, 482-491, (1990).
- [52] S. O. Kasap, "*Principles of electronic materials and devices*," 2nd Edition, McGraw-Hill, §7.6, 540-547, (2002).
- [53] G. S. Kino, "*The application of reciprocal theory to scattering of acoustic waves by flaws*," J. Appl. Phys., 49, 3190-3199, (1978).
- [54] R. T. Ko and L. Adler, "*Ultrasonic evaluation of an interface between a coating layer and substrate*," Ultrasonic Characterization and Mechanics of Interfaces ASME, (AMD-Vol. 177), (1993).
- [55] W. Kuhl, G. R. Schodder, and F. K. Schröder, "*Condenser transmitters and microphones with solid dielectric for airborne ultrasonics*," Acustica, 4, 519-532, (1954).
- [56] T. Kundu, K. Maslov, P. Karpur, T. E. Matikas and P. D. Nicolaou, "*A Lamb wave scanning approach for the mapping of defects in [0/90] titanium matrix composites*," Ultrasonics, 34, 43-49, (1996).

- [57] T. Kundu, A. Maji, T. Ghosh and K. Maslov, "*Detection of kissing bonds by Lamb waves*," Ultrasonics, 35, 573-580, (1998).
- [58] I. Ladabaum and B. T. Khuri-Yakub, "*Micromachined ultrasonic transducers: 11.4 MHz transmission in air and more*," Appl. Phys. Lett., 68, 7 (1996)
- [59] W. Michael Lai, David Rubin and Erhard Kreml, "*Introduction to continuum mechanics*," 3rd Edition, Butterworth-Heinemann, (1993).
- [60] V. M. Levin, O. I. Lobkis and R. G. Maev, "*Field of a spherical focusing transducer with arbitrary aperture angle*," Sov. Phys. Acoustic, 33, 87-89, (1987).
- [61] G. Ljung and G. Box, "*On a measure of lack of fit in time series models*," Biometrika, 67, 297-303, (1978).
- [62] O. I. Lobkis, A. Safaeinili and D. E. Chimenti, "*Precision ultrasonic reflection studies in fluid-coupled plates*," JASA, 99, 2727-2736, (1996).
- [63] O. I. Lobkis, D. E. Chimenti, and H. Zhang, "*In-plane elastic property characterization in composite plates*," JASA, 107, 1852-1857, (2000).
- [64] O. I. Lobkis and D. E. Chimenti, "*Three-dimensional transducer voltage in anisotropic materials characterization*," JASA, 106, 36-45, (1999).
- [65] O. I. Lobkis and D. E. Chimenti, "*Equivalence of Gaussian and piston ultrasonic transducer voltages*," JASA, 114, 3155-3166, (2003)
- [66] M. J. S. Lowe, "*Matrix techniques for modeling ultrasonic waves in multilayered media*," IEEE Trans. Ultrasonics, Ferroelectrics, and Frequency Control, 42, 525-542, (1995).
- [67] B. G. Lucas, "*The field of a focusing source*," JASA, 72, 1289-1296, (1982).

- [68] M. Luukkala, P. Heikkilä, and J. Surakka, “Plate wave resonance – a contactless test method,” *Ultrasonics*, 9, 201-208, (1971).
- [69] K. Maslov and T. Kundu, “Selection of Lamb modes for detecting internal defects in composite laminates,” *Ultrasonics*, 35, 141-150, (1997).
- [70] O. B. Matar, L. Pizarro, D. Certon, J. P. Remenieras, F. Patat, “Characterization of airborne transducers by optical tomography,” *Ultrasonics*, 38, 787-793, (2000).
- [71] National Institute of Standards and Technology - *Dataplot* statistical software, <http://www.itl.nist.gov/div898/software/dataplot/index.htm>
- [72] P. Nagy, W. R. Rose and L. Adler, “Single transducer broadband technique for leaky Lamb wave detection,” *Review of Progress in Quantitative NDE*, 6, 483-490, (1987).
- [73] A. H. Nayfeh, “Wave propagation in layered anisotropic media - with application to composites,” Elsevier, New York, (1995).
- [74] A.H. Nayfeh and D. E. Chimenti, “Ultrasonic plate waves in 3-D braided composites,” *JASA*, 97, 2056-2064, (1995).
- [75] A. H. Nayfeh and D. E. Chimenti, “Reflection of finite acoustic beams from loaded and stiffened halfspaces,” *JASA*, 75, 1360-1368, (1984) .
- [76] A. H. Nayfeh and P. Nagy, “General study of axisymmetric waves in layered anisotropic fibers and their composites,” *JASA*, 99, 931-941, (1996).
- [77] A. H. Nayfeh, “The general problem of elastic wave propagation in multilayered anisotropic media,” *JASA*, 89, 1521-1531, (1991).
- [78] H. T. O’Neil, “Theory of the focusing radiators,” *JASA*, 21, 516-526, (1949).

- [79] S. Orfanidis, *"Introduction to signal processing,"* Prentice Hall, (1996).
- [80] J. J. Peters, Z. A. Nielsen and D. K. Hsu, *"Comparison of local stiffness of composite honeycomb sandwich structures measured by tap test and mechanical test,"* Review of Progress in QNDE, 20, eds. D. O. Thompson and D. E. Chimenti, Plenum, New York, 1031-1038, (2000).
- [81] L. Pizarro, D. Certon, M. Lethiecq, B. Hoasten, *"Airborne electrostatic transducers with conductive grooved backplate: tailoring their center frequency, sensitivity and bandwidth,"* Ultrasonics, 37, 493-503, (1999).
- [82] T. J. Robertson, D. A. Hutchins and D. R. Billson, *"Capacitive air-coupled cylindrical transducers for ultrasonic imaging applications,"* Meas. Sci. Technol., 12, 758-769, (2002).
- [83] W. P. Rogers, *"Measurement of elastic properties of transversely isotropic plates using RayleighLamb waves,"* JASA, 94, 1837, (1993).
- [84] S. I. Rokhlin and D. E. Chimenti, *"Reconstruction of elastic constants from ultrasonic reflectivity data in a fluid-coupled composite plate,"* Review of Progress in QNDE, 9, eds. D. O. Thompson and D. E. Chimenti, Plenum, New York, 1411-1418, (1990).
- [85] S. I. Rokhlin and W. Wang, *"Double through-transmission bulk wave method for ultrasonic phase velocity measurement and determination of elastic constants of composite materials,"* JASA, 91, 3303-3312, (1992).
- [86] Joseph L. Rose, *"Ultrasonic waves in solid media,"* Cambridge University Press, (1999).
- [87] W. Sachse and Y.-H. Pao, *"On the determination of phase and group velocities of dispersive waves in solids,"* J. Appl. Phys., 49, 4320-4327, (1978).

- [88] A. Safaeinili, O. I. Lobkis and D. E. Chimenti, "Air-coupled ultrasonic estimation of viscoelastic stiffnesses in plates," *IEEE Trans. Ultrason. Ferroelect. Freq. Cont.*, 43, 1171-1179, (1996).
- [89] A. Safaeinili, O. I. Lobkis and D. E. Chimenti, "Quantitative materials characterization using air-coupled leaky Lamb waves," *Ultrasonics*, 34, 393-396, (1996).
- [90] D. W. Schindel, D. A. Hutchins, Lichun Zou, and M. Sayer,, "The design and characterization of micromachined air-coupled capacitance transducers," *IEEE Trans. Ultrason. Ferroelect. Freq. Cont.*, 42, 42-50, (1995).
- [91] D.W. Schindel, "Focussing of ultrasonic waves in air using a micromachined Fresnel zone plate," *Ultrasonics*, 35, 275-285, (1997).
- [92] L. W. Schmerr, "Fundamentals of ultrasonic nondestructive evaluation - a modeling approach," Plenum Press, (1998).
- [93] A. R. Selfridge, "Approximative material properties in isotropic materials," *IEEE Trans. on Sonics and Ultrasonics*, SU-32, No. 3, 381-395, (1985).
- [94] R. B. Thompson and E. F. Lopes, "The effects of focussing and refraction on Gaussian ultrasonic beams," *J. NDE* , 4(2), 107-123, (1984).
- [95] I. A. Viktorov, "Rayleigh and Lamb waves," Plenum Press, New York, (1967).
- [96] R. L. Weaver, W. Sachse, and L. Niu, "Transient ultrasonic waves in a viscoelastic plate: applications to materials characterization," *JASA*, 85, 2262-2267, (1989).
- [97] J.J. Wen and M. A. Breazeale, "A diffraction beam field expressed as the superposition of Gaussian beams," *JASA* 83, 1752-1756, (1988).
- [98] A. O. Williams, "Acoustic intensity distribution from a piston source. The concave piston," *JASA*, 17, 219-227, (1946).

- [99] S. Zeroug, F. E. Stanke, and R. Burridge, "A complex-transducer-point model for emitting and receiving ultrasonic transducers," *Wave Motion*, 24, 21-40, (1996).
- [100] S. Zeroug and L. B. Felsen, "Nonspecular reflection of two- and three-dimensional acoustic beams from fluid-immersed plane-layered elastic structures," *JASA*, 95, 3075-3098 (1994).
- [101] H. Zhang and D. E. Chimenti, "Two- and three-dimensional complex-transducer-point analysis of beam reflection from anisotropic plates," *JASA*, 108, 1-9, (2000).
- [102] H. Zhang, D. E. Chimenti, and S. Zeroug, "Transducer misalignment effects in beam reflection from elastic structures," *JASA*, 104, 1982-91, (1996).
- [103] H. Zhang and D. E. Chimenti, "Air-coupled ultrasonic beam transmission applied to material characterization," *Review of Progress in Quantitative NDE*, 18, eds D. O. Thompson and D. E. Chimenti, Plenum Press, New York, 1273-1280, (1999).
- [104] H. Zhang, "Interaction of acoustic beam with elastic structures, PhD dissertation, Iowa State University, (1998).

ACKNOWLEDGEMENTS

I would like to take this opportunity to express my sincere gratitude to my major professor Dr. Dale E. Chimenti for his guidance, encouragement, support and patience while achieving this project in my life. His extensive knowledge, creativity, and tireless optimism have been truly inspirational. I feel honored to have worked under his direction for all these years.

I would also like to thank my committee members for their efforts and contributions to this work: Dr. Bruce R. Thompson for his constant support and encouragement, Dr. Julie Dickerson, Dr. John Basart and Dr. David K. Hsu for their assistance in my research.

I would also like to specifically recognize two member of Dr. Dale E. Chimenti research group for their assistance with this work: Dr. Dong Fei and Dr. Steven Holland. I have worked very closely with both in the course of my research presented here and from whose knowledge I have borrowed often and freely. Dr. Fei helped me significantly, during the initial stages of my graduate career, with discussions on experiments, signal processing and modeling. The success of the air-coupled system used in the third chapter of this thesis is due in no small part to Dr. Holland. His ample experience proved very useful in designing a fast data acquisition and processing system and implementing a pulse-compression technique which both operated nearly flawlessly during the entirety of the experiment.

Special thanks to the rest of the professors, researchers, support staff, and students here at the Center for NDE and in my department of Aerospace Engineering. Your

assistance and friendship have made my graduate studies a wonderful experience.

At last, but not least, I thank my wonderful wife, Adriana, who has always been supportive of my work, drive, and ambition, and for her unconditional love and faith. I am grateful to my parents, Constantin and Elena, for giving me every opportunity that could be made available, for encouraging me to strive for the best education possible, and supporting me in anything I chose to pursue in life. I am also thankful to my parents-in-law, Ion and Eugenia, who are always willing to help and never let us forget that we have their love and support. I dedicate this work to them.